

# The Identification of Hydrogen-Deficient Cataclysmic Variable Donor Stars<sup>1,2</sup>

Thomas E. Harrison

Department of Astronomy, New Mexico State University, Box 30001, MSC 4500, Las  
Cruces, NM 88003-8001

Received \_\_\_\_\_;    accepted \_\_\_\_\_

## ABSTRACT

We have used ATLAS12 to generate hydrogen-deficient stellar atmospheres to allow us to construct synthetic spectra to explore the possibility that the donor stars in some cataclysmic variables (CVs) are hydrogen deficient. We find that four systems, AE Aqr, DX And, EY Cyg, and QZ Ser have significant hydrogen deficits. We confirm that carbon and magnesium deficits, and sodium enhancements, are common among CV donor stars. The three Z Cam systems we observed are found to have solar metallicities and no abundance anomalies. Two of these objects, Z Cam and AH Her, have M-type donor stars; much cooler than expected given their long orbital periods. By using the combination of equivalent width measurements and light curve modeling, we have developed the ability to account for contamination of the donor star spectra by other luminosity sources in the binary. This enables more realistic assessments of secondary star metallicities. We find that the use of equivalent width measurements should allow for robust metallicities and abundance anomalies to be determined for CVs with M-type donor stars.

*Key words:* stars — infrared: stars — stars: novae, cataclysmic variables — stars: abundances — stars: individual (DX And, RX And, AE Aqr, Z Cam, SY Cnc, EM Cyg, EY Cyg, SS Cyg, V508 Dra, AH Her, RU Peg, GK Per, QZ Ser)

<sup>1</sup>Partially based on observations obtained with the Apache Point Observatory 3.5-meter telescope, which is owned and operated by the Astrophysical Research Consortium.

<sup>2</sup>Partially based on observations obtained at the Gemini Observatory, which is operated by the Association of Universities for Research in Astronomy, Inc., under a cooperative agreement with the NSF on behalf of the Gemini partnership: the National Science Foundation (United States), the National Research Council (Canada), CONICYT (Chile),

Ministerio de Ciencia, Tecnología e Innovación Productiva (Argentina), and Ministério da Ciência, Tecnologia e Inovação (Brazil).

## 1. Introduction

Cataclysmic variable stars (CVs) consist of a white dwarf that is accreting matter from a late-type secondary star. The standard paradigm for the formation of CVs postulates that they start out as wide binaries ( $a > 130 R_{\odot}$ , Warner 1995), whose orbital separation depends on the ratio of the initial to final mass of the primary, and is also a function of the binary mass ratio (see Ritter 2012). For single stars, to produce the typical  $0.8 M_{\odot}$  white dwarf found in CVs (Knigge et al. 2011), requires a main sequence dwarf with an initial mass of  $5 M_{\odot}$  (Salaris et al. 2009). As the white dwarf progenitor evolves off of the main sequence, the secondary star suddenly finds itself orbiting within the red giant photosphere. During this common envelope (CE) phase, most of the angular momentum of the binary is believed to be shed due to interactions of the secondary star with the atmosphere of the red giant. During this process, the binary period gets shortened, and the red giant envelope gets ejected. Depending on the input parameters used in “standard” CE models, between 50 and 90% of all these close binary stars merge (c.f., Politano & Weiler 2007). At the end of this process, 50 to 80% of the initial mass of the progenitor system has been lost (Ritter 1976). After emerging from the CE phase, an epoch of angular momentum loss via magnetic braking (e.g., King & Kolb 1995), lasting  $\sim 10^7$  yr (Warner 1995), is then required that leads to the formation of a “semi-detached” binary, and the mass transfer phase that signals the birth of a CV.

If this framework were true, the majority of donor stars in CVs would not be expected to have undergone any significant nuclear evolution, they would perhaps be slightly bloated main-sequence-like stars (see Howell et al. 2001), but not otherwise unusual. After a

considerable amount of observational data had been amassed that showed that many donor stars had cooler spectral types than expected for their orbital period (e.g., Friend et al. 1990ab, or Beuermann et al. 1998; see Fig. 30 in Harrison 2016 for a recent update), had masses and radii inconsistent with main sequence stars (e.g., Bitner et al. 2007, Echevarría et al. 2007, Neustroev & Zharikov 2008, Rodriguez-Gil et al. 2009), and infrared spectra that revealed unusual abundances, especially strong deficits of carbon (Harrison et al. 2004a, 2005, 2009), it was clear that many CV donor stars bore little resemblance to normal main sequence dwarfs. Additionally, it was noted decades ago that the helium emission lines in many CVs were much stronger than expected, implying an enhanced abundance of helium in the material being transferred from the secondary star (Williams & Ferguson 1982). The UV spectra of many CVs also show unusual carbon to nitrogen line ratios (e.g., Bonnet-Bidaud & Mouchet 1987, Szkody & Silber 1996, Mauche et al. 1997, Gänsicke et al. 2003), suggesting deficits of carbon, and enhancements of nitrogen. Hamilton et al. (2011) found that CV donor stars that had carbon deficits, inferred from weak CO absorption features in  $K$ -band spectra, also had unusually weak C IV emission lines in the UV. Clearly, the donor stars of some CVs are chemically peculiar, presumably due to post-main sequence evolution prior to contact.

Goliash & Nelson (2015) have produced a new population synthesis calculation for CVs that includes detailed nuclear evolution, with more massive progenitor binaries. They confirm the results of Podsiadlowski et al. (2003), showing that there is a large range of masses and radii for donors in CVs with  $P_{\text{orb}} > 5$  hr when nuclear evolved secondary stars are considered. This effect arises due to some donors being zero age main sequence stars at the time they become semi-contact binaries, while others have undergone significant nuclear processing. The results of our CV temperature/abundance survey (Harrison 2016) confirms this conjecture, finding normal main sequence star donors in some systems, and secondaries that appear to be highly evolved in others.

Podsiadlowski et al. suggest that the secondaries that have undergone pre-CV evolution should show evidence for nuclear processing, in particular, products of the CNO cycle. Harrison & Marra (2017) used moderate resolution *K*-band spectroscopy to investigate the isotopic ratio of carbon to test whether there was evidence for CNO cycle processes. For the three systems they observed, small values of the  $^{12}\text{C}/^{13}\text{C}$  ratio ( $\leq 15$ ) were found. This indicates that all three donor stars had begun to evolve off the main sequence before becoming semi-contact binaries. Surprisingly, Harrison & Marra also found enhancements in the sodium abundance for all three objects.

In Harrison (2016), unusual abundances of sodium were found in two CVs: QZ Ser and EI Psc. Both of these objects are short period CVs, but appear to have K-type secondary stars, instead of the expected M-type (or later) secondaries. Thorstensen et al. (2002) suggested one possible way to explain the donor in QZ Ser is that it is hydrogen deficient, with an enhancement of helium. Perhaps an atmosphere that is hydrogen-deficient could explain many of the abundance anomalies found in Harrison (2016) or Harrison & Marra (2017). To test this we have generated a grid of hydrogen deficient stellar atmospheres using ATLAS12 (Kurucz 2005) for the purpose of creating synthetic spectra to derive the abundances for CV donor stars. We have found evidence for hydrogen deficiencies in four systems. In the next section we discuss the data used, the construction of the atmosphere models, accounting for possible contamination, and the equivalent width measurement process. In section 3 we present our analysis of the infrared spectra of CV secondary stars, and in section 4 we discuss our results, presenting our conclusions in section 5.

## 2. Data Reduction and Analysis Techniques

### 2.1. *JHK* Spectra for the Program Objects

The observational details of the IRTF/SPEX near-infrared spectroscopic data used below are listed in Harrison (2016, “H16”). In this paper, we only analyze the cross-dispersed data for CVs that are expected to have K-type donor stars. To the SPEX data set we add observations made with GNIRS<sup>1</sup> on Gemini-North, and with TripleSpec<sup>2</sup> on the Apache Point Observatory 3.5 m. An observation log for the latter two data sets is presented in Table 1. Both GNIRS and TripleSpec produce crossed-dispersed data across the *JHK* bandpasses with a resolution similar to that of SPEX on the IRTF. The GNIRS and TripleSpec observations were reduced in the usual fashion using IRAF (see H16). For all of the objects, telluric standards were observed at a similar airmass as the program target. The GNIRS spectra were wavelength calibrated using arc lamp spectra, while for TripleSpec we used night sky OH emission lines.

### 2.2. Generation of Hydrogen-Deficient Atmospheres and Synthetic Spectra

To allow the generation of hydrogen-deficient spectra, we employed ATLAS12 (Kurucz 2005). Compared to earlier versions of the ATLAS program series, ATLAS12 uses the “Opacity Sampling” method to compute line opacity in atmosphere models. Models generated using ATLAS12 can have the abundances of individual elements set while calculating an atmosphere, versus only being able to change the global metallicity in the “Opacity Distribution Function” (ODF) method used in ATLAS9, and earlier versions of

---

<sup>1</sup><https://www.gemini.edu/sciops/instruments/gnirs/>

<sup>2</sup><http://www.apo.nmsu.edu/arc35m/Instruments/TRIPLESPEC/>

this software. Where to download the codes, and how to run the software, are described in Castelli (2005).

To run ATLAS12, one needs to have pre-computed atmospheres for input. As described in Castelli, these can be ODF models generated using ATLAS9. Thus, to generate a grid of ATLAS12 models, requires a set of standard Kurucz ODF atmospheres covering the desired range of parameters. Given that none of the objects modeled here appeared to have extremely low metallicities, our grid covers the ranges  $-0.5 \leq [\text{Fe}/\text{H}] \leq +0.5$  in steps of  $\pm 0.1$  (less  $[\text{Fe}/\text{H}] = \pm 0.4$ ), and  $4000 \text{ K} \leq T_{\text{eff}} \leq 5500 \text{ K}$  in steps of 250 K. We computed this range for two different gravities ( $\log g = 4.0$  and  $4.5$ ), and at five different H-deficiencies: 0%, 25%, 50%, 75%, and 90%. Obviously, if we change the hydrogen abundance, the actual value of  $[\text{Fe}/\text{H}]$  also changes. To reduce confusion, and because we are not altering the abundances of any of the elements when running models of different metallicities, we keep the labeling consistent: if the ATLAS9 input atmosphere model had  $[\text{Fe}/\text{H}] = -0.3$ , no matter the hydrogen abundance of the ATLAS12 output model, we will label this an  $[\text{Fe}/\text{H}] = -0.3$  atmosphere model.

Before we started, we had to make a choice for the helium abundance. For a solar abundance, ATLAS12 lists the hydrogen abundance as  $\log H = -0.036$ , and helium as  $\log \text{He} = -1.106$ . This is not the standard notation by which such abundances are usually expressed, but is the format used by Kurucz. Normally the  $\log$  of the abundance of hydrogen is set equal to 12.0. To convert between the two scales one uses the equation  $\log(A/N_H) = 12.0 + \log(A/N_{\text{total}}) - \log(N_H/N_{\text{total}})$ . Where  $\log(A/N_{\text{total}})$  is the abundance of the element A in terms of number density relative to total number density. The value of  $\log(N_H/N_{\text{total}}) = -0.036$ .

To test how the He abundance actually affects the results we ran three models. The first has  $\log H = -0.3370$  (a hydrogen deficit of 50%),  $\log \text{He} = -1.106$  (the solar value),

the second has  $\log H = -0.3370$ ,  $\log He = -0.8046$  (He abundance increased by 50%), and  $\log H = -0.3370$ ,  $\log He = -0.2696$  (He abundance exactly replaces the lost hydrogen). We ran the programs described below to measure the equivalent widths in the near-infrared bandpasses. The last of these three models, exact replacement, produces spectra with the largest equivalent widths. For example, the equivalent width measurements for the sodium doublet at 22,000 Å in the *K*-band for each of these three models ( $T_{\text{eff}} = 5000$  K,  $[Fe/H] = 0.0$ ) are 1.44 Å, 1.47 Å, and 1.56 Å. On average, the equivalent width measurements for the exact replacement models are  $\sim 10\%$  larger for most lines than in either of the other two models. This is near the noise level for most of the measurements we present below. Thus, for simplicity, we decided to enhance the helium abundance to exactly make-up for the hydrogen deficiency, keeping the total abundance of  $H + He$  constant. If the helium abundance is lower than this, any hydrogen deficits found below will actually be slightly larger than measured.

The final grid of atmosphere models, in the form preferred as input to Gray’s SPECTRUM<sup>3</sup> program, can be found at <http://astronomy.nmsu.edu/tharriso/hdeficient>. We then used the program SPECTRUM, as described in H16, to generate synthetic spectra using the new hydrogen-deficient atmospheres. As discussed in Harrison & Marra (2017, “HM17”), two supplemental programs supplied with SPECTRUM, *avsini* and *smooth2*, were used to rotationally broaden and to match the dispersion of the model spectra to that of the data. Note that the three instruments whose data we analyze below have slightly different dispersions, and these were taken into account when generating model grids for each of the objects.

---

<sup>3</sup><http://www.appstate.edu/~grayro/spectrum/spectrum.html>

### 2.3. Infrared Light Curve Data for Contamination Estimates

In H16 and HM17, no attempt was made to examine the issue of contamination of the observed spectra due to emission by sources other than the donor star. Such a process can strongly affect the derived global metallicities, as it simultaneously weakens the apparent strength of all of the absorption features in the donor star spectrum. As we will show, it appears to have had little affect on the temperatures or relative elemental abundances they derived for the systems in common which we analyze below. To derive a contamination estimate, however, is difficult. It either requires the a priori fixing of the metallicity, or the use of some source of information that allows us to check whether a particular contamination level is likely. We use light curve modeling to supply this additional source of information.

For three targets below, DX And, SS Cyg, and RU Peg, we model *JHK* light curves the data for which were obtained with SQUIID<sup>4</sup> on the KPNO 2.1 m telescope. The photometry for SS Cyg comes from Harrison et al. (2007). The light curve data for RU Peg was collected over three consecutive nights, 3 to 5 August 2003. The observations for DX And occurred on 7 and 10 August 2003. For each of the three CVs, differential photometry was performed relative to stars in the field, and calibrated using data from 2MASS. To these data we add the light curve photometry from *WISE* (Wright et al. 2010) and *NEOWISE* (Mainzer et al. 2011).

For the majority of CVs, we only have *WISE* and *NEOWISE* light curves to work with. We use the Wilson-Divinney light curve modeling software WD2010<sup>5</sup> to produce models for the *JHK* and *WISE/NEOWISE* photometry. See Harrison et al. (2013a) for

---

<sup>4</sup><https://www.noao.edu/kpno/sqiid/>

<sup>5</sup><ftp://ftp.astro.ufl.edu/pub/wilson/lcdc2010>

details on how WD2010 can be used to model *WISE* light curves. For light curve modeling, the main influence of a source of contamination (“third light”) is its affect on the derived orbital inclination. A source of contamination dilutes the ellipsoidal variations that arise from the distorted shape of the secondary star, driving the apparent orbital inclination to lower values.

## 2.4. Equivalent Width Measurements

For the analysis used below, we change from the  $\chi^2$ -based analysis of H16 and HM17 to the measurement of equivalent widths. The main reason for this switch is the fact that different elements have different responses to a change in the hydrogen abundance. The increase in the complexity introduced by possible hydrogen deficits makes the results from  $\chi^2$  analysis ambiguous, as analysis of broad segments of the spectra can produce identical  $\chi^2$  values due to either a large hydrogen deficit, or a high metallicity. Thus, while individual elemental abundances (especially carbon) are derived using the same  $\chi^2$  analysis techniques used in H16 and HM17, to examine the donor star spectra for possible hydrogen deficits requires us to compare the equivalent widths of various lines from individual elements in the object spectra to those of the model spectra. A secondary reason for this switch is the fact that the  $\chi^2$  analysis is more sensitive to the quality of the continuum division than are equivalent width measurements.

To demonstrate how the spectra change with hydrogen abundance, we plot synthetic *K*-band spectra for five different values in Fig. 1. All of the spectra have identical parameters,  $T_{\text{eff}} = 5000$  K, and  $[\text{Fe}/\text{H}] = 0.0$ . As might be expected, diminishing the hydrogen abundance results in stronger metal lines in the synthetic spectra. While the lines all get stronger as we decrease hydrogen (since we are essentially increasing the relative metallicity), there are subtle differences on how the lines from each of the metals responds

due to the changes in the structure of the stellar atmospheres. Focusing on the spectral range from 22500 to 23200 Å we have three large absorption features: the Ca I triplet at 22632 Å, Mg I at 22808 Å, and the  $^{12}\text{CO}_{(2,0)}$  bandhead at 22937 Å. It is clear that the CO bandhead does not strengthen as quickly as either Ca I or Mg I, and Ca I strengthens more quickly than Mg I. In Fig. 2 we plot the equivalent widths for the Na I doublet at 22000 Å, the Ca I triplet, and the Mg I line for the five different hydrogen abundances. The Na I doublet strengthens more rapidly with decreasing hydrogen abundance than the lines for either of those other two elements.

We will use this type of analysis for all of the objects discussed below. We calculate the equivalent widths and their errors using the method discussed in Vollmann & Eversberg (2006). In Table 2 we list the spectral limits for each element’s equivalent width measurement along with those of their continuum bandpasses. Where there are multiple lines from an element in one of the near-IR bandpasses, we sum the equivalent widths of those lines, and add their errors in quadrature. Though we have selected these bandpasses because they are mostly free from strong emission features from the program CVs, some of them will occasionally be affected by a stronger-than-normal emission line from the CVs, or from a poor telluric absorption correction, such as the red end of the *J*-band. In cases where there are noise spikes or other features located near a spectral line of interest, we have resorted to using the *splot* routine in IRAF to measure equivalent widths. We find that the equivalent width measurements produced by our program agree very well with those from *splot*. We will note these object-specific issues as we encounter them. It is also important to note that the equivalent widths for Na I in the *J*-band and *H*-bands are often suspect. The Na I doublet in the *J*-band falls on the red edge of a strong telluric feature, and the line and continuum regions are always very noisy. In the *H*-band, the Na I doublet is quite weak, and falls amongst a large number of other absorption lines, so its measurement can be unreliable, especially for cooler stars. As shown in HM17, the abundance of carbon can be

derived to a high precision from the CO features in the  $K$ -band using the  $\chi^2$  method. We will not be using the equivalent width measurement techniques to examine its abundance.

To provide a test of the reliability of the equivalent width measurement process we return to the spectra of the K dwarfs from the IRTF Spectral Library (Cushing et al. 2005) used in H16. To this data set we add the star 61 Cyg A observed using SPEX (Harrison et al. 2004a), with the means of its data from the PASTEL catalog (Soubiran et al. 2016). We list the mean temperatures and metallicities for these K dwarfs from the PASTEL catalog in Table 3. In Fig. 3abc, we plot the equivalent width measurements for the eight K dwarfs in the three bandpasses against the results from the synthetic spectra for six different metallicities:  $[\text{Fe}/\text{H}] = -0.2, -0.1, 0.0, +0.1, +0.2$ , and  $+0.5$ . This range in metallicities covers the observed range for the K dwarfs listed in Table 3.

We used these same objects in H16 to demonstrate the efficacy of the  $\chi^2$  analysis method in deriving their previously published temperatures and metallicities. Thus, it is not surprising that the equivalent width measurements for these K dwarfs are consistent with the results for the synthetic spectra to within the error bars of the equivalent width measurements, assuming the tabulated metallicities (and error bars) listed in Table 3. The equivalent width measurements for the K4V star HD45977, however, *generally* appear to be larger than expected given the data in Table 3, and differ from the results in H16. A metallicity closer to  $[\text{Fe}/\text{H}] = +0.2$  would be a better match to its measurements. The PASTEL catalog has  $\log g = 4.3$  listed for this star, so perhaps it is slightly evolved, and a lower gravity model would provide a better match to the observations.

### 3. Results

We present our equivalent width and contamination analysis for the program CVs below. These are ordered by constellation name, except for the first object, SS Cyg. Given the change in our procedure, and the fact that the entire process for each object can be quite involved, we use the data set for SS Cyg to show all of the steps used in assessing whether the hydrogen abundance is non-solar.

#### 3.1. SS Cygni

HM17 presented a new analysis of SS Cygni using both moderate resolution  $K$ -band spectra from NIRSPEC on Gemini, and cross-dispersed data from SPEX on the IRTF. Their best fitting  $\log g = 4.5$  model had the following parameters:  $T_{\text{eff}} = 4750 \pm 204$  K,  $[\text{Fe}/\text{H}] = -0.3$ ,  $[\text{C}/\text{Fe}] = -0.1$ ,  $[\text{Mg}/\text{Fe}] = -0.4$ ,  $[\text{Na}/\text{Fe}] = +0.4$ , and  $^{12}\text{C}/^{13}\text{C} = 4$ . In the following, we will assume an isotopic ratio of  $^{12}\text{C}/^{13}\text{C} = 4$  for all of our models for SS Cyg. The weakness of the  $^{13}\text{CO}$  features, and the lower resolution of the cross-dispersed data set, do not allow a robust measurement of the  $^{12}\text{C}/^{13}\text{C}$  ratio. As discussed in HM17, the main effect of fixing  $^{12}\text{C}/^{13}\text{C} = 4$  is to raise the value of  $[\text{C}/\text{Fe}]$  by  $+0.1$ , when compared to the value of  $[\text{C}/\text{Fe}]$  found using the cosmic value ( $^{12}\text{C}/^{13}\text{C} = 89$ ). We have chosen not to use the red Na I doublet in the  $K$ -band in our analysis procedure as it sits amidst strong CO absorption features, and thus requires a precise value of  $[\text{C}/\text{Fe}]$  to obtain a reliable measurement. This does not, however, void the need for including the correct input value for  $[\text{C}/\text{Fe}]$ . Both the level of the blue continuum in the  $H$ -band, and the broad absorption feature in the  $J$ -band near  $1.12 \mu\text{m}$ , are shaped by CN absorption. Thus, for the model spectra to more closely resemble reality, we must include the best available value for the carbon abundance when generating the synthetic spectra.

Before we describe the equivalent width (hereafter, ‘EQW’) measurements, we briefly discuss the possibility of contamination of the spectra by emission from sources in SS Cyg other than the donor star. Contamination of the spectrum by emission from the white dwarf and its accretion disk can be a serious problem as one works towards bluer wavelengths. Bitner et al. (2007) found that at 5500 Å, the white dwarf and accretion disk in SS Cyg account for 54% of the system’s luminosity. Presumably, this should be smaller in the near-infrared, where the spectral energy distributions of K dwarfs peak. As shown in Fig. 1 of H16, most of the metal lines increase in strength with decreasing temperature in the K dwarfs. Thus, if there is significant contamination as one progresses from the  $K$ -band to the  $J$ -band, the best fitting models in the  $H$ - or  $J$ -band should, in general, be hotter than those in the  $K$ -band. This allows for the possibility of quantifying *differential* contamination. We encounter this issue in the following subsection, and address the possibility of contamination across the near-infrared in subsection 3.1.2.

### 3.1.1. Equivalent Width Measurements

We first assume that there is no significant contamination of the SS Cyg donor star spectrum. We plot results in  $JHK$  for both solar (Fig. 4abc), and subsolar ( $[\text{Fe}/\text{H}] = -0.3$ , Fig. 5abc) models. The strong magnesium deficit is apparent for both metallicities in all three bandpasses. The subsolar model (with  $\text{Hd} = 0\%$ ) provides the better fit to all of the lines across the three wavebands. In the  $J$ -band, however, the subsolar fit would be improved if the donor star were slightly hotter:  $T_{\text{eff}} \sim 5000$  K. Evidence for differential contamination. For the solar metallicity results to reproduce the data for SS Cyg, a hotter donor star would be required regardless of bandpass. In the  $H$ - and  $K$ -bands, a donor with  $T_{\text{eff}} = 5000$  K produces a reasonable match between the observations and models. In the  $J$ -band, however, a temperature of 5250 K, or higher, would be required for the solar

abundance model to provide a sensible fit. Unless there is a source of contamination, or the previously derived donor star temperature is incorrect, it appears that a solar abundance for the secondary star in SS Cyg can be excluded.

Using just the results from the  $J$ -band, we would conclude that  $T_{\text{eff}} \sim 5250$  K, and the donor star in SS Cyg has a large enhancement of both sodium and carbon. In the  $H$ -band, the iron line appears to be weaker in SS Cyg than found for either abundance, but the continuum bandpasses for this line includes both H I Br19 and Br18. In SS Cyg, these high order hydrogen lines are sufficiently strong to affect the weak Fe I line. There appears to be an aluminum deficit for both metallicities in the  $K$ -band, but this line is corrupted by He I emission in SS Cyg. The measured EQW of the aluminum line in the  $H$ -band agrees with the subsolar metallicity model. The abundance of sodium appears to be enhanced in the  $K$ -band for the lower metallicity model. There is an Na I doublet in the  $H$ -band. This feature is weak compared to those in the  $J$  or  $K$ -bands, but will become more relevant, below. For SS Cyg, our program was unable to measure an EQW for this doublet due to H I emission.

From this analysis we would conclude that the donor in SS Cyg has a subsolar metallicity, with a normal abundance *pattern*, except for the presence of a magnesium deficit, and an enhancement in the sodium abundance. These results closely reflect those of HM17, except that the sodium enhancement found here is about one half ( $[\text{Na}/\text{Fe}] = +0.2$ ) of what they found. As noted above, one possible cause of this is the fact that the  $\chi^2$  analysis is more reliant on the relative continuum levels between the models and the data, and this requires an accurate continuum division for the CV spectrum. This is especially true since they included the red Na I doublet in the  $K$ -band to derive the sodium excess. With CO absorption, defining the actual continuum near this feature is challenging. The EQW results do suggest that a slightly hotter donor star,  $T_{\text{eff}} \sim 4875$  K, would produce

better fits across the three bandpasses at  $[\text{Fe}/\text{H}] = -0.3$ .

### 3.1.2. A Broader Level of Contamination?

For the  $J$ -band, an increase in the level of contamination would improve the fit to most of the lines for that bandpass. It is impossible to quantify the exact level of contamination while allowing the value for the metallicity to float without some type of additional constraint. To derive this constraint we employ the near-infrared light curves of SS Cyg. To the  $JHK$  data from Harrison et al. (2007), we add the 3.4 and 4.5  $\mu\text{m}$  photometry from *WISE* and *NEOWISE*, and model the combined data set with WD2010.

For the ellipsoidal variations of Roche-lobe filling CV secondary stars, the deeper of the two light curve minima often occurs at phase 0.5. This is because at this time we are viewing the hemisphere of the donor star that extends further from the center of the secondary, and it is cooler. The ratio of the two minima is almost completely dependent on the temperature ratio of the two stars. A very hot white dwarf can irradiate the secondary, and raise the temperature of the distorted hemisphere. As can be seen in Fig. 6, the observed minima in the  $K$ -band light curve of SS Cyg have similar depths. This implies a *small* amount of irradiation of the donor. We fix the temperature of the secondary star to  $T_{\text{eff}_2} = 4750$  K. This then requires  $T_{\text{eff}_1} = 20,000$  K to match the depths of the two minima. This temperature is lower than that typically reported for SS Cyg from modeling UV spectroscopy,  $T_{\text{eff}} \approx 35,000$  K (c.f., Urban & Sion 2006). Such a high temperature for the white dwarf would decrease the depths of the secondary minima to smaller than what is observed. With no contamination (“no third light” in the parlance of light curve modeling), we derive a best-fitting orbital inclination of  $i = 35^\circ$  for SS Cyg.

We now add a contaminating source that is present at all phases, and has no bandpass

dependency. For a third light component that supplies 25% of the flux (at  $\phi = 0$ ), the best fitting model (plotted in red in Fig. 6), has  $i = 45^\circ$ . For a contamination level of 50%, the orbital inclination has to be  $i = 55^\circ$  for the model to match the observations. The latter level of contamination is what was found by Bitner et al. (2007) for the visual part of the spectrum. Such a large contamination level is unreasonable. The spectral energy distribution of the donor in SS Cyg peaks in the near-IR, thus relative to the optical flux, it should dominate the infrared luminosity. It is also difficult to reproduce the observed near-IR colors of SS Cyg with such a large contamination component. We conclude that the contamination level is near 25%.

Because we do not have *JHK* light curves for all of our sources, it is worthwhile to investigate the utility of the *WISE/NEOWISE* light curve data for estimating contamination. The same model used above was run for the two *WISE/NEOWISE* bandpasses. Assuming  $(W1 - K) = 0.07$ , and  $(W2 - K) = 0.0$  for the  $\sim K3.5V$  secondary star (see Pecaut & Mamajek 2013), the resulting model light curves exactly fit the lower envelope of the *WISE/NEOWISE* data in both bands. Note that SS Cyg was at minimum for all of the data collected by *WISE* and *NEOWISE* (though some data sets occurred just a few days before an outburst, or within a few days of returning to minimum). Thus, the large amplitude variations above the light curve model are due to intrinsic processes occurring within the binary system *during quiescence*. It is curious that the level of variability is much smaller at both inferior *and* superior conjunctions. The amplitude of the variability in the *W3* bandpass ( $11.3 \mu\text{m}$ , not plotted) is about twice that seen in *W2*. Dubus et al. (2004) explored the mid-infrared variability of SS Cyg, and had attributed it to free-free emission from expanding clouds. Given the radio detection of SS Cyg by Körding et al. (2008), perhaps SS Cyg is also a synchrotron source in quiescence.

We now repeat the EQW analysis using a contamination level of 25% in each bandpass.

As shown in Fig. 7abc, the resulting, best fit metallicity for SS Cyg is  $[\text{Fe}/\text{H}] = 0.0$ . The strong magnesium deficit, and the enhancement of sodium described above, remain. The remainder of the data set is fully consistent with a solar abundance pattern. Increasing the contamination level in the  $J$ -band would aid the fit of the data to the models. In the case of SS Cyg, the subsolar metallicity derived by H16 and HM17 is due to contamination. However, neither their derived temperature for the donor in SS Cyg, or the relative elemental abundance anomalies they found, are strongly affected by the observed level of contamination. There is no evidence to support a non-solar value for the (photospheric) hydrogen abundance.

### 3.2. DX Andromedae

DX And is a U Gem type dwarf nova of long period,  $P_{\text{orb}} = 10.57$  hr. DX And was observed using GNIRS on Gemini North. Bruch et al. (1997) and Drew et al. (1993) found that the secondary star has a spectral type near K1. Bruch et al. present an ephemeris for this object obtained from a radial velocity study. Their analysis suggested a mass ratio of  $q = 0.66 \pm 0.08$ , while Drew et al. found  $q = 0.96$ . If the former is true, the secondary star would have an unusual mass,  $M_2 = 0.53 M_{\odot}$ , for its spectral type ( $M_{\text{K1V}} = 0.8 M_{\odot}$ ; Henry & McCarthy 1993). The larger value for  $q$  would imply a more normal mass for the donor star, if the white dwarf mass was similar to that found in the typical CV ( $\langle M_{\text{WD}} \rangle = 0.8 M_{\odot}$ ; Knigge et al. 2011). From a sparse set of photometry, Drew et al. estimated an orbital inclination of  $45^\circ$ , and a contamination level of 15% in the visual. They also derived a rotational velocity of  $v \sin i = 79 \pm 5 \text{ km s}^{-1}$ , and we have used this value in generating the model spectra.

In Fig. 8, we present a partial  $JHK$  light curve, along with the photometry from *WISE/NEOWISE*. Given the poorly known system parameters, we set  $T_1 = 25,000 \text{ K}$ ,

and  $T_2 = 5000$  K, and used the larger value for  $q$ . In the model light curve (red) presented in Fig. 8, we have set the contamination level in all bands to zero. An inclination angle of  $i = 45^\circ$  provides a reasonable fit to the data. Any flaring in  $W1$  and  $W2$  bands is much smaller than seen in most of the CVs of our program, suggesting that the accretion disk is relatively unimportant in the near-IR. We will assume no contamination.

Using equation 2.3b in Warner (1995), the mean density of the donor in DX And is  $\langle \rho \rangle \simeq 0.96 \text{ gm cm}^{-3}$ . Using data in Boyajian et al. (2012), a K1 dwarf should have  $\langle \rho \rangle \simeq 2.2 \text{ gm cm}^{-3}$ . The donor in DX And has a density that suggests it is evolved. The *Gaia* Data Release 2 (“DR2”) parallax (*Gaia* Collaboration 2018) gives a distance to DX And of 600 pc. The light curve shows that  $\langle K \rangle = 12.35$ , and assuming the donor supplies 100% of the observed luminosity, implies  $M_K = 3.46$ . The secondary star in DX And is 1.79 times more luminous than a main sequence K1V (Houk et al. 1997), suggesting a radius that is  $1.34 \times$  that of a K1V. For such an object, *if* it has the mass of a normal K1V ( $0.8 M_\odot$ ),  $\log g = 4.28$ , well below that for a main sequence dwarf.

Using a solar metallicity, we find that all of the lines, except those of Mg I, are stronger than expected whether  $\log g = 4.5$  or  $4.0$  (Fig. 9abc). For the dwarf model ( $\log g = 4.5$ ), the best explanation at  $[\text{Fe}/\text{H}] = 0.0$  is that the donor suffers from a hydrogen deficit of at least 25%. For the subgiant model ( $\log g = 4.0$ ), the best fit occurs for a hydrogen deficit of 50%. In either case magnesium is deficient, while the sodium abundance is enhanced. The only plausible alternative to a hydrogen deficit is a large, super-solar metallicity. The highest metallicity we have in our grid is  $[\text{Fe}/\text{H}] = +0.50$ , and models with this value do a very poor job at reproducing the measured equivalent widths, with deficits of some elements, and enhancements of others. *While the results for both gravities are consistent across the three bandpasses for single values of the hydrogen deficit.*

We conclude that the donor star in DX And is truly hydrogen deficient. This result

explains the stronger than expected absorption features found by Drew et al. (1993), and enhanced strength of the absorption lines of Ca I and Cr I noted by Bruch et al. (1997). The Gemini GNIRS spectrum of DX And is presented in Fig. 11, where we compare it to a model spectrum with  $T_{\text{eff}} = 5000$  K,  $\log g = 4.0$ ,  $[\text{Fe}/\text{H}] = 0.0$ , and  $\text{Hd} = 50\%$ . Using the  $\chi^2$  analysis, we derive the following abundances for the  $\log g = 4.0$ :  $[\text{C}/\text{Fe}] = -0.7$ ,  $[\text{Mg}/\text{Fe}] = -0.2$ , and  $[\text{Na}/\text{Fe}] = +0.5$ . The model plotted in Fig. 11 includes those abundance anomalies. For  $\log g = 4.5$ , the abundances are  $[\text{Fe}/\text{H}] = 0.0$ ,  $\text{Hd} = 25\%$ ,  $[\text{C}/\text{Fe}] = -0.5$ ,  $[\text{Mg}/\text{Fe}] = -0.5$ , and  $[\text{Na}/\text{Fe}] = +0.3$ .

### 3.3. RX Andromedae

RX And is an interesting system in that it has dwarf novae eruptions, what appear to be Z Cam-like standstills, and deep minima like VY Scl stars (Schreiber et al. 2002). The Ritter-Kolb Catalog (“RKCcat”, Ritter & Kolb 2003) has the following parameters listed for the RX And system:  $M_1 = 1.14 M_{\odot}$ ,  $M_2 = 0.48 M_{\odot}$ ,  $i = 51^{\circ}$ , and a spectral type of K5 for the donor. Using these parameters we calculate that the rotational velocity of the secondary star should be  $v \sin i = 101 \text{ km s}^{-1}$ . The SPEX data do not have sufficient resolution to provide a robust value for this parameter. Using absorption lines in the *I*-band, however, where the dispersion is  $2.02 \text{ \AA/pix}$ , we find a value of  $v \sin i = 96 \pm 20 \text{ km s}^{-1}$  for RX And. To model RX And, we generated a grid of synthetic spectra with  $v \sin i = 100 \text{ km s}^{-1}$ .

The temperature of the secondary in RX And appears to be ambiguous. While the RKCcat lists a spectral type of K5, H16 found that the donor appeared to be an M-type star. The routine they used to derive metallicities and temperatures for M dwarfs found a value of  $[\text{Fe}/\text{H}] = +0.07$  and a spectral type of M2. RX And has strong Na I and Ca I absorption, with equivalent widths of  $5.35 \text{ \AA}$  and  $4.18 \text{ \AA}$ , respectively. For main sequence dwarfs, the equivalent width of the Na I doublet does not become larger than that for the

Ca I triplet until the spectral type is later than  $\sim$  M1V. H16 found that if the spectral type is earlier than M2, the donor star has a subsolar metallicity. An alternative explanation is that the donor star has a large excess of sodium, and its flux is diluted by emission from the non-stellar components in the system.

We use the *WISE/NEOWISE* light curves to explore the issue of contamination. We only use those data for when RX And was at a minimum (two of the six NEOWISE epochs occurred during maxima). The *WISE/NEOWISE* light curves in the W1 and W2 bands both show random variations of  $\Delta m = 0.5$  mag. It is likely that there is a significant level of contamination. The orbital ephemeris for RX And has been published by Kaitchuck (1989), and we phased the *WISE/NEOWISE* photometry using their result. We used WD2010 to generate a light curve setting  $T_{\text{eff}_2} = 4500$  K (K5V). Sepinsky et al. (2002) quote a temperature for the white dwarf of 34,000 K. With  $i = 51^\circ$ , a light curve assuming no contamination has too large of an amplitude to explain the observed photometry. If we use a contamination level of 50%, we can better match the lower envelope of the W1 and W2 data sets. If we use  $T_{\text{eff}_2} = 3500$  K (M2V) we again find that the amplitude of the variations is too large for  $i = 51^\circ$  without a third light component. In this case, a contamination level of 30% is consistent with the lowest values in the *WISE/NEOWISE* photometry throughout the orbit.

The EQW analysis for RX And, assuming that  $T_{\text{eff}} \geq 4000$  K, is wildly inconsistent. It requires a contamination of 30% to get calcium, aluminum and iron within the error bars of the measurements for RX And in the *K*-band. In this scenario sodium would have an enormous excess, while magnesium has a very large deficit. In the *J*-band, a 30% contamination level is only consistent with the Al I datum. Sodium, potassium and manganese would have excesses, while silicon, magnesium and iron would have deficits. *The donor in RX And is not a K-type dwarf.*

To attempt to constrain the secondary in RX And, we decided to apply our EQW measurement programs to the M dwarfs in the IRTF Spectral Library. While blindly applying our programs to these M dwarfs could be quite dangerous due to the number of molecular features found in the spectra of M dwarfs, we think the results are quite illuminating. In Fig. 12abc we present the results for the three bandpasses, plotting EQW versus spectral type. In addition, we separate the M dwarfs into those with  $[\text{Fe}/\text{H}] > 0$  (red), and those with  $[\text{Fe}/\text{H}] < 0$  (blue). In the *J*-band, assuming the donor is an M2, the only anomalies are deficits of magnesium and aluminum, and an enhancement of manganese. Given the possibility of intrinsic water vapor absorption at the red end of the *J*-band, peculiar values for the EQWs of manganese might be expected. In the *H*-band, the only peculiarity is a deficit of magnesium. This is also true in the *K*-band *if* the donor in RX And has a solar metallicity.

Given that there is probably significant contamination of the spectrum of the donor in RX And, the true EQW measurements would be somewhat larger than plotted in Fig. 12abc. A 25% contamination level results in EQW measurements that are 75% the depth of those without contamination. We conclude that the best fit spectral type for the secondary in RX And is an M2, and it has a near-solar abundance. It appears to have normal levels of sodium, with a deficit of magnesium. An M2 spectral type with solar abundance requires a sizeable carbon deficit,  $[\text{C}/\text{Fe}] \leq -0.3$ .

### 3.4. AE Aquarii

HM17 found that the donor in AE Aqr has a very low carbon abundance, and likely has a small value for the isotopic ratio of carbon:  $^{12}\text{C}/^{13}\text{C} = 4$ . They found for their  $\log g = 4.5$  (“dwarf”) model values of  $T_{\text{eff}} = 5000$  K,  $[\text{Fe}/\text{H}] = 0.0$ ,  $[\text{C}/\text{Fe}] = -1.4$ ,  $[\text{Mg}/\text{Fe}] = 0.0$ , and  $[\text{Na}/\text{Fe}] = +0.5$ . For the  $\log g = 4.0$  (“subgiant”) model they found  $T_{\text{eff}} = 4750$  K,  $[\text{Fe}/\text{H}]$

$= 0.0$ ,  $[\text{C}/\text{Fe}] = -1.7$ , and  $[\text{Na}/\text{Fe}] = +0.52$ . We adopt the HM17 carbon abundances for the two gravities in the following. The equivalent width analysis for the dwarf model with  $[\text{Fe}/\text{H}] = 0.0$  leads to the conclusion that the donor in AE Aqr has a hydrogen deficit of 25%, a small deficit of magnesium, and an excess of sodium (Fig. 13abc). In all three bandpasses, slightly better fits of the data to the models (less magnesium) occurs if we lower the temperature of the donor in AE Aqr to  $T_{\text{eff}} \simeq 4750$  K. A model with  $[\text{Fe}/\text{H}] = +0.1$  also reduces the need for a hydrogen deficit at  $T_{\text{eff}} = 5000$  K in the  $H$ - and  $K$ -bands, but worsens the fit in the  $J$ -band. Obviously, a higher metallicity lowers any sodium excess, while making the magnesium deficit more severe.

Given the long orbital period of AE Aqr, 9.88 hr, it is likely that the secondary star has a lower gravity than that of a dwarf (see HM17). Using a solar abundance, subgiant model, we find that the most likely solution (see Fig. 14abc) at  $T_{\text{eff}} = 4750$  K is one where the donor star has a 25% deficit of hydrogen. In this scenario the abundance of sodium is enhanced, while the magnesium abundance is close to normal. The one deviation from this result is that potassium seems to be underabundant. Increasing the metallicity to  $[\text{Fe}/\text{H}] = +0.2$  creates a better match between models and the data for Mg I, Ca I, and Al I in the  $H$ - and  $K$ -bands. It also reduces the excess of sodium. The fit of this solution to the observed  $J$ -band equivalent widths is much worse. A significant level of contamination in the  $J$ -band would be needed to make such a model work.

It appears that either the donor in AE Aqr is hydrogen deficient, or that the metallicity is super-solar. It is impossible to decide between these alternatives without knowing the contamination level. Welsh et al. (1995) found that the contamination of the donor star by the white dwarf and accretion disk was very low for AE Aqr in the red ( $\sim \lambda 6600$  Å), with the secondary supplying 94% of the luminosity for the donor star temperatures we have derived. This would suggest that it is unlikely that the  $J$ -band suffers from a

large contamination component. Unfortunately, there has been very little near-infrared photometry published for AE Aqr. The only near-IR light curve that we have found is from Tanzi et al. (1981); they observed it in the  $K$ -band, covering 30% of an orbit. That light curve is consistent with pure ellipsoidal variations.

It is well known that AE Aqr is variable in the mid-infrared (see Dubus et al. 2004, Abada-Simon et al. 2005). This variability has been ascribed to free-free emission from expanding clouds, a synchrotron source, or a combination of both. Fortunately, sufficient *WISE* and *NEOWISE* observations exist to better probe the infrared variability of this source. In Fig. 15 we plot the *WISE* four band photometry, and the *NEOWISE* two band data. There does not appear to be any offset between the overlapping data sets. Using the system parameters derived by Hill et al. (2014), we have used WD2010 (with  $i = 50^\circ$ ) to generate a set of light curve models for AE Aqr. The  $W1$  bandpass shows clear ellipsoidal variations, but with excursions of  $\sim 20\%$  from the model baseline. The amplitude of the random variations is larger in the  $W2$  band, and a non-stellar source dominates the light curves in the  $W3$  and  $W4$  ( $22\ \mu\text{m}$ ) bands.

The strong wavelength dependence suggests that the source of the variation is relatively unimportant in the  $J$ -band, while contributing  $\sim 10\%$  to the  $K$ -band flux during flaring events. Ignoring the possibility of contamination, for the dwarf model, a value of  $[\text{Fe}/\text{H}] = 0.0$  with  $\text{Hd} = 25\%$  reproduces most of the observations *if* the temperature is  $T_{\text{eff}} = 4750$  K. In this solution, the sodium abundance is super-solar, and magnesium is deficient. For the subgiant models, the best fit occurs for a hydrogen deficit of 25%, with an enhanced abundance of sodium, but a normal abundance for magnesium. HM17 calculated that the expected gravity for the donor in AE Aqr was intermediate between the dwarf and subgiant models that we have used here, suggesting the true solution lies somewhere between our two results. It does appear, however, that the donor in AE Aqr has a modest hydrogen deficit.

### 3.5. Z Camelopardalis

Z Cam is the proto-type of a small family of CVs that show “standstills” in their outbursts (see Simonsen et al. 2014). The RKCats lists the following parameters for the system:  $P_{\text{orb}} = 0.2898406$  d,  $M_1 = 1.00 \pm 0.06 M_{\odot}$ ,  $M_2 = 0.77 \pm 0.03 M_{\odot}$ , and  $i = 57^{\circ}$ . The last three parameters come from Shafter (1983). While Kraft et al. (1969) believed the secondary star had a G spectral type, Wade (1980) lists the spectral type as K7. Thorstensen & Ringwald (1995) have published the most recent ephemeris for Z Cam. We downloaded the *WISE/NEOWISE* data to evaluate the orbital inclination. There were eight epochs of observations, but the AAVSO data base shows that only two, those for 2014 October 10 and 2015 October 10, were obtained during minimum light ( $V \geq 13$ ). We plot the data for these two epochs in Fig. 16, with the data for 2014 plotted in red, and that for 2015 plotted in green. The photometry for the 2014 observation appeared to be 0.17 mag brighter than that for 2015. This mirrored the visual light curve data that showed the system to be  $\sim 0.2$  mag brighter in the 2014 epoch versus the 2015 epoch.

We used the system parameters to generate model light curves using WD2010. Hartley et al. (2005) found that the white dwarf in Z Cam appeared to be very hot,  $T_{\text{eff}} = 57,000$  K, though a model with  $T_{\text{eff}} = 26,000$  K also appeared to fit the data. We set the white dwarf temperature to 26,000 K as there is little evidence for intense irradiation in the mid-infrared light curves. As we will discuss below, the secondary star in Z Cam appears to be an early M dwarf. We set the temperature of the secondary star to 3575 K. An orbital inclination of  $57^{\circ}$  is not consistent with the *NEOWISE* data unless there is a contamination level of  $\sim 30\%$  in each band (see Fig. 16). If we assume that there is no contamination, we find that the best fit for the orbital inclination is  $i = 40^{\circ}$ . The 2MASS photometry of Z Cam was obtained during minimum light and, at an orbital phase of  $\phi = 0.55$ , had the following colors:  $(J - H) = 0.53$ , and  $(H - K) = 0.18$ . These suggest a K4

spectral type, and such an object should have  $(K - W1) = 0.08$ . For Z Cam, at  $\phi = 0.55$ ,  $(K - W1) = 0.12$ . A secondary with  $T_{\text{eff}} = 3575$  K would have  $(J - H) = 0.66$ ,  $(H - K) = 0.19$ ,  $(K - W1) = 0.14$ . For the M spectral type to agree with the photometry requires some level of contamination in the near-infrared.

To construct a synthetic spectral grid for Z Cam requires a value of  $v \sin i$ . Using the parameters listed above, for  $i = 57^\circ$ , we calculate  $v \sin i = 117 \text{ km s}^{-1}$ . For  $i = 40^\circ$ , we get  $v \sin i = 89 \text{ km s}^{-1}$ . Unfortunately, the resolution of our spectra is insufficient to decide between these two. Using four isolated lines in the  $J$ -band, we get  $v \sin i = 91 \pm 26 \text{ km s}^{-1}$ . Hartley et al. argue that a higher inclination than  $i = 57^\circ$  would produce a better match to their UV data. We will assume an inclination of  $57^\circ$ , and use  $v \sin i = 117 \text{ km s}^{-1}$  for generating the grid.

The results of the EQW analysis are inconsistent. The main deviations appear to be a significant enhancement of sodium and a deficit of magnesium. The data appear to be most consistent with an object that has  $T_{\text{eff}} = 4500$  K, and a small hydrogen deficit. If the temperature of the donor is slightly cooler,  $T_{\text{eff}} = 4250$  K versus  $T_{\text{eff}} = 4500$  K, the need for a hydrogen deficit is diminished. The strong sodium excess and magnesium deficit, however, remain. At temperatures much higher or lower than 4500 K, the match to the CO features becomes very poor. We also attempted more metal-rich models, and found that synthetic spectra with  $T_{\text{eff}} = 4500$  K,  $\text{Hd} = 0\%$ , and  $[\text{Fe}/\text{H}] = +0.3$  do a reasonable job at reproducing the data. In this case, however, the CO features are much stronger than seen in Z Cam, and would require a large carbon deficit. There does not seem to be a robust solution assuming the donor is a K dwarf.

If we apply the metallicity program used for the M-dwarfs in H16 to the  $K$ -band spectrum of Z Cam, we derive a spectral type of M1.6, and  $[\text{Fe}/\text{H}] = +0.03$ . The spectral type determined by this routine uses a “water vapor index” (see Covey et al. 2010) that

is calculated using the ratios of three different continuum bandpass fluxes (21800 – 22000 Å, 22700 – 22900 Å, and 23600 – 23800 Å). The only strong line in these bandpasses is Mg I at 22820 Å. As we did for RX And, we compare the EQW measurements for Z Cam to those of M dwarfs in Fig. 17abc. The results are fully consistent across the three bandpasses. The only deviation appears to be the enhanced strength of Mn I, but this is almost certainly due to the continuum division process, with the added complication of water vapor absorption in the donor.

In Fig. 18, we compare the *JHK* spectra of an M1V (HD 42581) from the IRTF Spectral Library to that of Z Cam. Using the metallicity program, we derive a value of  $[\text{Fe}/\text{H}] = +0.12$ , and a spectral type of M1.3 for HD 42581. The match between the two sources is excellent, including the CO features in the *K*-band. The donor star of Z Cam does not appear to show *any* abundance anomalies. It is, however, surprising that an object with a longer orbital period than SS Cyg, has a donor that is 1000 K cooler. The parallax of Z Cam from the *Gaia* DR2 is  $\pi = 4.467 \pm 0.05$  mas. With  $K = 10.85$  from the 2MASS catalog,  $M_K = 4.11$ . An M1.3V should have  $M_K \sim 5.55$ . Note that due to its brightness, “G” < 12, systematic effects in the *Gaia* data analysis could lead to an actual error bar of  $\pm 0.3$  mas for Z Cam (Lindgren et al. 2018). Even assuming this large of an error bar, and moving Z Cam to 186 pc ( $\pi + 3 \sigma$ ), the system has  $M_K = 4.5$ . The donor star in Z Cam is much more luminous than a main sequence M dwarf.

### 3.6. SY Cancri

The long period Z Cam system SY Cnc is unusual in that it has a mass ratio greater than one; Casares et al. (2009) found  $q = 1.18 \pm 0.14$ . Casares et al. refined the orbital period and ephemeris for SY Cnc, measured  $v \sin i = 75.5 \text{ km s}^{-1}$ , and derived a spectral type of G8  $\pm 2$  ( $T_{\text{eff}} = 5500 \text{ K}$ ) for the donor. H16 found that the donor in SY Cnc

was completely normal, with  $T_{\text{eff}_2} = 5500$  K,  $[\text{Fe}/\text{H}] = 0.0$ , and  $[\text{C}/\text{Fe}] = 0.0$ . At the epoch of the observations used by H16, the system had  $V = 12$ , and was declining from an outburst that had peaked four days earlier. That spectrum must have a considerable level of contamination, weakening the depth of any absorption features. It is likely that the spectral type of the donor is cooler than derived in H16. The new cross-dispersed spectrum obtained with TripleSpec, analyzed below, occurred when the system had  $V = 11.8$ .

There is only a rough estimate for the orbital inclination. Casares et al. use the mass function,  $M_1 \sin^3 i = 0.13 \pm 0.02 M_\odot$ , to derive the following limits:  $26^\circ \leq i \leq 38^\circ$ . We are not aware of any infrared light curves of this source, so we downloaded the *WISE/NEOWISE* data to investigate the system. There are three epochs of data when SY Cnc was in quiescence ( $V \gtrsim 13$ ): 2010 April 28, 2016 April 18, and 2016 November 4. The latter of these was just as SY Cnc began an outburst, having  $V = 13.2$ . The light curves, Fig. 19, in both bandpasses are quite noisy, though there are clearly ellipsoidal variations present.

We use WD2010 with  $T_{\text{eff}_1} = 20,000$  K, and  $T_{\text{eff}_2} = 5500$  K,  $q = 1.18$ , and  $M_2 = 0.9 M_\odot$  to generate model light curves. We find that the best fitting inclination is  $i = 55^\circ$ . Given the observed variability, it is likely that there is a small amount of contamination, and the true inclination is likely higher. This might pose a conundrum. Given the radial velocity solution by Casares et al., if our derived inclination was correct, the white dwarf would have an extremely low mass:  $0.24 M_\odot$ ! As shown in Fig. 19, the  $38^\circ$  upper limit established by Casares et al. is consistent with the envelope of the faintest data points, but *only if* there is no contamination. This latter inclination implies a white dwarf mass of  $0.58 M_\odot$ , somewhat lower than typically found in CVs. This then leads to  $M_2 = 0.66 M_\odot$ , a mass more typical of late K-type main sequence stars, than late G (note, changing the input masses for WD2010 to these lower values increases the amplitude of the variations by

0.01 mag).

Given that our spectroscopy was not obtained during quiescence, we need to estimate a contamination level. The *NEOWISE* observation that began on 2015 November 6 occurred at a time when  $V = 11.7$ . At  $\phi = 0$ , the  $W1$  and  $W2$  magnitudes in outburst were 0.48 mag brighter than their quiescent values. This suggests that at this time, the donor star only contributed 40% of the infrared flux. We assume this contamination level, and find *globally* that the EQW measures of SY Cnc, Fig. 20abc, are consistent with  $T_{\text{eff}} = 5500$  K, and  $[\text{Fe}/\text{H}] = 0$ . Magnesium appears to be slightly underabundant. The presence of numerous emission/noise features corrupts several of the measurements, including Al I and Fe I in the  $K$ -band, and Al I, K I, Si I, and Fe I in the  $J$ -band.

Plotting the spectrum of SY Cnc versus the best fitting model from the EQW analysis, finds that the CO features in the synthetic spectrum are too weak. Assuming the same contamination level, we find that synthetic spectra with a temperature of  $T_{\text{eff}} = 5250$  K are a better match to the data in the  $K$ -band. However, such a spectrum is not as good of a match to the  $J$  and  $H$ -band spectrum without additional contamination. This can be seen in the EQW plots, where the observed Na I and Ca I measures are too large in the  $K$ -band, but not overtly so in the  $J$  and  $H$ -bands. For the synthetic spectrum in Fig. 21, we have used a contamination level of 60% in the  $K$ -band, 70% in the  $H$ -band, and 75% in the  $J$ -band, to achieve a reasonable match to the observations. The prominence of the donor and brightness of the system in the near-IR would enable high resolution observations, allowing a more robust measurement of  $v \sin i$  to confirm the nature of this unusual system. Phase-resolved  $JHK$  photometry during quiescence is needed to better constrain the orbital inclination.

### 3.7. EM Cygni

H16 only had  $K$ -band spectra of EM Cyg, finding a subsolar metallicity and a small carbon deficit. Here we have cross-dispersed  $JHK$  spectra, plotted in Fig. 22, obtained with GNIRS on Gemini. The AAVSO light curve for EM Cyg shows that it was in quiescence with  $V \simeq 13.4$  at the epoch of the Gemini observations. North et al. (2000) showed that there is a third star, of similar spectral type as the donor star, that contaminates the light of the system. By subtracting this star out, they were able to solve for the system parameters. We have used the values they found ( $M_1 = 1.12 \pm 0.08 M_\odot$ ,  $M_2 = 0.99 \pm 0.08 M_\odot$ ,  $q = 0.88$ , and  $i = 67^\circ$ ) to set up WD2010 for modeling the *WISE* and *NEOWISE* light curves of EM Cyg. North et al. found that the donor and contaminating star had very similar contributions to the luminosity at  $6500 \text{ \AA}$ , with the donor supplying 7% more flux. For light curve modeling, we add a third component that has exactly 50% of the total light. We set the white dwarf temperature to 20,000 K, and the secondary to 4500 K.

The resulting light curve is shown in Fig. 23. During the *WISE* observations, the AAVSO data base show that EM Cyg had  $V = 13.2$ , a few tenths of a magnitude brighter than its typical minimum light value, though well above its rare, deep minima at  $V = 14.5$ . There were six epochs of *NEOWISE* data, but only two of those were during times when  $V \sim 13.0$ . In Fig. 23, the *WISE* photometry is plotted in black, and the two separate *NEOWISE* epochs are in green (2014 Oct 24) and red (2015 Oct 18). To achieve overlap between the light curves, we added 0.06 mag to the  $W1$  photometry for the 2014 observations, and subtracted  $-0.095$  from the 2015 data. For  $W2$  these offsets were 0.0 mag, and  $-0.13$  mag, respectively. The solid line in this figure is the model light curve for a 50% contamination by the interloping star. The dashed line is with no third light component. To explain the light curves requires a contaminating source that supplies  $\sim 50\%$  of the total mid-infrared flux.

The excursions from the model light curves,  $\Delta m \sim \pm 0.1$  mag, during the epochs when  $V \sim 13$ , suggest a low (non-stellar) contamination level. When adding-in the *NEOWISE* data from the epochs when EM Cyg was brighter than  $V = 13$ , the *W1* photometry has maxima that reach to  $W1 = 10.8$ , while maintaining the same floor of  $W1 = 11.2$ . While there are few data points, the minimum at  $\phi = 0$  in the *W1* light curve is suggestive of an eclipse. Perhaps the inclination angle is larger than derived by North et al.

North et al. found a rotation velocity of  $v \sin i = 140 \pm 6 \text{ km s}^{-1}$ . We have broadened our model grid using this value. The EQW measurements for EM Cyg, Fig. 24abc, are completely consistent with a solar abundance for  $T_{\text{eff}} = 4500 \text{ K}$ . There are several deviant values that can be resolved by looking at the spectra in Fig. 22. The EQW for Al I in the *K*-band suggests a strong deficit, but this feature is compromised by He I emission. The EQW for the Ca I triplet suggests an enhanced abundance. The spectra show a slightly deeper Ca I triplet than the model, perhaps due to the presence of narrow absorption features from the contaminating star. The profile of the Mg I line in the *K*-band was corrupted during the telluric correction, and it appears broader and deeper than it actually should be. The Mg I line in the *H*-band suggests a deficit, while that in the *J*-band suggests a normal abundance. The Al I doublet in the *J*-band has a much smaller equivalent width than expected for a solar abundance. The Al I line in the *H*-band, however, appears to be normal. Presumably this contradiction is simply due to low S/N and a poor telluric correction at the red end of the *J*-band.

With the cross-dispersed data, we use the techniques in H16 to construct a model for EM Cyg. The best fitting temperature is  $T_{\text{eff}_2} = 4500 \pm 150 \text{ K}$ . We find that carbon and magnesium suffer identically sized deficits:  $[\text{C}/\text{Fe}] = -0.5 \pm 0.02$ , and  $[\text{Mg}/\text{Fe}] = -0.5 \pm 0.1$  (using just the *H*-band spectrum). If the contaminating star is a normal field dwarf of solar abundance, then the carbon and magnesium deficits in the secondary of EM Cyg

would be about twice those just found. It will take higher resolution spectroscopy for a more robust measurement of the abundances of the donor in EM Cyg.

### 3.8. EY Cygni

EY Cyg is a long period ( $P_{\text{orb}} = 11.0$  h) U Gem-type dwarf nova. Echevarría et al. (2007) conducted a radial velocity study of the system and found  $M_1 = 1.1 \pm 0.09 M_{\odot}$ , and  $M_2 = 0.49 \pm 0.09 M_{\odot}$ . They estimated a spectral type of K0 for the secondary, and limited the orbital inclination to  $i = 14^{\circ} \pm 1$ . Echevarría et al. note that the secondary star has a much larger radius than a main sequence dwarf. Using their parameters, we estimate  $\log g \simeq 4.2$ . As might be expected, the *WISE/NEOWISE* light curves show no evidence for ellipsoidal variations, with only random, small scale variability of  $\leq \pm 0.2$  mag in both *W1* and *W2*. We will assume that the contamination level is insignificant.

The results from H16 were  $T_{\text{eff}_2} = 5250$  K (= K0),  $[\text{Fe}/\text{H}] = 0.0$ , and  $[\text{C}/\text{Fe}] = -0.5$ . Echevarría et al. measured  $v \sin i = 34 \pm 4$  km s $^{-1}$ , and we have used this value to generate the synthetic spectral grid. From that grid we find that the donor star in EY Cyg has a significant hydrogen deficit. For the dwarf gravity, we find that  $\text{Hd} \geq 25\%$ , while for the subgiant gravity (see Fig. 25abc),  $\text{Hd} \simeq 50\%$ . At both gravities, magnesium is slightly underabundant, and sodium has a significant excess. Sion et al. (2004) found a large N V/C IV ratio. The carbon deficit we find is consistent with this result, and suggests a nuclear evolved donor. Sion et al. also found a very low abundance of silicon (10% solar) from *FUSE* and *HST* spectroscopy, but from our measurements, the silicon abundance does not appear to be unusual. Due to the lower S/N ratio of the SPEX data for EY Cyg, the error bars on the EQW measurements are significant. However, the results were consistent across all three bandpasses. We attempted to fit higher metallicity models but, like DX And, the measured EQWs were discordant. The best fit of any of the higher metallicity models for

$\log g = 4.0$  occurred with  $[\text{Fe}/\text{H}] = +0.3$ .

Smaller hydrogen deficits are possible if the donor star has a much lower temperature; at  $T_{\text{eff}_2} = 4750$  K, there is no hydrogen deficit. Such a temperature is substantially different from that derived by H16, or the K0 spectral type assigned to the donor by both Echevarría et al. and Kraft (1962). Given the low inclination, it is worth noting that we are looking at the pole of the secondary in EY Cyg, and at this viewing angle, the donor probably looks hotter than it would if it were viewed at a more equatorial angle (see H16). With  $K_{2\text{MASS}} = 12.62$ , and a *Gaia* DR2 distance of 637 pc, the system has  $M_K = 3.58$ . This is 0.4 mag more luminous than a K0V.

### 3.9. V508 Draconis (SDSS J171456.78+585128.3)

V508 Dra is a poorly studied long period CV. Agüeros et al. (2009) confirm the CV nature of the system, found a K4 spectral type for the donor, and believed the orbital period to be about 10 hours. Wils (2011) shows that the period is in fact 20.113 hr, and have published an ephemeris for the system. We downloaded the *WISE/NEOWISE* light curves and present them as Fig. 26. We have phased them using the ephemeris of Wils, but have shifted the time of phase 0 by  $\Delta\phi = -0.52$  to place the deeper of the two minima at  $\phi = 0.5$ , (i.e., inferior conjunction of the donor at  $\phi = 0.0$ ). Regardless of the nature of the donor, the large amplitude of these variations suggest a highly inclined system. If we assume a K4 spectral type,  $q = 0.8$ , and  $M_1 = 1.0 M_\odot$ , we find a best fitting inclination of  $i = 75^\circ$ . Changing the masses of the components in the system, or  $q$ , would change this inclination, but only by a few degrees. The scatter around the light curve model is minimal, so we expect very little contamination.

Using the  $q = 0.8$  model, the mass of the secondary is  $M_2 = 0.8 M_\odot$ , and WD2010

calculates its radius as  $1.64 R_{\odot}$ , and  $\log g = 3.9$ . Using these parameters we estimate a rotational velocity of  $95 \text{ km s}^{-1}$ . We will assume that the donor star is a subgiant. Our EQW analysis finds that for  $T_{\text{eff}} = 4500 \text{ K}$ , there are no abundance anomalies. There is, however, a significant carbon deficit, and the  $\chi^2$  analysis gives  $[\text{C}/\text{Fe}] = -0.3 \pm 0.02$ . The TripleSpec data are shown in Fig. 27, where a model with  $T_{\text{eff}} = 4500 \text{ K}$ ,  $\log g = 4.0$ ,  $[\text{Fe}/\text{H}] = 0.0$ , and  $[\text{C}/\text{Fe}] = -0.3$  is overplotted. The carbon deficit is necessary to match both the CO features in the  $K$ -band, as well as the depth of the broad CN feature in the  $J$ -band.

### 3.10. AH Herculis

AH Her is another long period ( $P_{\text{orb}} = 6.19 \text{ hr}$ ) Z Cam system. H16 found  $T_{\text{eff}_2} = 4500 \text{ K}$ ,  $[\text{Fe}/\text{H}] = -0.7$ , and  $[\text{C}/\text{Fe}] = -0.4$ . Our observations with TripleSpec on 2018 Feb 2 appear to have occurred during an outburst. Unfortunately, the AAVSO data base has sparse coverage, with the average of the two nearest points giving  $V = 11.8$ . At visual maximum, AH Her reaches  $V = 11$ . The conditions were non-photometric for our observing run, but by averaging the fluxes for AH Her and the telluric standard (HD 153808), we estimate  $K \sim 11.7$ . The 2MASS observations were obtained at the peak of an outburst of AH Her, and had  $K = 11.4$ . There were eight epochs of *WISE* and *NEOWISE* observations, none of them was centered on an outburst. Except for the *NEOWISE* observations on 2016 February 22, when AH Her was at minimum ( $V = 14.5$ ), all of these occurred at an intermediate brightness level, with  $12 \leq V \leq 13$ . This makes it difficult to estimate the contamination level for our spectra.

To construct the *WISE/NEOWISE* light curves, we took the mean values for each epoch, and offset them to match that found for the first *WISE* epoch. We plot the result in Fig. 28, where each epoch is color coded. We phase these data using the updated ephemeris in North et al. (2002). Three of the epochs of *NEOWISE* data have been excluded from

this plot, those for 2014 August 24, 2015 February 23, and 2016 August 10. The intrinsic scatter in those three data sets was twice that observed for the other epochs. Construction of the mean for when AH Her was in quiescence finds  $\langle W1 \rangle = 11.54$ , and  $\langle W2 \rangle = 11.48$ . For the first *WISE* epoch, we found  $\langle W1 \rangle = 11.17$ , and  $\langle W2 \rangle = 11.11$ . AH Her is about 0.4 mag brighter in the *WISE* bandpasses during standstill.

North et al. list the parameters for AH Her as  $M_1 = 0.95 M_\odot$ ,  $M_2 = 0.76 M_\odot$ ,  $i = 46^\circ$ , and a donor spectral type of K7V ( $T_{\text{eff}} = 4250$  K). Inputting these values into WD2010, we get the light curve model plotted as the solid line in Fig. 28. This does a reasonable job of fitting the lower bounds of the data, *assuming there is no contamination*. If we add a source that supplies 30% of the total flux, we need to increase the inclination to  $i = 70^\circ$  (dashed line) to achieve a similar result. Given that the change in the visual magnitude between quiescence and standstill is  $\Delta V = 2$ , while  $\Delta W1 = 0.4$ , we expect that the contamination level in our *JHK* spectra will be even higher, of order 40 – 50%.

The results of the EQW analysis for AH Her, like those for RX And and Z Cam, are not consistent with those of the synthetic spectra even with a 40 or 50% level of contamination. Again, some elements have strong excesses (sodium), while others have huge deficits (magnesium). We turn to the spectra, shown in Fig. 29, to attempt to better characterize the donor. We find that the spectrum of HD 42581 (M1.3V with  $[\text{Fe}/\text{H}] = 0.12$ ) with a 40% contamination level is a near-perfect match for the spectrum of AH Her. The only deviation is that the Al I doublet in the *J*-band spectrum of AH Her is much weaker than seen in the M1V. Perhaps, like SY Cancri, there is an emission line at this position that corrupts the depth of this feature. Though, there is no sign of an emission feature here. The Al I feature in the *K*-band appears to be relatively normal, as the He I emission line that normally corrupts this feature is weak in AH Her.

The other interesting aspect of the spectra can be seen in the *H*-band: there are weak

absorption lines from the H I Brackett series superposed on the late-type star spectrum. This is the first time we have seen “disk” H I absorption features in any of our near-IR spectra of CVs, showing that the system must have been in outburst at the time of our observations. We repeat the analysis that we used for Z Cam to check whether a donor with a spectral type of M1.3 can explain the observations of AH Her. In Fig. 30abc, we plot the EQW measures for the M dwarfs. Given the uncertainty in the donor spectral type, instead of plotting the measurements of AH Her as data points with error bars, we plot the EQW measures as a horizontal solid lines. We also plot what the EQWs should be if the contamination level was 40% as dashed lines.

It is clear that throughout the three bandpasses a 40% contamination level works well if the donor is an early M-type star. The main deviations are the Al I measure in the *J*-band and the Na I feature in the *H*-band. We noted the issue with the Al I line above. The reason the Na I doublet in the *H*-band is stronger than expected is that this feature is convolved with the absorption feature due to H I Br12. We conclude that the donor star in AH Her is an early M-type star with a solar abundance pattern. The hotter temperatures estimated for this source are due to contamination issues, as is the low value of [Fe/H] found in H16. AH Her does not have a carbon deficit. Modeling the light curve using a donor star temperature of 3600 K reduces the amplitude of the ellipsoidal variations by about 0.02 mag. It is a certainty that the orbital inclination angle is larger than  $46^\circ$ .

### 3.11. RU Pegasi

H16 and HM17 found for  $\log g = 4.5$  that the donor star in RU Peg had  $T_{\text{eff}} = 5125$  K,  $[\text{Fe}/\text{H}] = -0.28$ ,  $[\text{Mg}/\text{Fe}] = -0.20$ ,  $[\text{C}/\text{Fe}] = -0.2$ ,  $[\text{Na}/\text{Fe}] = 0.5$ , and  $^{12}\text{C}/^{13}\text{C} = 15$ . Given the long orbital period, it is likely that the donor star in RU Peg has a lower gravity than a main sequence star. For  $\log g = 4.0$ , HM17 found  $T_{\text{eff}} = 4750$  K,  $[\text{Fe}/\text{H}] = -0.2$ ,  $[\text{C}/\text{Fe}] =$

$-0.6$ ,  $[\text{Mg}/\text{Fe}] = -0.18$ ,  $[\text{Na}/\text{Fe}] = +0.3$ , and  $^{12}\text{C}/^{13}\text{C} = 6$ . We will consider both gravities, and assume the derived values for the carbon abundance in our analysis.

For the  $\log g = 4.5$  (“dwarf”) models, a metallicity of  $[\text{Fe}/\text{H}] = -0.3$  fits best in each of the wavebands. In the  $K$ -band, there is a small deficit of magnesium, and apparent enhancements of aluminum and sodium. The aluminum abundance is normal in the  $H$ -band for the subsolar metallicity. The same result attains in the  $J$ -band, where silicon appears to have a normal abundance at  $[\text{Fe}/\text{H}] = -0.3$ , compared to the fit seen in the  $K$ -band. There is no evidence for a sodium enhancement in the  $J$ -band. A slightly better fit results when using hotter donor,  $T_{\text{eff}} \geq 5000$  K, in agreement with the results of HM17.

For the  $\log g = 4.0$  models, a temperature of  $T_{\text{eff}} = 4750$  K works poorly at any metallicity. For the  $K$ -band, a model with  $T_{\text{eff}} = 5000$  K and  $[\text{Fe}/\text{H}] = -0.3$  provides a reasonable fit to Mg I, Ca I, and Fe I. It appears that both sodium and aluminum are enhanced, but the magnesium abundance is normal within the error bars of the measurement. Silicon appears to have a deficit. In the  $H$ -band, magnesium appears to be enhanced, and aluminum normal. In the  $J$ -band, there are no statistically significant deviations from a solar abundance pattern at a subsolar metallicity. The largest offsets imply a small enhancement of sodium, and a small deficit of silicon.

These results for RU Peg are similar to those derived in HM17. The difference, however, is that here we find that a subgiant model fits the measured equivalent widths better than a dwarf model. In the subgiant scenario, the deficit of magnesium is much smaller than found in the dwarf model. Other than carbon, the only deviations from a solar abundance pattern for the subgiant model are the enhanced levels of sodium, a possible underabundance of silicon and, of course, the low value of the  $^{12}\text{C}/^{13}\text{C}$  ratio derived in HM17. It is interesting to note that Godon et al. (2008) found that silicon and carbon were underabundant from their modeling of the UV spectra of RU Peg.

The subsolar abundance of RU Peg, like that for SS Cyg, argues for contamination. In Fig. 31 we present the *JHK* plus *WISE* light curves of RU Peg. Dunford et al. (2012) have provided an updated ephemeris for RU Peg, and solved for the system parameters:  $M_1 = 1.06 M_\odot$ ,  $M_2 = 0.96 M_\odot$ , and  $i = 43^\circ$ . The *JHK* light curves are not clean ellipsoidal variations, and confirm that there is a contaminating, non-stellar, highly variable source in the system. The smaller depth of the  $\phi = 0.5$  minimum argues for a heavily irradiated hemisphere. Assuming  $T_{\text{eff}_2} = 5000$  K, we find that the white dwarf in the model has to have  $T_{\text{eff}_1} = 45,000$  K to get the ratio of the minima to match observations. The *JHK* observations were obtained about a week after RU Peg had returned to minimum light following an eruption. This might partially account for the high temperature of the white dwarf we find here, however, Sion & Urban (2002) used UV observations to find a quiescent white dwarf temperature of  $T_{\text{eff}} = 50,000 - 53,000$  K.

Without a contaminating source, we find that the best fit orbital inclination is  $40^\circ$ , consistent with the value from Dunford et al. A third light component that supplies 25% of the flux at inferior conjunction requires  $i = 50^\circ$ , while reproducing the lower envelope of the light curves in all five bands. The 5 to 10% random variations seen in *JHK* give way to 20% variations in *W1* and *W2*. The total amplitude of the variations in the *W3* band (not plotted) is even larger:  $\Delta W3 = 0.9$  mag.

The *JHK* spectra were obtained near inferior conjunction,  $\phi = 0.85$ , about two weeks after RU Peg had returned to minimum light. While a contamination level of 25% is probably reasonable in the *K*-band, it appears that the contamination in *J* and *H* might be even higher. Assuming that the donor supplies 75% of the flux in each of the bandpasses, we find that the best fitting model at both gravities has  $[\text{Fe}/\text{H}] = 0.0$ . At this metallicity, the subgiant model fits the data slightly better than the dwarf model. If, however, the contamination level is increased to 35%, the dwarf model would fit equally well. A higher

temperature donor,  $T_{\text{eff}_2} = 5250$  K (at 25% contamination), also results in a better fit for the dwarf model. In all scenarios, the only significant abundance anomaly is the large excess of sodium. Magnesium has a small deficit in the dwarf model.

Given the large mass for the donor found by Dunford et al., its surface gravity is  $\log g = 4.4$ , a value consistent with that of a main sequence dwarf. That mass, however, is not consistent with the temperature we have derived, being more appropriate for an early G-type dwarf, than an early K-type dwarf. If one uses an inclination of  $50^\circ$  instead of  $43^\circ$ , with  $q = 0.88$ , the masses of both components in the system are lower:  $M_1 = 0.76 M_\odot$ , and  $M_2 = 0.67 M_\odot$ . The resulting secondary star mass would be much more consistent with the effective temperature found above. The *Gaia* DR2 parallax is in agreement with the *HST* parallax (Harrison et al. 2004b) and, as noted in H16, RU Peg is 1.2 mag more luminous than a main sequence star of its observed spectral type.

### 3.12. GK Persei

For the long-period, old classical nova GK Per, H16 found (for  $\log g = 4.0$ ):  $T_{\text{eff}} = 5000$  K,  $[\text{Fe}/\text{H}] = -0.3$ ,  $[\text{Mg}/\text{Fe}] = -0.3$ , and  $[\text{C}/\text{Fe}] = -0.5$ . We generated our synthetic spectral grid using a value of  $v \sin i = 55 \text{ km s}^{-1}$  from Harrison & Hamilton (2015), and with  $[\text{C}/\text{Fe}] = -0.5$ . We assume that the subgiant donor star dominates the near-IR spectral energy distribution (see Fig. 16 in Harrison et al. 2013b). Our equivalent width analysis finds an identical result to that of H16. There are no significant abundance anomalies except that of magnesium, and no evidence for a hydrogen deficit. Silicon and potassium appear to be slightly underabundant, but the spectra for GK Per have lower S/N than most of the other targets modeled here.

### 3.13. QZ Serpentis

The oddest object in the survey of H16 was QZ Ser. It has an orbital period near two hours, yet the donor has a spectral type near K5. H16 generated spectra where they altered the hydrogen abundance, and concluded that a hydrogen deficiency was the best explanation for its unusual spectrum. They found that sodium was highly overabundant ( $[\text{Na}/\text{Fe}] = +1.5$ ), and aluminum also had a greatly enhanced abundance ( $[\text{Al}/\text{Fe}] = +0.5$ ). Carbon was nearly undetectable,  $[\text{C}/\text{Fe}] = -1.7$ . No other abundance anomalies were obvious in their analysis. In the following we will assume that the donor star has a temperature of 4500 K, and that there is no contamination from other sources in the system (see Thorstensen et al. 2002).

To derive an estimate of  $v \sin i$  for QZ Ser, we velocity broadened a synthetic spectrum ( $T_{\text{eff}} = 4500$  K,  $[\text{Fe}/\text{H}] = 0.0$ ,  $\text{Hd} = 90\%$ ) until we achieved a good match between the lines across the three bandpasses. Rotation velocities near  $v \sin i = 150$  km s $^{-1}$  worked reasonably well, given the unusual abundance pattern. A grid was generated with this rotation velocity, and  $[\text{C}/\text{Fe}] = -1.7$ , with our EQW programs applied to the resulting data set. The values for the EQWs for QZ Ser across the three bandpasses plotted against the synthetic grid is presented as Fig. 32abc. The enormous sodium overabundance is obvious in each of the three bandpasses. In the  $J$  and  $K$  bandpasses, the Na I doublet is about twice as deep as the  $\text{Hd} = 90\%$  model. In the  $H$ -band, the sodium doublet is about three times stronger than the 90% model. This difference was noted in H16.

The measurement of EQWs in QZ Ser is hampered by the presence of a large number of absorption features caused by the peculiar nature of the donor. If we use the higher atomic mass elements, K, Ca, Fe, and Mn, the best fit occurs for  $\text{Hd} = 90\%$ . Assuming this is correct, it appears that magnesium is deficient. Though the EQW of the Mg I line in the  $K$ -band is consistent with  $\text{Hd} = 90\%$ , the continuum region from 22500 to 22850 Å,

where the Mg I line is located, appears to be depressed compared to nearby segments of the spectrum. It is likely that other absorption features are complicating the extraction of the true value of the EQW for the Mg I line in the  $K$ -band.

H16 found an enhanced aluminum abundance, and the results in the  $J$  and  $H$ -bands are consistent with this conclusion. In the  $K$ -band, the combination of He I emission, and another segment of depressed continuum, makes the EQW measurement of the Al I feature unreliable. We cannot determine the silicon abundance using our EQW programs, as two of the four lines in the  $J$ -band are corrupted by what appear to be emission features, and one of the other lines is convolved with a nearby absorption feature. This is also true for the Si I feature in the  $K$ -band. As can be seen in Fig. 28 of H16, there are several strong absorption features in the  $K$ -band between 21200 and 22000 Å. The reddest of these, centered near  $\lambda 21900$  Å appears to be a convolution of absorption from Ti I at 21789 Å, and Si I at 21903 Å. Using IRAF, measurement of this line gives a value of 8.3 Å for the equivalent width. For the synthetic spectrum (with  $H_d = 90\%$ ), we find  $EQW = 1.1$  Å. If the silicon abundance was this strongly enhanced, we would be able to see it in the Si I line at  $\lambda 12264$  Å, the only clearly visible Si I line in the  $J$ -band. There is a Si I absorption line in the  $H$ -band at  $\lambda 15888$  Å, and for QZ Ser we measure  $EQW = 6.8$  Å. For the synthetic spectrum, we find  $EQW = 6.5$  Å. Silicon appears to have a normal abundance.

Another one of the strong absorption lines in the region near H I Br $\gamma$  in the  $K$ -band is the feature at  $\lambda 21789$  Å. There is a Ti I line at this position. We measure  $EQW = 4.5$  Å in QZ Ser, and  $EQW = 1.2$  in the synthetic spectrum. There are two other strong lines to the blue of previous feature, one at  $\lambda 21450$  Å, and the other at  $\lambda 21618$  Å. Using the NIST Spectral Database<sup>6</sup>, there are absorption lines from both Na I and Ti I at  $\lambda 21450$  Å, and a Ti I line at  $\lambda 21604$  Å. The bluer of these two lines has  $EQW = 5.4$  Å, compared to  $EQW =$

---

<sup>6</sup>[https://physics.nist.gov/PhysRefData/ASD/lines\\_form.html](https://physics.nist.gov/PhysRefData/ASD/lines_form.html)

1.17 in the synthetic data. There does not seem to be a counterpart in the model spectrum for the redder line. Unless there are absorption lines of other elements contaminating these various features, it appears that titanium has an enhanced abundance.

Our analysis for the spectrum of QZ Ser confirms the results from H16: it appears that the donor star in this system suffers an extreme hydrogen deficit ( $\geq 90\%$ ), larger than any of the other program objects. The enormous overabundance of sodium, enhanced aluminum, and the deficit of magnesium found by H16 are confirmed. In addition, there appears to be a large enhancement of titanium,  $[\text{Ti}/\text{Fe}] \sim +0.5$ .

#### 4. Discussion

We have used ATLAS12 to generate hydrogen-deficient stellar atmospheres for K dwarfs to enable us to generate synthetic spectra to determine if the donor stars of any long period cataclysmic variables have evidence for photospheric hydrogen deficiencies. It is clear that several systems show strong evidence for such anomalies: AE Aqr, DX And, EY Cyg, and QZ Ser. For the first three of these, the hydrogen deficits are in the 25 to 50% range, while QZ Ser appears to have a hydrogen deficit of 90%. Unfortunately, we cannot rigorously quantify the hydrogen deficits due to spectral type uncertainty, the limited number of uncontaminated spectral features, intrinsic abundance variations, contamination issues, the presence of emission lines of H and He, insufficient S/N in the data, and the vagaries of the near-infrared spectral reduction process. Fortunately, all four systems with identified hydrogen deficits appear to have low levels of contamination, and have donors with well-determined spectral types. We summarize our results for the program objects in Table 4.

We had previously shown that AE Aqr was unusual in that its carbon deficit was

very large,  $[C/Fe] \leq -1.4$ . It has also been proposed that AE Aqr is a relatively young CV (Schenker et al. 2002), having only recently exited the “post-thermal-time-scale mass transfer state.” They predicted that it might have a small  $^{12}C/^{13}C$  ratio, which appears to have been confirmed by HM17. Echevarría et al. (2007) concluded that the donor star in EY Cyg was 30% larger than a main sequence star of the same spectral type, suggesting it is evolved. A similar conclusion was reached by Drew et al. (1993) for DX And. Thus, it is not too surprising that these three systems might show evidence for hydrogen deficits. As described in H16, Thorstensen et al. (2002) had already suggested that the donor in QZ Ser might be hydrogen deficient. It certainly remains the poster child for such systems. There appeared to be several short period CVs in the survey of H16 that had similar properties to QZ Ser, but which had M-type secondaries.

It is worthwhile to examine the outburst intervals for the hydrogen deficient dwarf novae (AE Aqr is not in this category). Using the AAVSO data base, we find that in the past five years DX And, EY Cyg and QZ Ser have had very few dwarf novae outbursts. For DX And there have been three observed eruptions, two for QZ Ser (one of which appears to have been a “superoutburst”), and only one for EY Cyg. While RU Peg, a solar abundance pattern system with a similar orbital period to DX And and EY Cyg, has had 21 eruptions! Many CVs with orbital periods like that of QZ Ser are SU UMa systems that exhibit frequent dwarf novae outbursts, and more infrequent superoutbursts. Other CV systems with similar orbital periods, however, can also have infrequent outbursts (see Kato et al. 2003). Establishment of any tendencies will require a larger survey, but starting by selecting infrequently outbursting dwarf novae for study might prove fruitful for finding additional hydrogen deficient objects.

As in H16, we find that carbon and magnesium deficits are the most common abundance anomalies, whether or not the system has a hydrogen deficit. Aside from

sodium, there are few other elements in the program objects that have odd abundances. RU Peg may have a small deficit of silicon. In QZ Ser, both aluminum and titanium appear to have enhanced abundances. One of the most surprising results from our survey is that the three long period Z Cam systems (Z Cam, SY Cnc, and AH Her) have solar metallicities and abundance patterns. The origin of the Z Cam phenomenon does not appear to be related to *unusual* abundance issues. It is interesting that RX And appears to exhibit some Z Cam-like behavior, and its donor has a solar metallicity. However, the donor in RX And also has deficits of both magnesium and carbon, unlike the three Z Cam systems studied here.

The consideration of the contamination of the infrared spectra by non-stellar sources has led to the dramatic revision in the metallicities for both SS Cyg and RU Peg. Both systems appear to have  $[\text{Fe}/\text{H}] = 0.0$ , though the abundance anomalies identified in H16 and HM17 for these two objects remain. It is likely that many of the objects identified as having low metallicity in that survey actually have spectra that suffer from significant contamination issues. The combination of EQW measures, light curve modeling of the *WISE/NEOWISE* data, and matching of (contaminated) synthetic/template spectra to the observed *JHK* spectra, appears to allow for excellent estimates of the contamination level. Obviously, it would be better to have quiescent *JHK* light curves of every source for light curve modeling, but given that such data do not exist, the *WISE/NEOWISE* photometry provides a useful alternative. As demonstrated above, those data were sufficient to determine/revise the orbital inclinations for SY Cnc, V508 Dra, AH Her, and RU Peg.

Our new methods allow us to examine the reliability of the spectral type determinations listed in H16, and elsewhere. For the majority of the systems, the  $\chi^2$  techniques used in H16 produced reliable spectral types. We confirm their assignment of an M-type donor in RX And. The only significantly different spectral type reassignment is that for AH Her.

Not surprising given that H16 only had a  $K$ -band spectrum to work with. The same cannot be said for most of the spectral types assigned using optical data. Only in those systems where the contamination in the visual is insufficient to mask the donor star (e.g., AE Aqr, DX And or SS Cyg), and/or where line ratio analysis was performed, are optically-derived spectral types accurate. Perhaps the most surprising result in this vein is the late spectral type we find for the donor in Z Cam. This system has an orbital period close to seven hours. The mass of the donor,  $M_2 = 0.77 M_\odot$ , is similar to that of a main sequence K0V. Perhaps, like the results in H16 for U Gem, it is the large inclination angle that makes the system appear to have a such a cool temperature.

The success of using the equivalent widths of field M dwarfs in ascertaining the nature of the donors in RX And, Z Cam and AH Her suggests that we can use this technique to validate our analysis regimen. In Fig. 33abc, we plot the EQW measurements for all of the K and M dwarfs discussed above. The x-axis in this plot now extends to  $-8$ , which is the coding for a K0V. We plot the values of the EQW measures for SS Cyg as a horizontal solid line in each plot. We also plot what the equivalent widths would be if the contamination was 25% (dashed lines), and 50% (dotted lines). Our results for SS Cyg put its spectral type at  $-4.5$ . It is obvious that a 25% contamination is the best fit to the majority of the EQW measures near this spectral type. The only significant deviation is the large magnesium deficit. This confirms the results derived above, and lends confidence to the entire process. If the metallicity of the CV donor is not too extreme, this technique provides a useful estimate of the contamination level if the spectral type is approximately known, or the spectral type if the contamination level can be estimated, without recourse to synthetic or template spectra matching.

Thus, we can now state with confidence that magnesium and carbon deficiencies are common among the donor stars in CVs. There are also systems with enhanced levels of

sodium. H16 discussed the possible mechanisms to produce such systems. It is clear that long period CVs have a very wide range of properties, from systems with completely normal abundance patterns, to highly peculiar ones. It is interesting that the two longest period systems, GK Per and V508 Dra, have subgiant donor stars that are relatively normal, with the only shared anomaly being a carbon deficit. While there are systems with orbital periods near 10 hrs that have significant hydrogen deficits. As explored in Kalomeni et al. (2016), there have to be a variety of paths for producing CVs.

## 5. Conclusions

Using new hydrogen deficient atmospheres, we have generated synthetic spectra to determine whether any CV donor stars show evidence for hydrogen deficiencies. We have found four systems that appear to have such deficits. We have also shown that when a contamination estimate is possible, one can use the EQW method to obtain both donor star temperatures and identify abundance anomalies without the need for model spectra. This includes application to M-type donor stars, where it currently remains extremely difficult to construct realistic synthetic spectra. Further refinement of the M star equivalent width technique used above, which would include obtaining additional spectra of M-type stars spanning a wider range in properties, is needed to enable its use for deriving accurate values for donor star temperatures, metallicities, abundance anomalies, and contamination levels. The latter grows in importance in shorter period CV systems where the donor stars are much less luminous relative to the white dwarf and its accretion disk.

T. E. H. was partially supported by a grant from the NSF (AST-1209451). The Gemini GNIRS data were acquired under the program GN-2017A-Q-91. This publication makes use of data products from the Wide-field Infrared Survey Explorer, which was

a joint project of the University of California, Los Angeles, and the Jet Propulsion Laboratory/California Institute of Technology, funded by the National Aeronautics and Space Administration. This publication makes use of data products from the Near-Earth Object Wide-field Infrared Survey Explorer (NEOWISE), which is a project of the Jet Propulsion Laboratory/California Institute of Technology. NEOWISE is funded by the National Aeronautics and Space Administration. We acknowledge with thanks the variable star observations from the AAVSO International Database contributed by observers worldwide and used in this research. This publication makes use of data products from the 2MASS, which is a joint project of the University of Massachusetts and the Infrared Processing and Analysis Center/California Institute of Technology, funded by the National Aeronautics and Space Administration and the National Science Foundation.

## References

- Abada-Simon, M., Casares, J., Evans, A., Eyres, S., Fender, R., et al. 2005, *A&A*, 433, 1063
- Agüeros, M. A., Anderson, S. F., Covey, K. R., Hawley, S. L., Margon, B., et al. 2009, *ApJS*, 181, 444
- Beuermann, K., Baraffe, I., Kolb, U., & Weichhold, M. 1998, *A&A*, 339, 518
- Bitner, M. A., Robinson, E. L., & Behr, B. B. 2007, *ApJ*, 662, 564
- Bonnet-Bidaud, J. M., & Mouchet, M. 1987, *A&A*, 188, 89
- Boyajian, T. S., von Braun, K., van Belle, G., McAlister, H. A., ten Brummelaar, T. A., et al. 2012, *ApJ*, 757, 112
- Bruch, A., Vrielmann, S., Hessman, F. V., Kocksiek, A., & Schimpke, T. 1997, *A&A*, 327, 1107
- Casares, J., Martínez-Pais, I. G., & Rodríguez-Gil, P. 2009, *MNRAS*, 399, 1534
- Castelli, F. 2005, *MSAIS*, 8, 25
- Covey, K. R., Lada, C. J., Roman-Zuniga, C. et al. 2010, *ApJ*, 722, 971
- Cushing, M. C., Rayner, J. T., & Vacca, W. D. 2005, *ApJ*, 623, 1115
- Drew, J. E., Jones, D. H. P., & Woods, J. A. 1993, *MNRAS*, 260, 803
- Dubus, G., Campbell, R., Kern, B., Taam, R. E., & Spruit, H. C. 2004, *MNRAS*, 349, 869
- Dunford, A., Watson, C. A., Smith, R. C. 2012, *MNRAS*, 422, 3444
- Echevarría, J., Connon Smith, R., Costero, R., Zharikov, S., & Michel, R. 2007, *A&A*, 462, 1068
- Friend, M. T., Martin, J. S., Connon Smith, R., & Jones, D. H. P. 1990b, *MNRAS*, 246, 654
- Friend, M. T., Martin, J. S., Connon Smith, R., & Jones, D. H. P. 1990a, *MNRAS*, 246, 637
- Gaia Collaboration: Brown, A. G. A., Vallenari, A., Prusti, T., de Bruijne, J. H. J., Babusiaux, C., et al. 2018, arXiv: 1804.09365
- Gänsicke, B. T., Szkody, P., de Martino, D., Beuermann, K., Long, K. S., et al. 2003, *ApJ*,

594, 443

Godon, P., Sion, E. M., Barrett, P. E., Hubeny, I., Linnell, A. P., & Szkody, P. 2008, *ApJ*, 679, 1447

Goliasch, J., & Nelson, L. 2015, *ApJ*, 809, 80

Harrison, T. E., & Marra, R. E. 2017 (HM17), *ApJ*, 843, 152

Harrison, T. E. 2016 (H16), *ApJ*, 833, 14

Harrison, T. E., & Hamilton, R. T. 2015, *AJ*, 150, 142

Harrison, T. E., Hamilton, R. T., Tappert, C., Hoffman, D. I., & Campbell, R. K. 2013a, *ApJ*, 145, 19

Harrison, T. E., Campbell, R. D., & Lyke, J. E. 2013b, *ApJ*, 146, 37

Harrison, T. E., Bornak, J., Howell, S. B., Mason, E., Szkody, P., & McGurk, R. 2009, *AJ*, 137, 4061

Harrison, T. E., Howell, S. B., Szkody, P., & Cordova, F. A. 2007, *ApJ*, 133, 162

Harrison, T. E., Osborne, H. L., & Howell, S. B., 2005, *AJ*, 129, 2400

Harrison, T. E., Osborne, H. L., & Howell, S. B., 2004a, *AJ*, 127, 3493

Harrison, T. E., Johnson, J. J., McArthur, B. E., Benedict, G. F., Szkody, P., et al. 2004b, *AJ*, 127, 460

Hartley, L. E., Long, K. S., Froning, C. S., & Drew, J. E. 2005, *ApJ*, 623, 425

Henry, T. J., & McCarthy, D. W. 1993, *AJ*, 106, 773

Hill, C. A., Watson, C. A., Shahbaz, T., Steeghs, D., & Dhillon, V. S. 2014, *MNRAS*, 444, 192

Howell, S. B., Nelson, L. A., & Rappaport, S. 2001, *ApJ*, 550, 897

Houk, N., Swift, C. M., Murray, C. A., Penston, M. J., & Binney, J. J. 1997, in *Proc. ESA Symp. Hipparcos Venice*, ESA SP-402, ed. M. A. C. Perryman & P. L. Bernacca (Noordwijk: ESA), 279

Kaitchuck, R. R. 1989, *PASP* 101, 1129

- Kalomeni, B., Nelson, L., Rappaport, S., et al. 2016, *ApJ*, 833, 83
- Kato, T., Nogamin, D., Moilanen, M., & Yamaoka, H. 2003, *PASJ*, 55, 989
- King, A. R., & Kolb, U. 1995, *ApJ*, 439, 330
- Knigge, C., Baraffe, I., & Patterson, J. 2011, *ApJS*, 194, 28
- Körding, E., Rupen, M., Knigge, C., et al. 2008, *Sci*, 320, 1318
- Kraft, R. P., Krzeminiski, W., Mumford, G. S. 1969, *ApJ*, 158, 589
- Kraft, R. P. 1962, *ApJ*, 135, 408
- Kurucz, R. L. 2005, *MSAIS*, 8, 14
- Lindgren, L., Hernandez, J., Bombrun, A., Klioner, S., Bastian, U., et al. 2018, *arXiv* 1804.09366
- Mainzer, A., Bauer, J., Grav, T., Masiero, J., Cutri, R. M., et al. 2011, *ApJ*, 731, 53
- Mauche, C. W., Lee, Y. P., & Kallman, T. R. 1997, *ApJ*, 477, 832
- Neustroev, V. V., & Zharikov, S. 2008, *MNRAS*, 386, 1366
- North, R. C., Marsh, T. R., Moran, C. K. J., Kolb, U., Smith, R. C., & Stehle, R. 2000, *MNRAS*, 313, 383
- North, R. C., Marsh, T. R., Kolb, U., Dhillon, V. S., & Moran, C. K. J. 2002, *MNRAS*, 337, 1215
- Pecaut, M. J., & Mamajek, E. E. 2013, *ApJS*, 208, 9
- Podsiadlowski, Ph., Han, Z., & Rappaport, S. 2003, *MNRAS*, 340, 1214
- Politano, M., & Weiler, K. P. 2007, *ApJ*, 655, 663
- Ritter, H. 2012, *MmSAI*, 83, 505
- Ritter H., & Kolb U. 2003, *A&A*, 404, 301
- Rodriguez-Gil. P., Torres, M. A. P., Gansicke, B. T., Munoz-Darius, T., Steeghs, D., Schwarz, R., Rau, A., Hagen, H. J. 2009, *MNRAS*, 395, 973
- Salaris, M., Serenelli, A., Weiss, A., & Bertolami, M. M. 2009, *ApJ*, 692, 1013
- Schreiber, M. R., Gänsicke, B. T., & Mattei, J. A., 2002, *A&A*, 384, 6

- Sepinsky, J. F., Sion, E. M., Szkody, P., & Gänsicke, B. T. 2002, *ApJ*, 574, 937
- Shafter, A. W. 1983, PhD thesis, University of California, Los Angeles
- Shenker, K., King, A. R., Kolb, U., Wynn, G. A., & Zhang, Z. 2002, *MNRAS*, 337, 1105
- Simonsen, M., Boyd, D., Goff, W., Krajci, T., Menzies, K., et al. 2017, *JAAVSO*, 42, 177
- Sion, E. M., Winter, L., Urban, J. A., Tovmassian, G. H., Zharikov, S. et al. 2004, *AJ*, 128, 1795
- Sion, E. M., & Urban, J. A. 2002, *ApJ*, 572, 456
- Soubiran, C., Le Campion, J. -F., Brouillet, N., & Chemin, L. 2016, *A&A*, 591, 118
- Szkody, P., & Silber, A. 1996, *AJ*, 112, 289
- Tanzi, E. G., Chincarini, G., & Tarengi, M. 1981, *PASP*, 93, 68
- Thorstensen, J. R., Fenton, W. H., Patterson, J., et al. 2002, *PASP*, 114, 1117
- Thorstensen, J. R., & Ringwald, F. A. 1995, *IBVS*, 4249
- Urban, J. A., & Sion, E. M. 2006, *ApJ*, 642, 1029
- Vollmann, K., & Eversberg, T. 2006, *AN*, 327, 862
- Wade, R. A. 1980, PhD thesis, California Institute of Technology
- Warner, B. 1995, in “Cataclysmic Variable Stars”, (Cambridge University Press:Cambridge), p495
- Welsh, W. F., Horne, K., & Gomer, R. 1995, *MNRAS*, 275, 649
- Williams, R. E., & Ferguson, D. H. 1982, *ApJ*, 257, 672
- Wils, P. 2011, *JAAVSO*, 39, 60
- Wright, E. L., Eisenhardt, P. R. M., Mainzer, A. K., et al. 2010, *AJ*, 140, 1868

Table 1. Observation Log

Object	Date Observed (UT)	Number Exps. $\times$ Exp. Time	Orbital Phase (mean)	Instrument
DX And	2017 07 10	$10 \times 340$ s	0.00	GNIRS
Z Cam	2018 02 02	$8 \times 300$ s	0.27	TSPEC
SY Cnc	2018 02 02	$4 \times 300$ s	0.68	TSPEC
EM Cyg	2017 06 02	$10 \times 300$ s	0.28	GNIRS
V508 Dra	2017 07 18	$12 \times 240$ s	0.17	TSPEC
AH Her	2018 02 02	$8 \times 300$ s	0.57	TSPEC

Table 2. Equivalent Width Measurement Bandpasses

Element	Blue Continuum Bandpass (Å)	Line Bandpass (Å)	Red Continuum Bandpass (Å)
Na I	11250 — 11360	11372 — 11418	11450 — 11570
Si I	11450 — 11570	11585 — 11630	11709 — 11732
K I	11450 — 11570	11682 — 11709	11709 — 11732
Mg I	11785 — 11814	11822 — 11853	11853 — 11868
Fe I	11853 — 11868	11875 — 11908	11908 — 11940
Si I	11905 — 11940	12090 — 12115	12135 — 12235
Si I	12135 — 12235	12265 — 12289	12290 — 12365
K I	12450 — 12495	12515 — 12545	12580 — 12655
Ni I	12907 — 12923	12933 — 12955	12955 — 12958
Mn I	12955 — 12958	12970 — 12995	12995 — 13016
Si I	12995 — 13016	13028 — 13055	13055 — 13105
Al I	13055 — 13105	13119 — 13174	13174 — 13255
Mn I	13174 — 13255	13275 — 13342	13342 — 13365
Mg I	14730 — 14840	14850 — 14900	14910 — 14994
Mg I	14910 — 14994	15000 — 15070	15100 — 15187
Fe I	15267 — 15280	15283 — 15302	15340 — 15365
Na I	16245 — 16295	16369 — 16410	16460 — 16630
Al I	16560 — 16645	16732 — 16765	16885 — 16990
Mg I	17030 — 17080	17081 — 17140	17150 — 17290
Al I	20990 — 21034	21079 — 21185	21280 — 21330

Table 2—Continued

Element	Blue Continuum Bandpass (Å)	Line Bandpass (Å)	Red Continuum Bandpass (Å)
Si I	21280 — 21330	21335 — 21370	21380 — 21415
Na I	21940 — 21990	22030 — 22119	22190 — 22245
Fe I	22190 — 22245	22360 — 22405	22550 — 22590
Ca I	22550 — 22590	22591 — 22685	22690 — 22780
Mg I	22690 — 22780	22781 — 22840	22842 — 22900

Table 3. Spectral Type Template Parameters

Name	Spectral Type	$\langle T_{\text{eff}} \rangle$ (K)	$\langle [\text{Fe}/\text{H}] \rangle$
HD145675	K0V	$5320 \pm 114$	$+0.41 \pm 0.12$
HD10476	K1V	$5189 \pm 53$	$-0.06 \pm 0.06$
HD3765	K2V	$5023 \pm 66$	$+0.05 \pm 0.10$
HD219134	K3V	$4837 \pm 138$	$+0.05 \pm 0.10$
HD45977	K4V	$4689 \pm 174$	$+0.03 \pm 0.18$
HD36003	K5V	$4615 \pm 29$	$-0.14 \pm 0.08$
61 Cyg A	K5V	$4394 \pm 150$	$-0.18 \pm 0.15$
HD237903	K7V	$4110 \pm 102$	$-0.21 \pm 0.10$

Table 4. Results for the Program CVs

Name	$T_{\text{eff}}$ (K)	$\log g$	[Fe/H]	Hydrogen Deficit	Abundance Notes
DX And	5000	4.5	0.0	25%	$[\text{C}/\text{Fe}] = -0.5$ , $[\text{Mg}/\text{Fe}] = -0.3$ , $[\text{Na}/\text{Fe}] = +0.3$
DX And	5000	4.0	0.0	25%	$[\text{C}/\text{Fe}] = -0.7$ , $[\text{Mg}/\text{Fe}] = -0.2$ , $[\text{Na}/\text{Fe}] = +0.5$
RX And	3500	4.5	+0.07	0%	$[\text{C}/\text{Fe}] \leq -0.3$ , $[\text{Mg}/\text{Fe}] \leq -0.2$
AE Aqr	5000	4.5	0.0	25%	see HM17
AE Aqr	5000	4.0	0.0	25%	see HM17
Z Cam	3575	4.5	+0.03	0%	solar
SY Cnc	5250	4.5	0.0	0%	solar
SS Cyg	4750	4.5	0.0	0%	HM17, except $[\text{Na}/\text{Fe}] = +0.2$
EM Cyg	4500	4.5	0.0	0%	$[\text{C}/\text{Fe}] \leq -0.5$ , $[\text{Mg}/\text{Fe}] \leq -0.5$
EY Cyg	5250	4.5	0.0	25%	see H16
EY Cyg	5250	4.0	0.0	50%	see H16
V508 Dra	4500	4.0	0.0	0 %	$[\text{C}/\text{Fe}] = -0.3$
AH Her	3600	4.5	0.12	0%	solar
RU Peg	5000	4.5	0.0	0%	see HM17
RU Peg	5000	4.0	0.0	0%	see HM17
GK Per	5000	4.0	-0.3	0%	see H16
QZ Ser	4500	4.5	0.0	90%	H16, except $[\text{Ti}/\text{Fe}] = +0.5?$



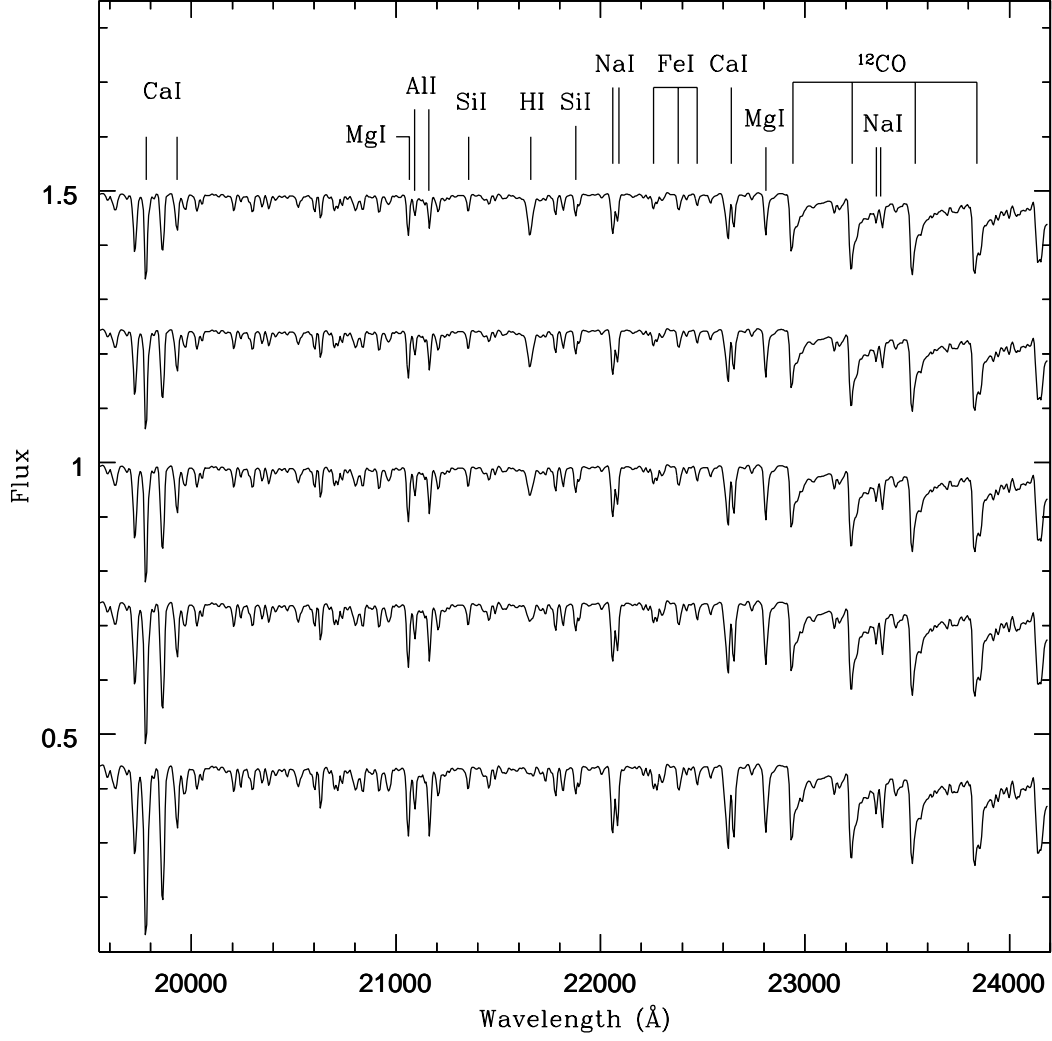


Fig. 1.— Synthetic *K*-band spectra for  $T_{\text{eff}} = 5000$  K and  $[\text{Fe}/\text{H}] = 0.0$ , with five different values for the hydrogen deficit. The model at top has  $\text{Hd} = 0\%$ , while that at the bottom has  $\text{Hd} = 90\%$ . The metal lines (the strongest of which are identified at the top of the plot) all get stronger as hydrogen becomes depleted, while the H I Br $\gamma$  line at 21600 Å slowly disappears.

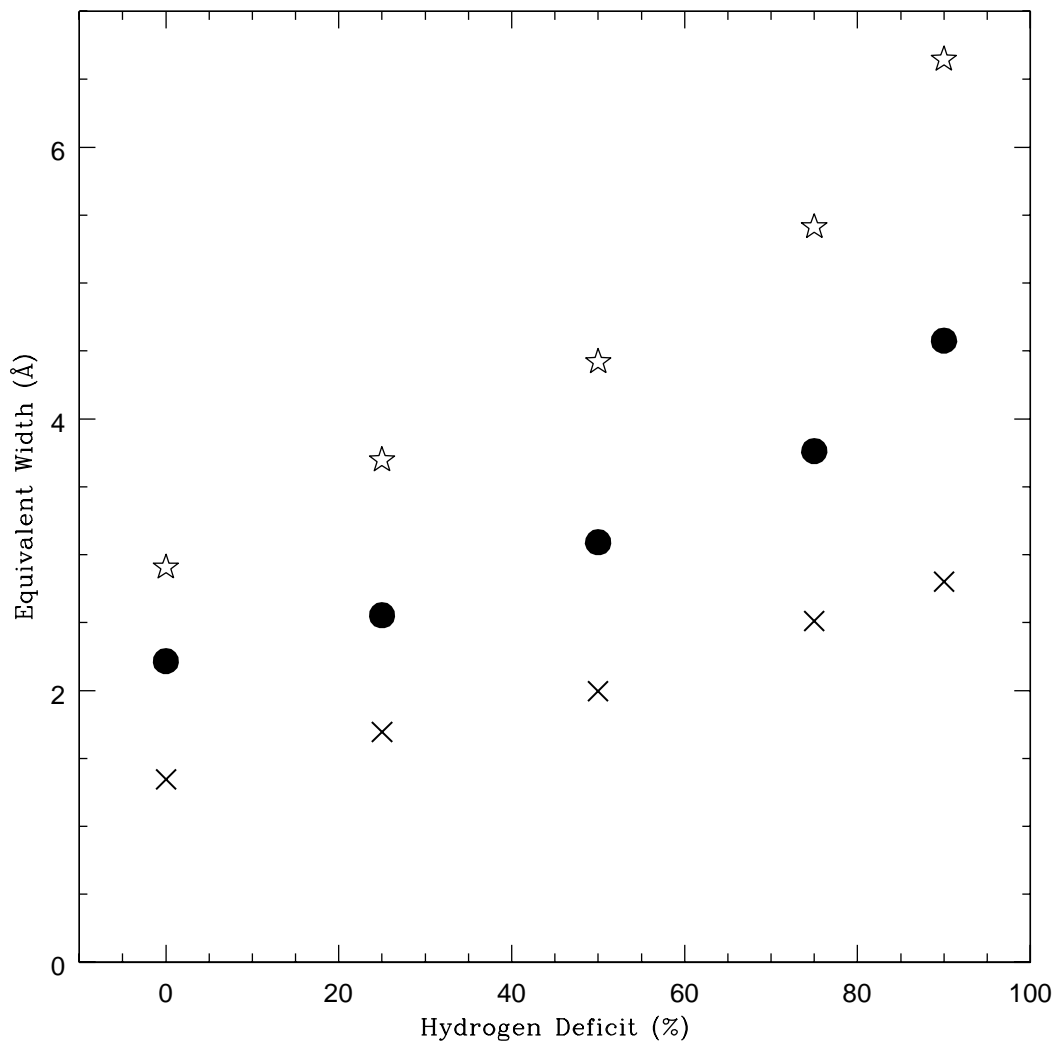


Fig. 2.— Equivalent width measurements from the synthetic  $K$ -band spectra presented in Fig. 1. The star-shaped symbols are for the Na I doublet at 22000 Å, the filled circles are for the Ca I triplet at 22632 Å, and the crosses are for the Mg I feature 22808 Å.

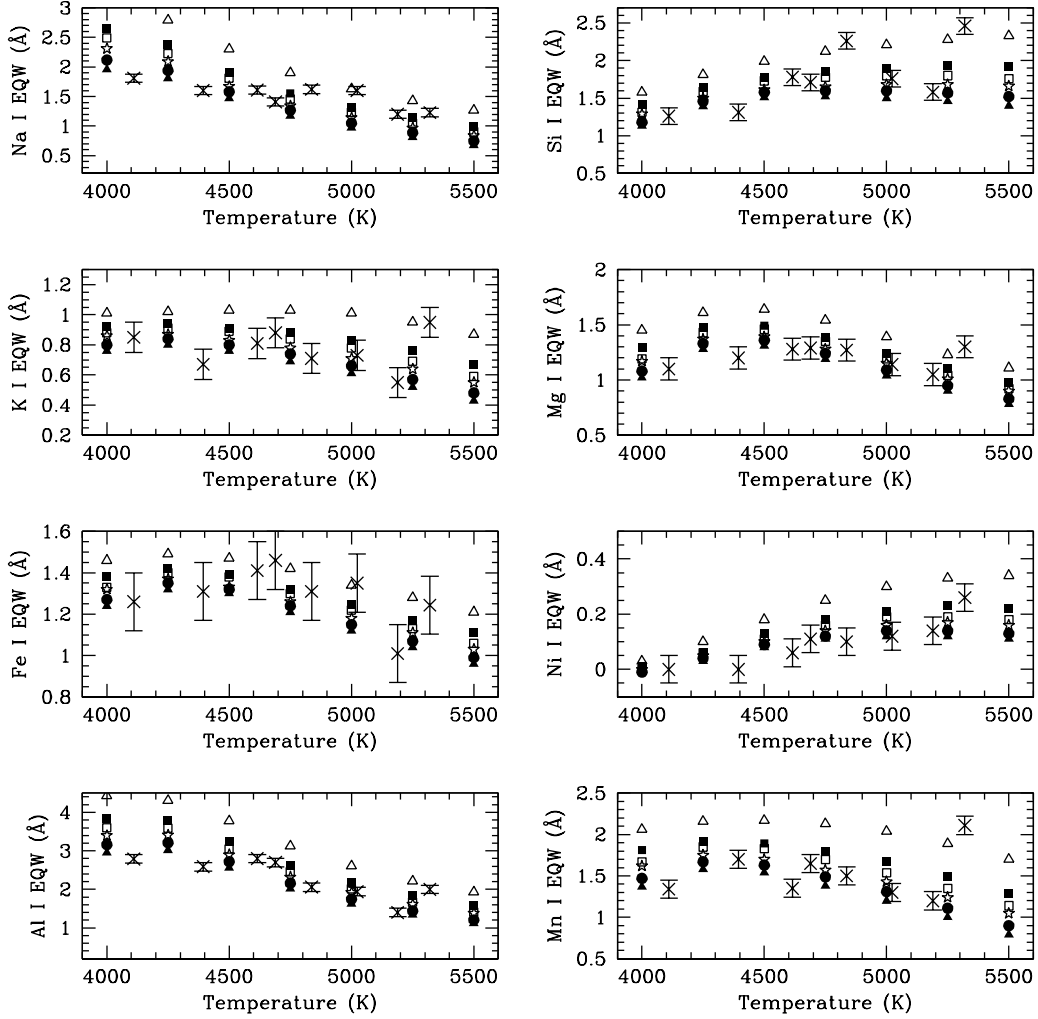


Fig. 3abc.— The equivalent width measurements (crosses with error bars) in the *J*-band for the K type dwarfs listed in Table 3, plotted against those measured from the synthetic spectra for five metallicities:  $[\text{Fe}/\text{H}] = 0.0$  (stars),  $[\text{Fe}/\text{H}] = +0.1$  (open squares),  $[\text{Fe}/\text{H}] = +0.2$  (filled squares),  $[\text{Fe}/\text{H}] = +0.5$  (open triangles),  $[\text{Fe}/\text{H}] = -0.1$  (filled circles), and  $[\text{Fe}/\text{H}] = -0.2$  (filled triangles).

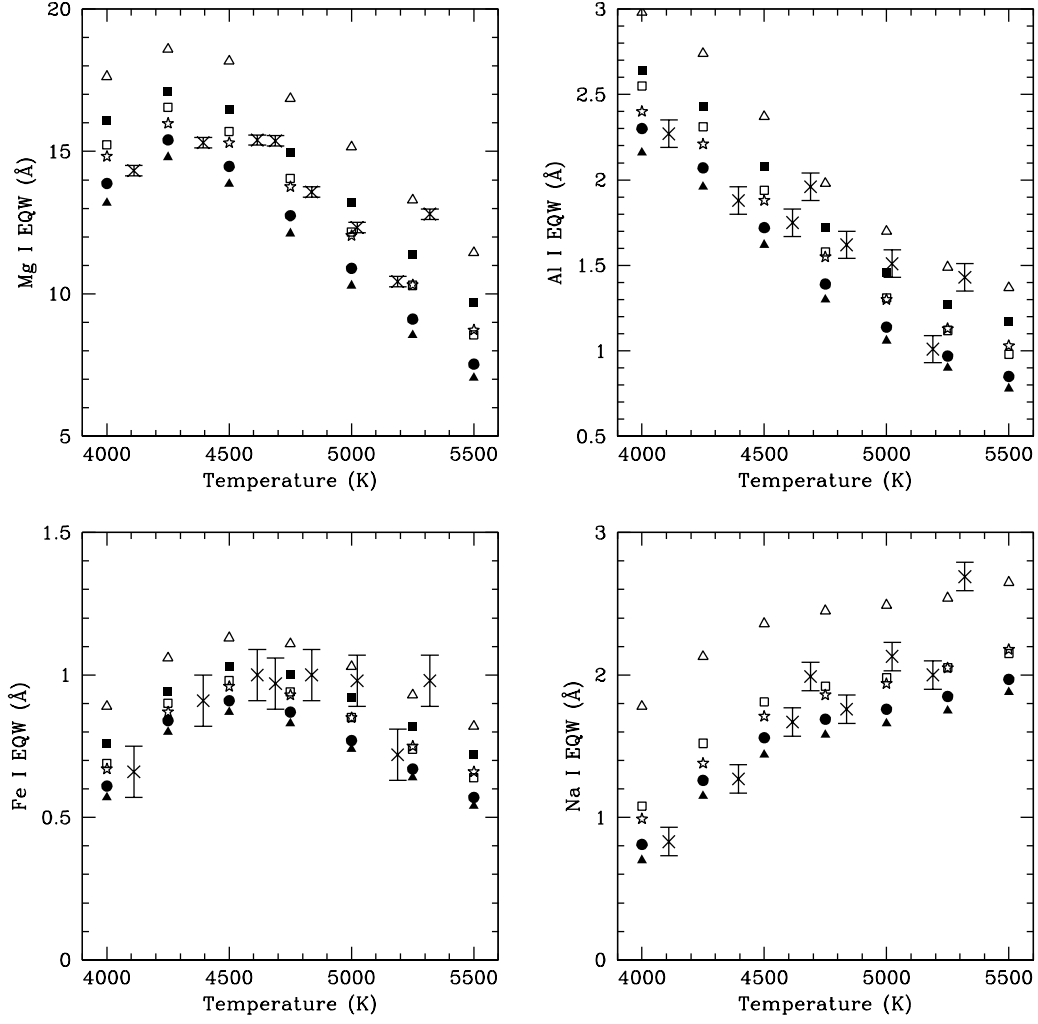


Fig. 3b.— Same as 3a, but for the  $H$ -band.

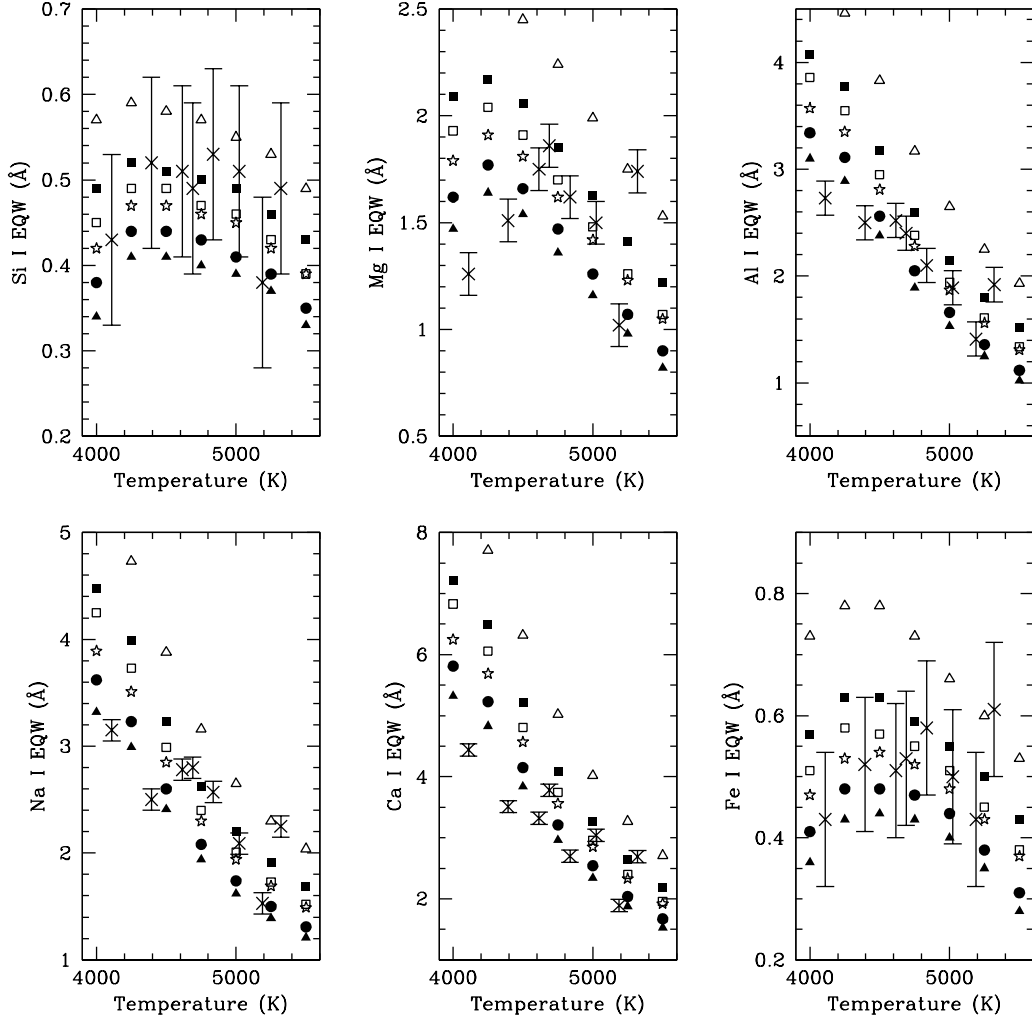


Fig. 3c.— Same as 3a, but for the *K*-band.

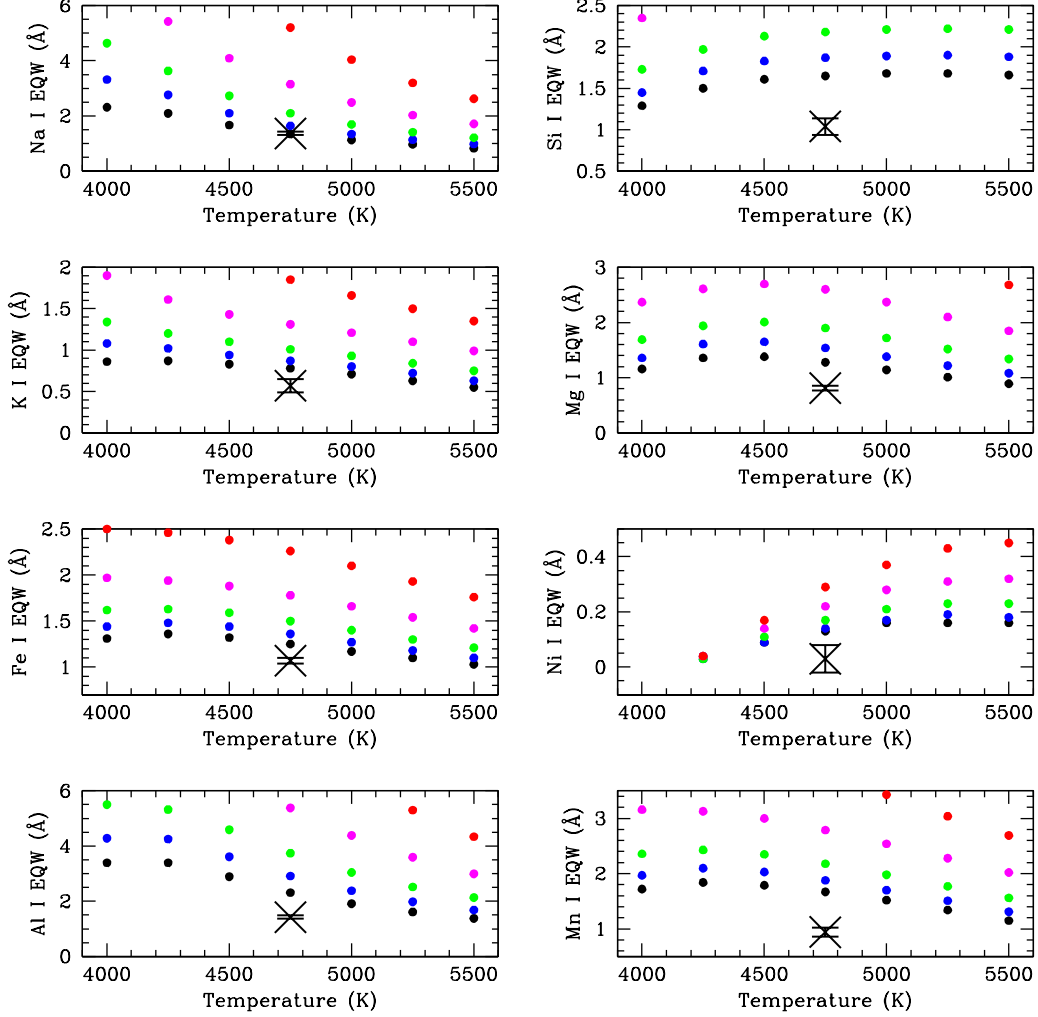


Fig. 4abc.— The fit of the  $J$ -band EQW measurements for SS Cyg to those for the model synthetic spectra with  $\log g = 4.5$ , and  $[\text{Fe}/\text{H}] = 0.0$ . The filled black circles are for no hydrogen deficit, blue circles are for a hydrogen deficit of 25%, green is for a deficit of 50%, magenta for a deficit of 75%, and red for a deficit of 90%.

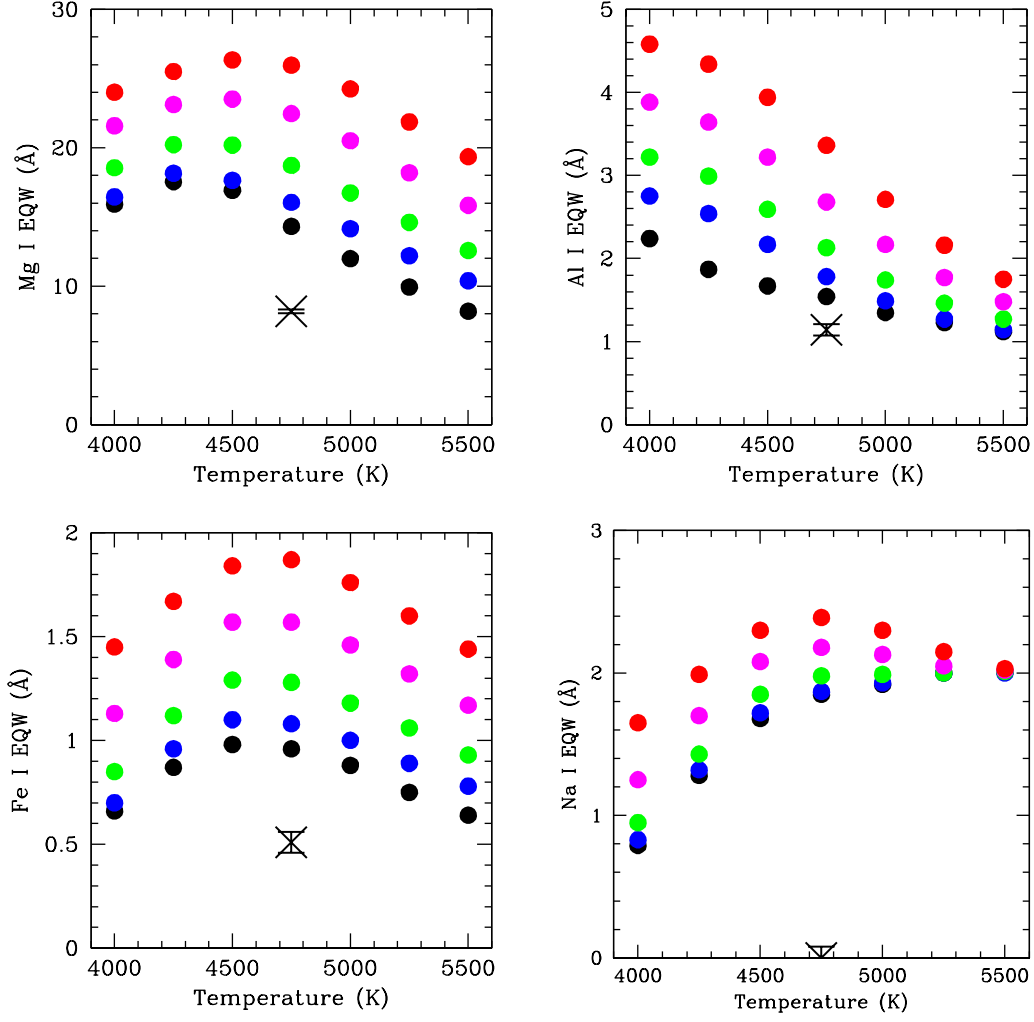


Fig. 4b.— The same as panel *a*, but for the *H*-band.

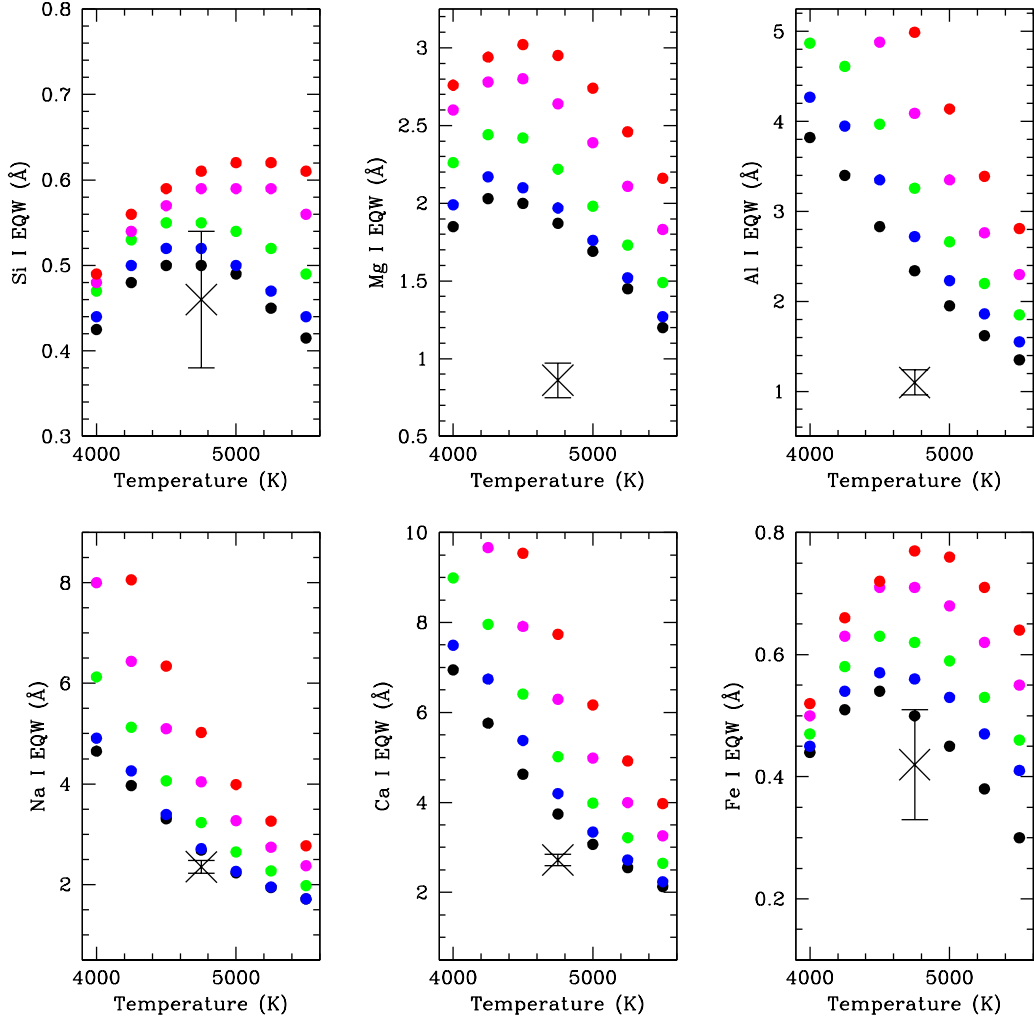


Fig. 4c.— The same as panel *a*, but for the *K*-band.

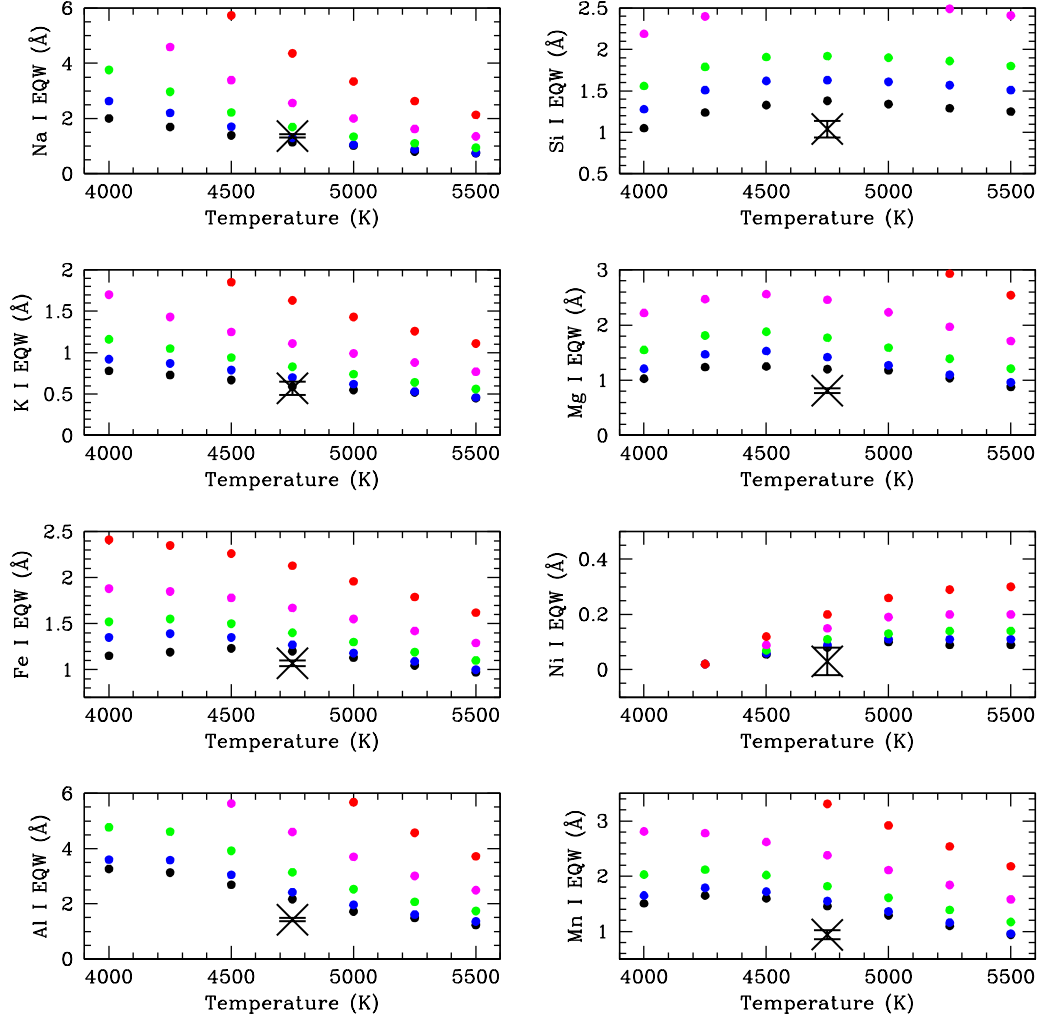


Fig. 5abc.— As in Fig. 4abc, but for  $[\text{Fe}/\text{H}] = -0.3$ .

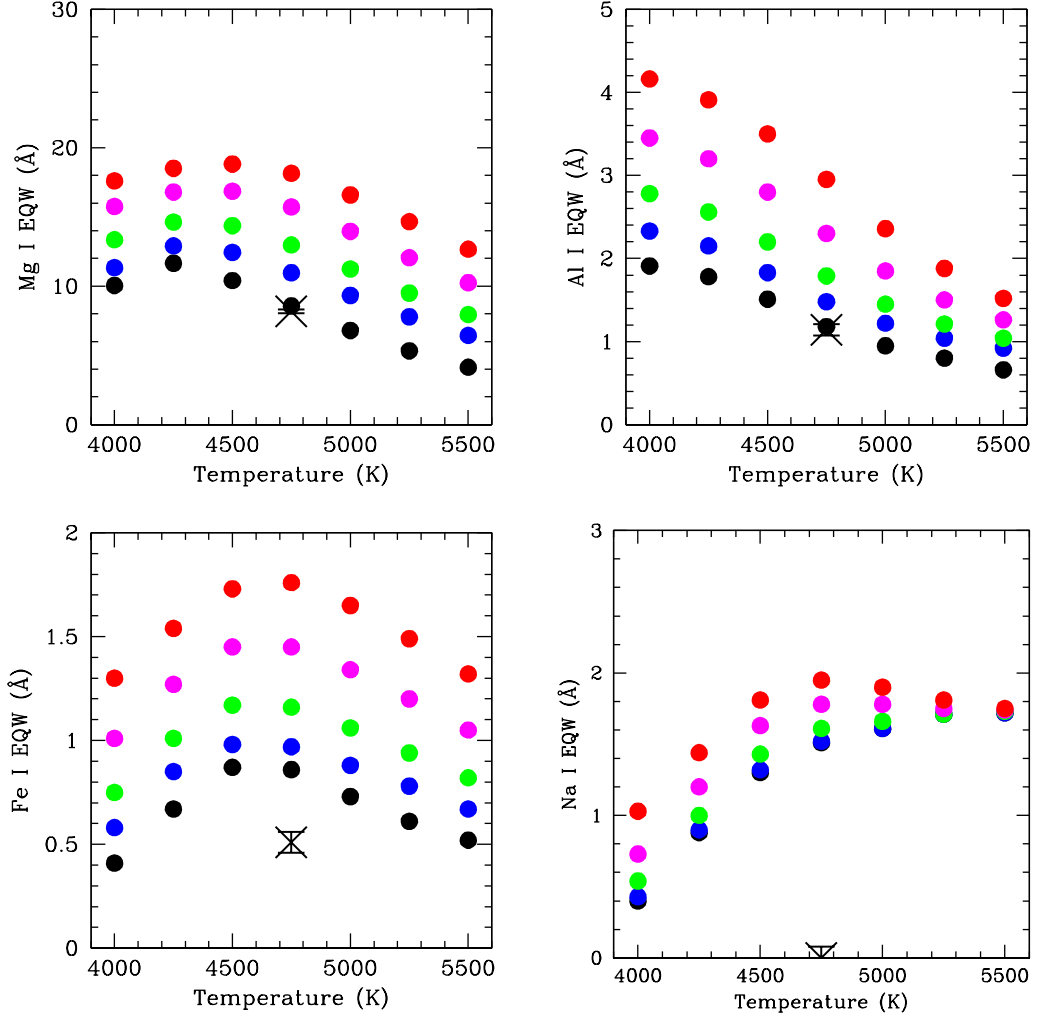


Fig. 5b.— Same as panel *a*, but for the *H*-band.

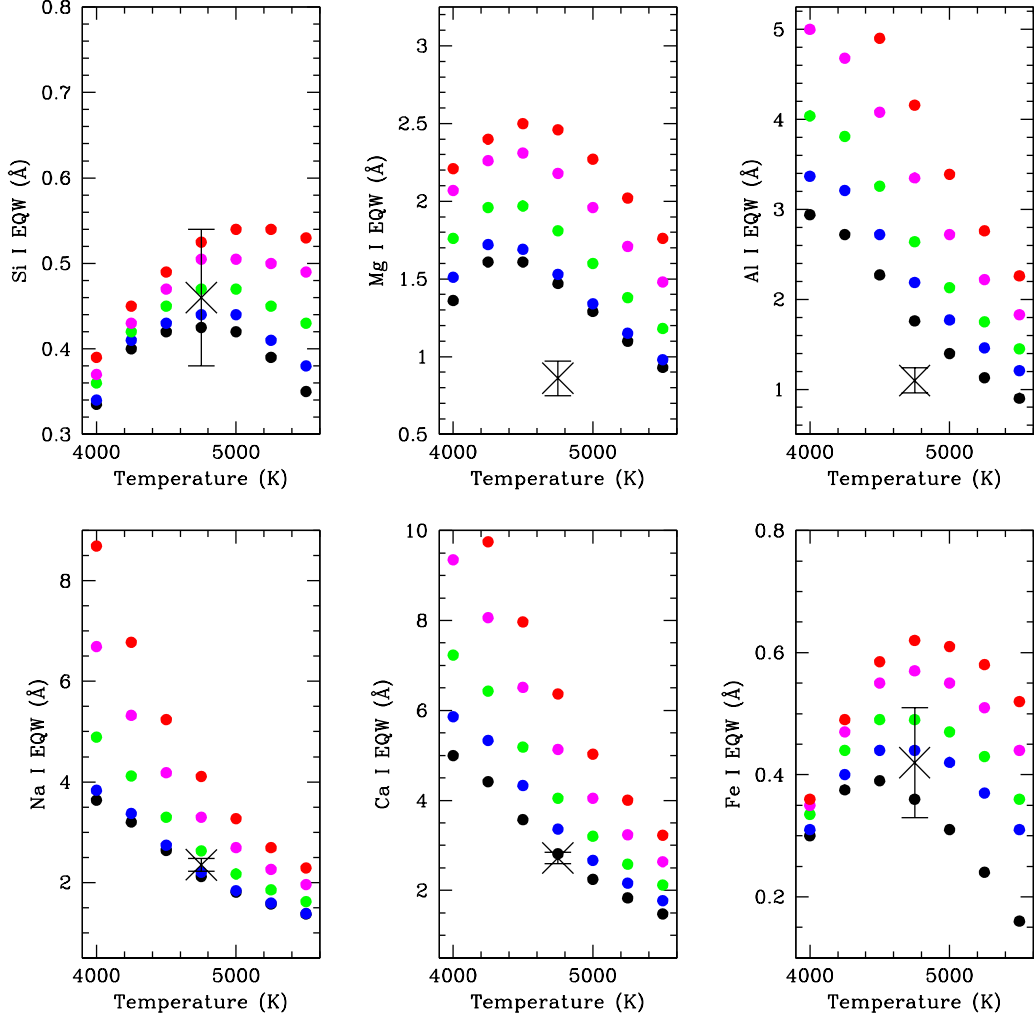


Fig. 5c.— The same as panel *a*, but for the *K*-band.

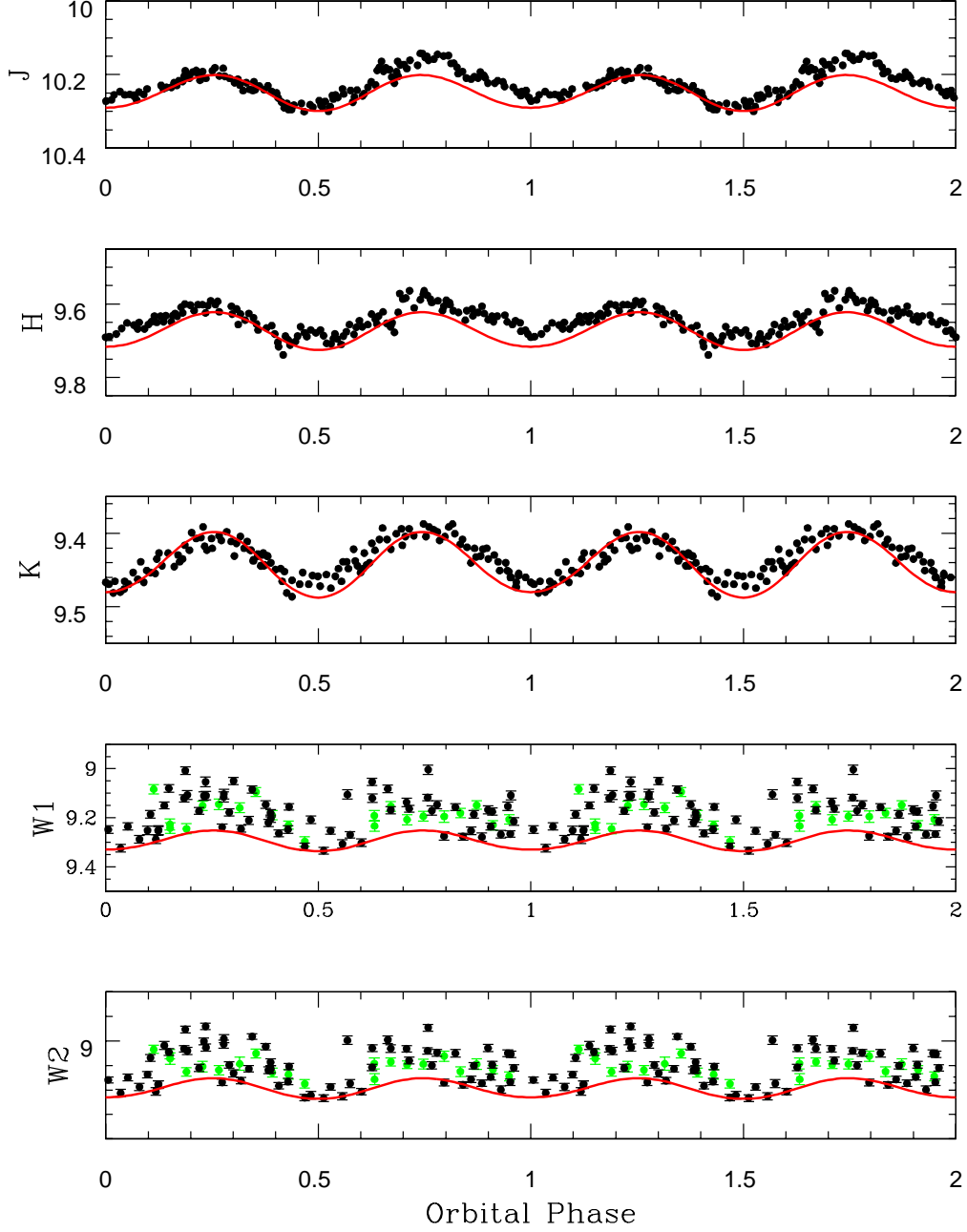


Fig. 6.— The  $JHK$  and  $WISE/NEOWISE$  light curves of SS Cyg. In the  $W1$  ( $3.4 \mu\text{m}$ ) and  $W2$  ( $4.6 \mu\text{m}$ ) panels, the  $WISE$  light curve data is plotted in green, and the  $NEOWISE$  data is plotted in black. The model light curve is in red and has  $T_{\text{eff}_1} = 20,000 \text{ K}$ ,  $T_{\text{eff}_2} = 4750 \text{ K}$ ,  $i = 45^\circ$ , with a contamination level of 25% from the white dwarf, accretion disk and its hot spot.

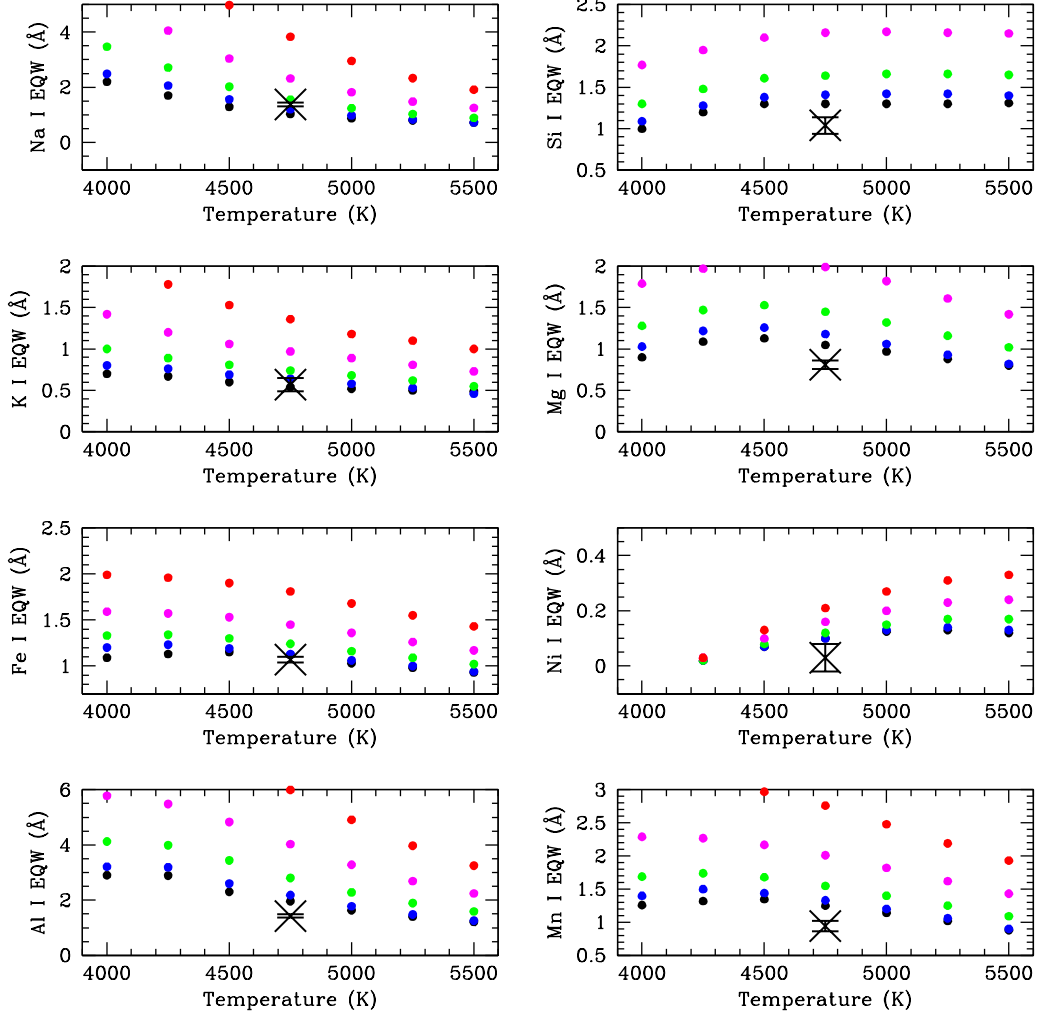


Fig. 7abc.— The fit of the  $J$ -band EQW measurements for SS Cyg to those for the model synthetic spectra with  $[\text{Fe}/\text{H}] = 0.0$  and with the donor star supplying 75% of the broadband flux.

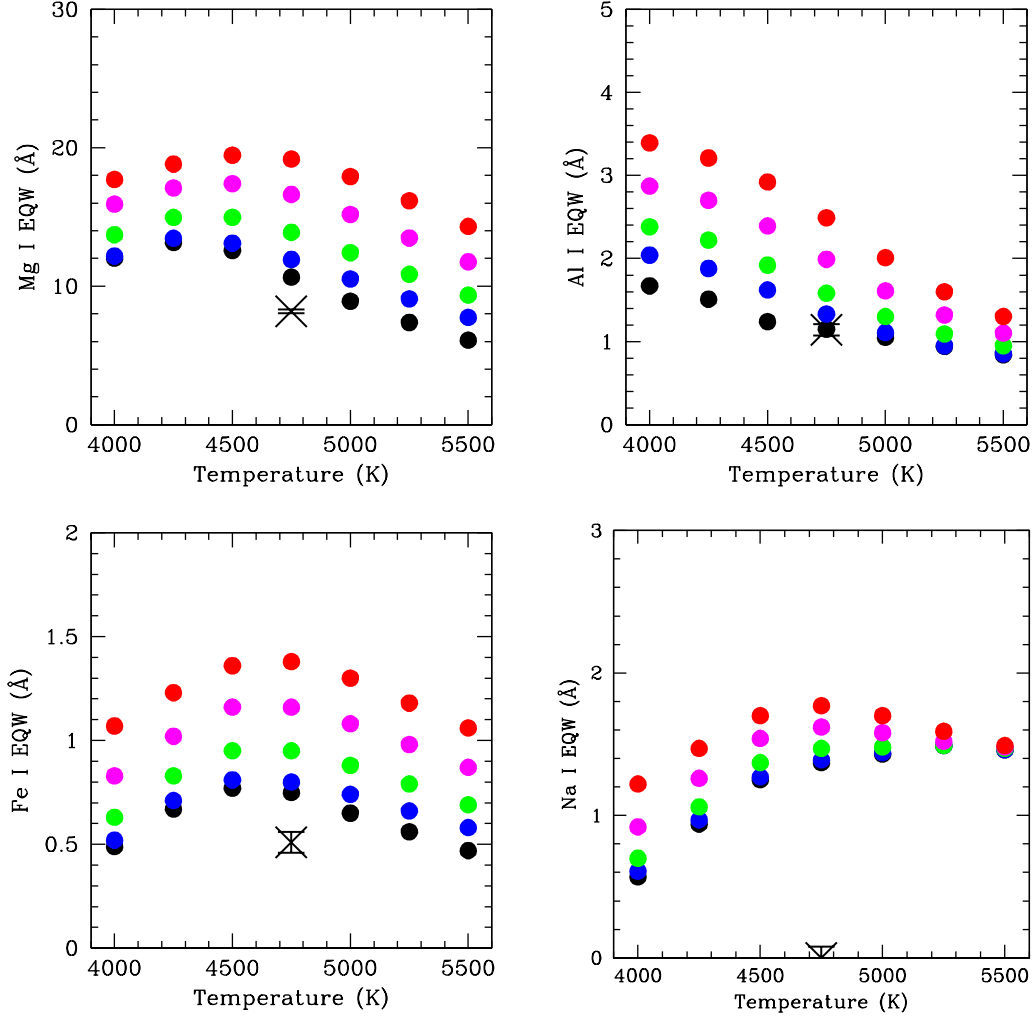


Fig. 7b.— The same as in panel *a*, but for the *H*-band.

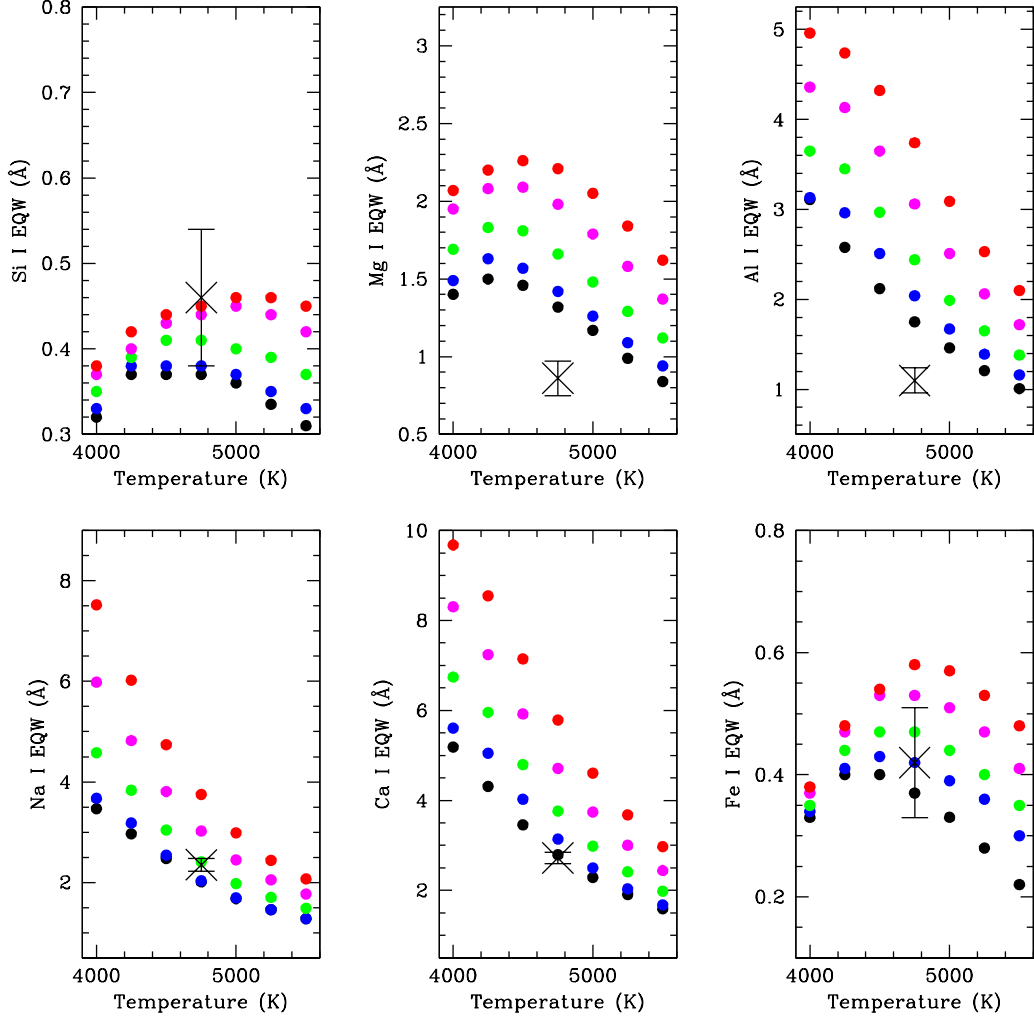


Fig. 7c.— The same as as in panel *a*, but for the *K*-band.

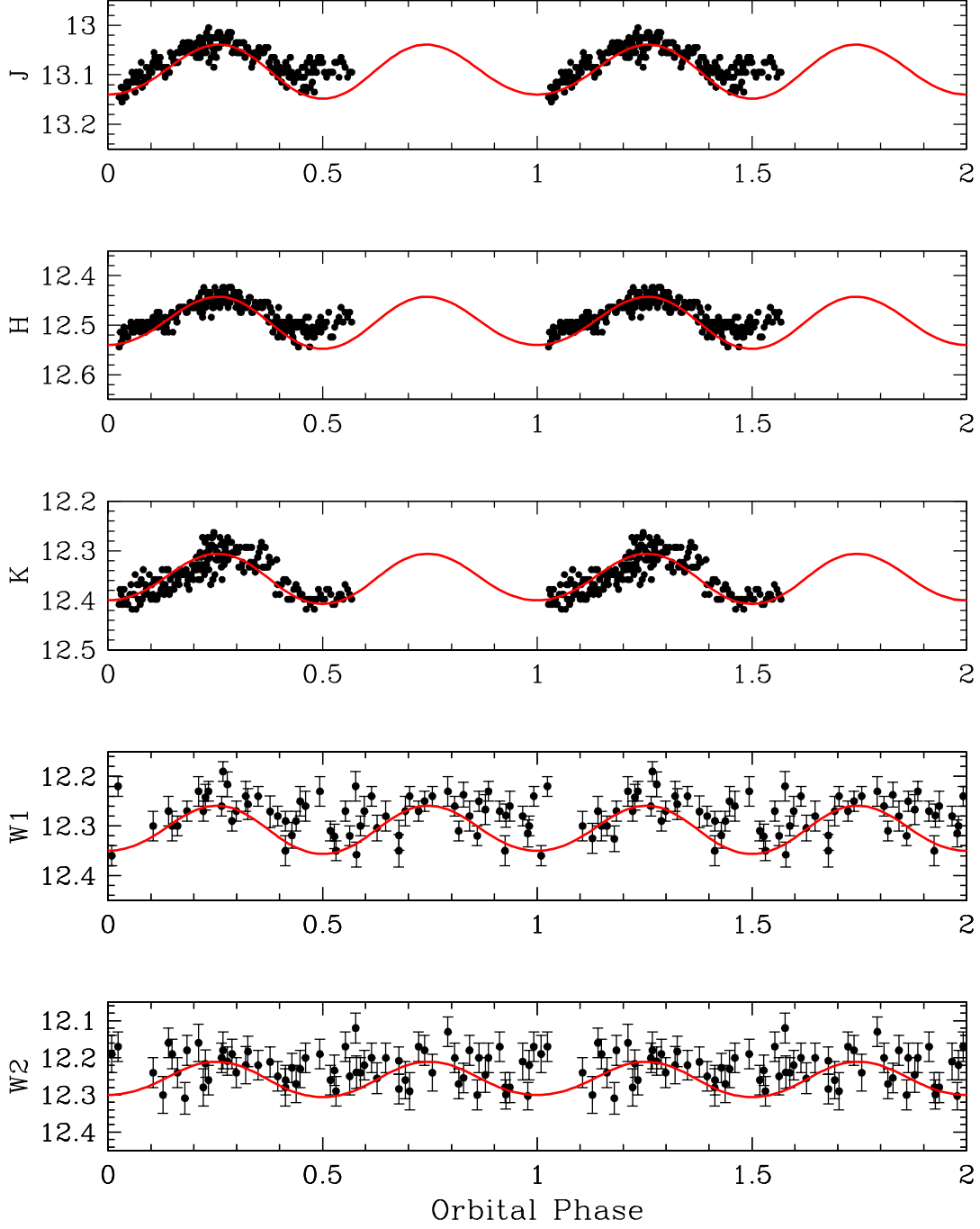


Fig. 8.— The *JHK* and *WISE/NEOWISE* light curves of DX And. Using the AAVSO data base, DX And was in a quiescent state for all epochs of observation. The light curve model (red) has  $T_{\text{eff}1} = 25,000$  K,  $T_{\text{eff}2} = 5,000$  K,  $q = 0.96$ , and  $i = 45^\circ$ .

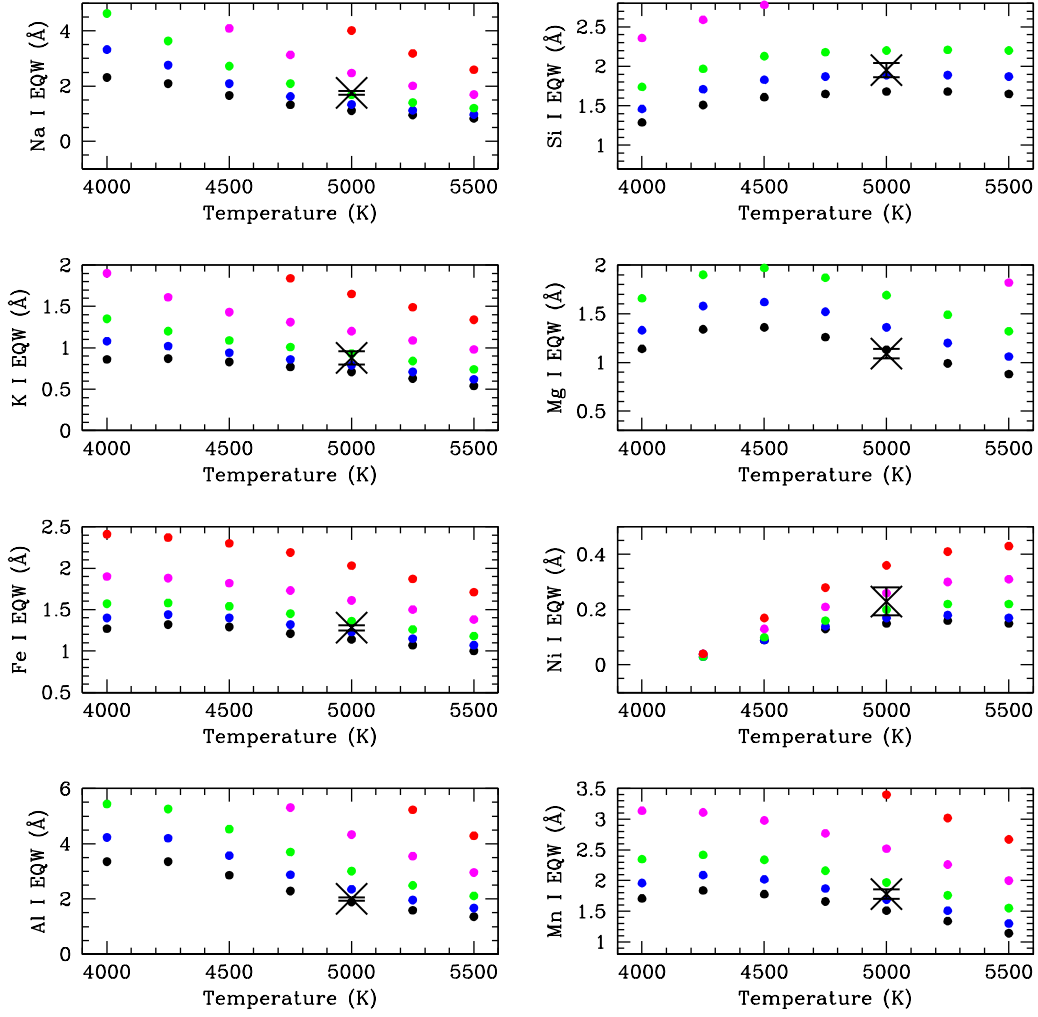


Fig. 9abc.— The fit of the  $J$ -band EQW measurements for DX And to those for the synthetic spectra with  $\log g = 4.5$ , and  $[\text{Fe}/\text{H}] = 0.0$ .

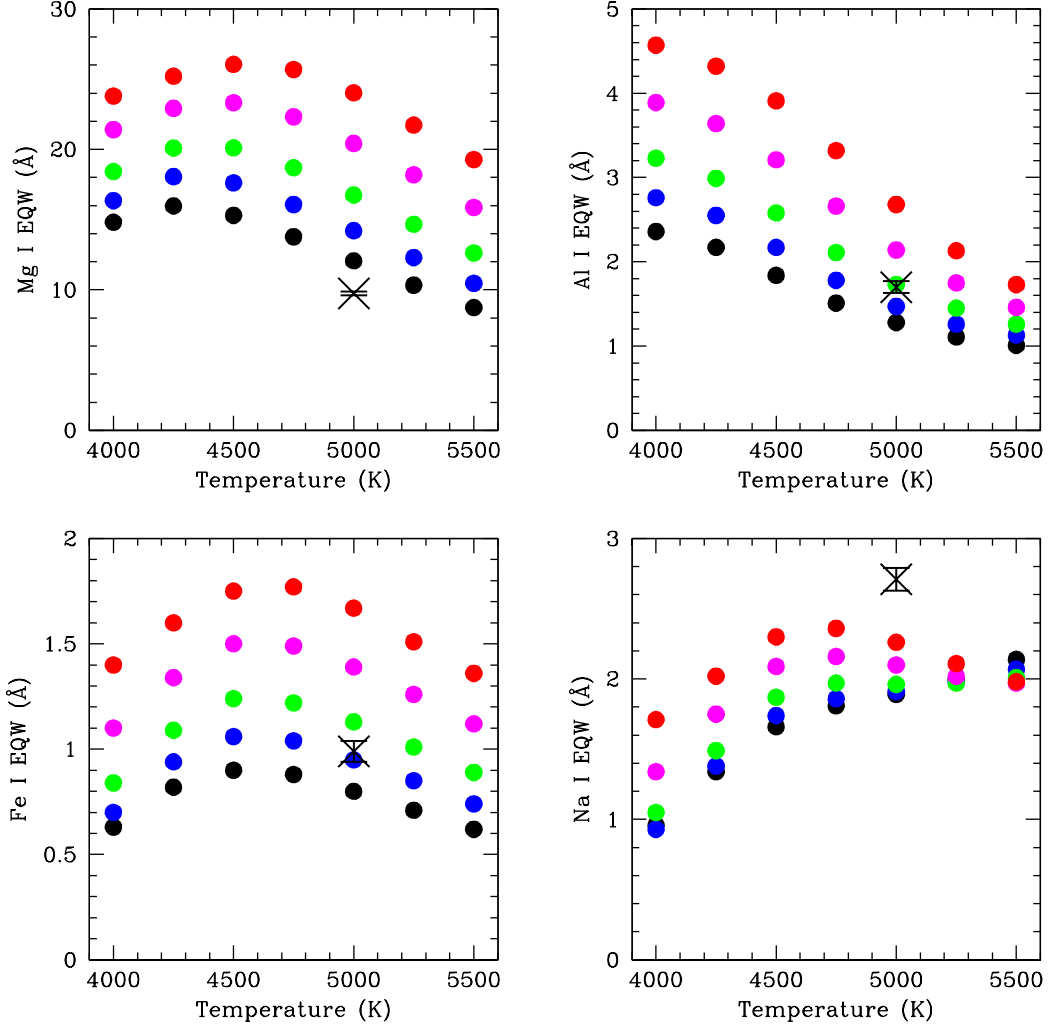


Fig. 9b.— The same as panel *a*, but for the *H*-band.

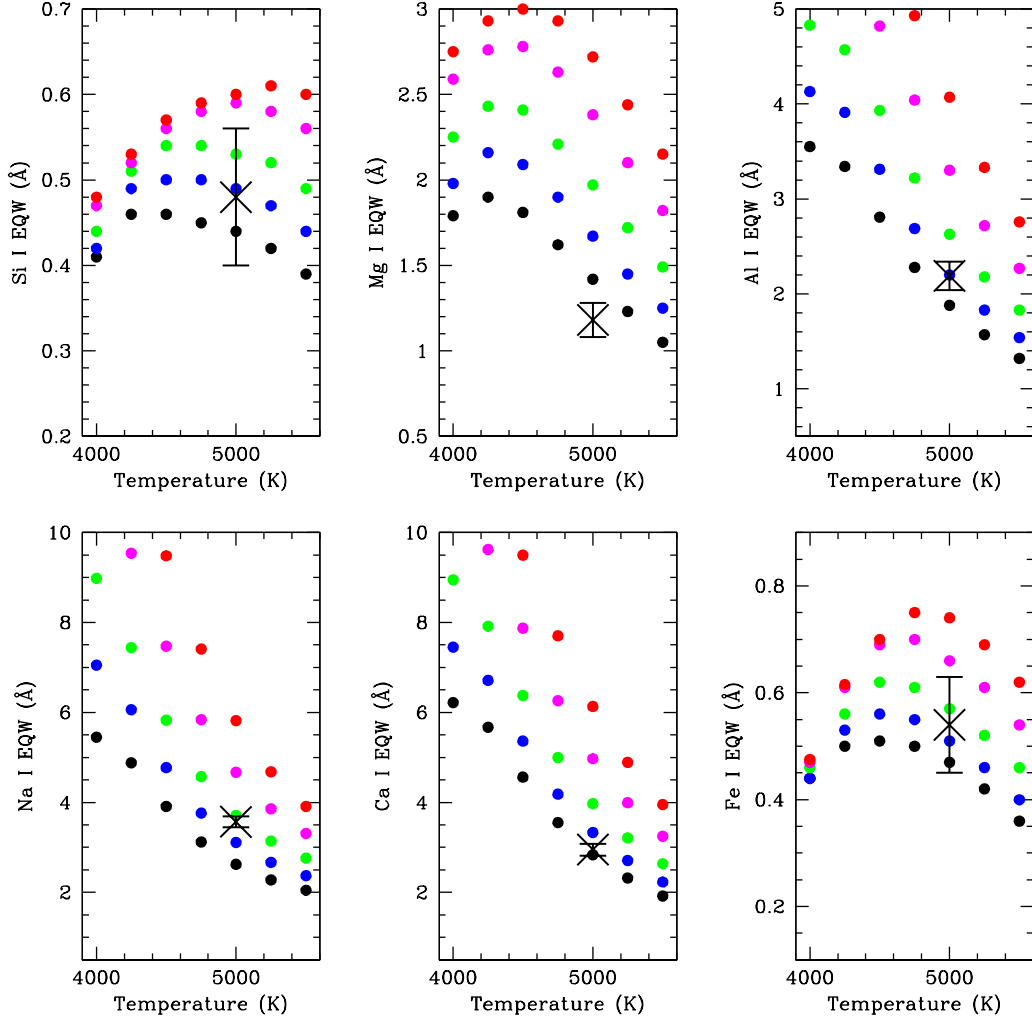


Fig. 9c.— The same as panel *a*, but for the *K*-band.

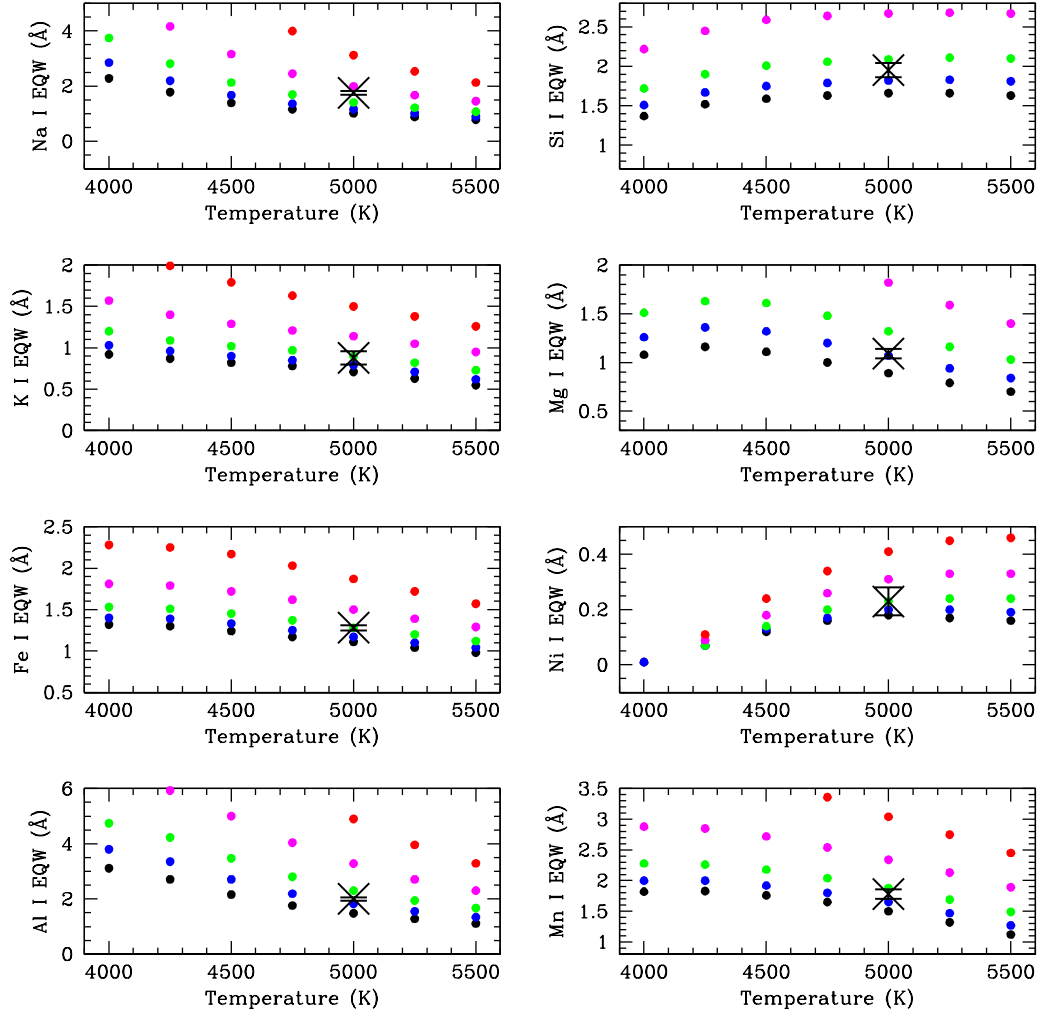


Fig. 10abc.— The fit of the  $J$ -band EQW measurements for DX And to those for the synthetic spectra with  $\log g = 4.0$ , and  $[\text{Fe}/\text{H}] = 0.0$ .

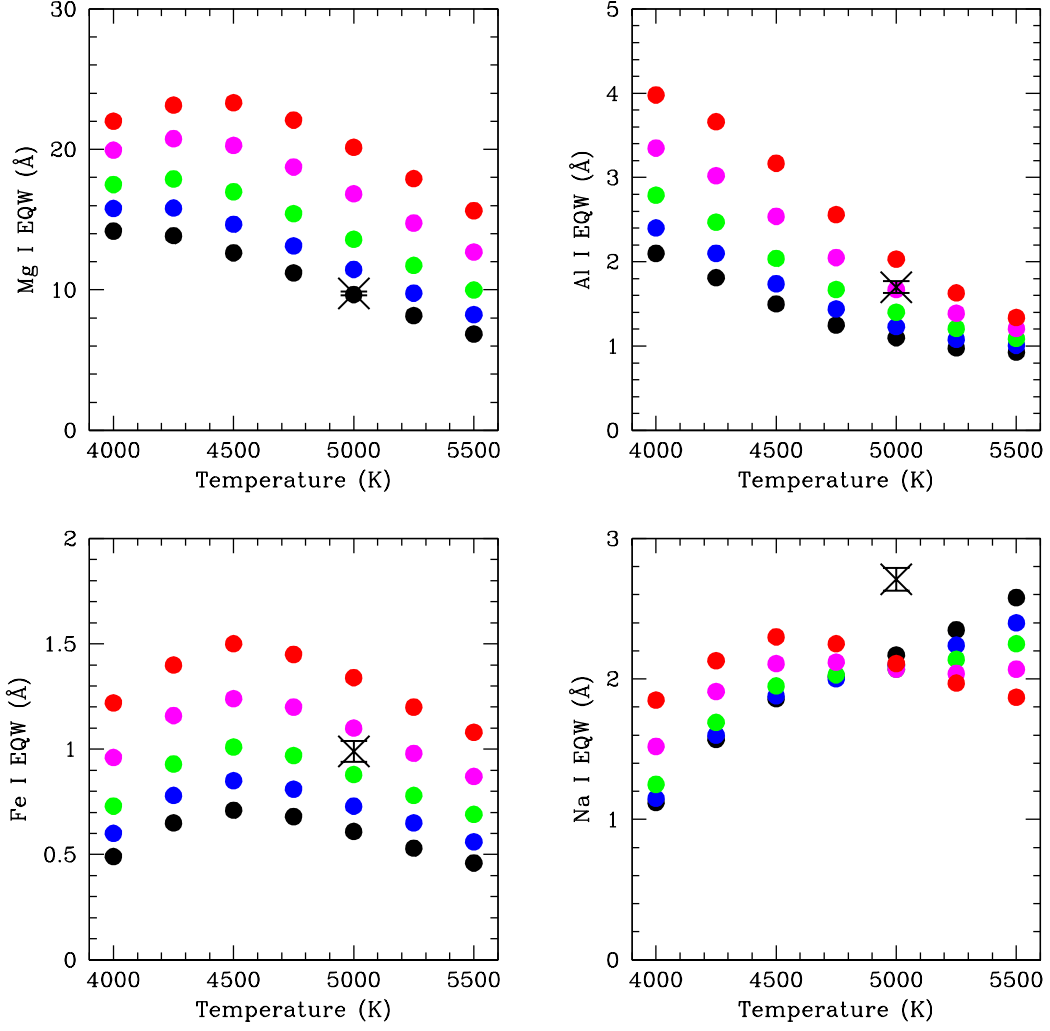


Fig. 10b.— The same as panel *a*, but for the *H*-band.

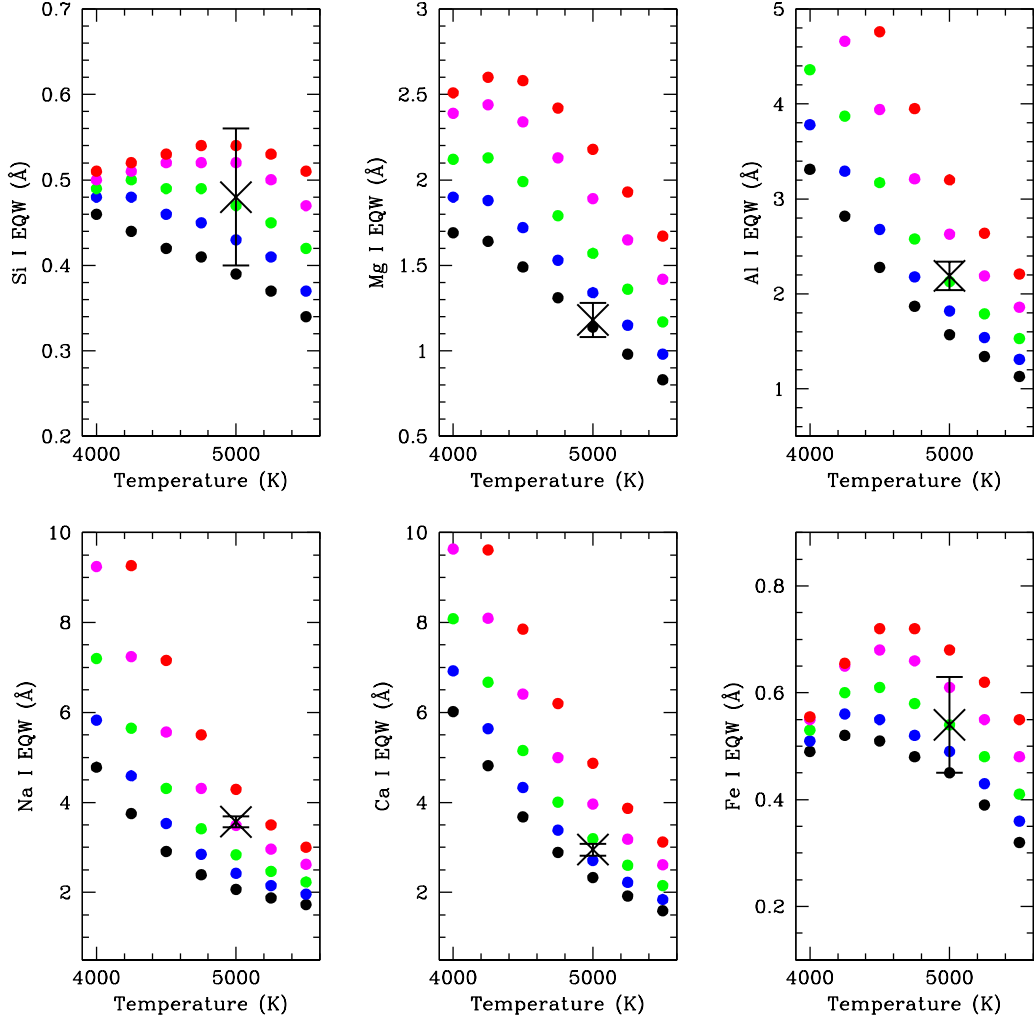


Fig. 10c.— The same as panel *a*, but for the *K*-band.

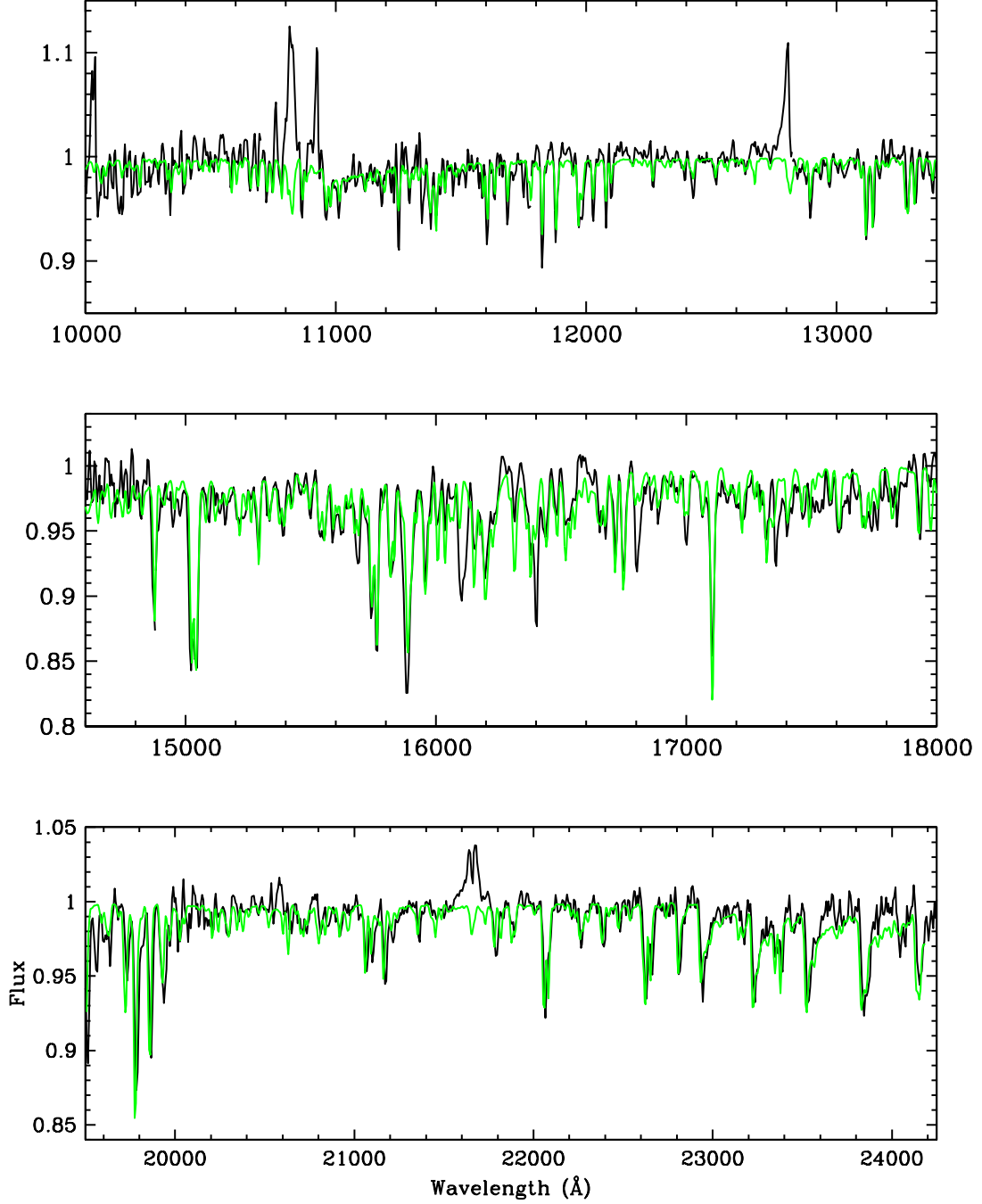


Fig. 11.— The Gemini GNIRS spectrum (black) of DX And compared to a synthetic spectrum (green) with  $T_{\text{eff}} = 5000$  K,  $\log g = 4.0$ ,  $[\text{Fe}/\text{H}] = 0.0$ ,  $\text{Hd} = 50\%$ ,  $[\text{C}/\text{Fe}] = -0.7$ ,  $[\text{Mg}/\text{Fe}] = -0.2$ , and  $[\text{Na}/\text{Fe}] = +0.5$ .

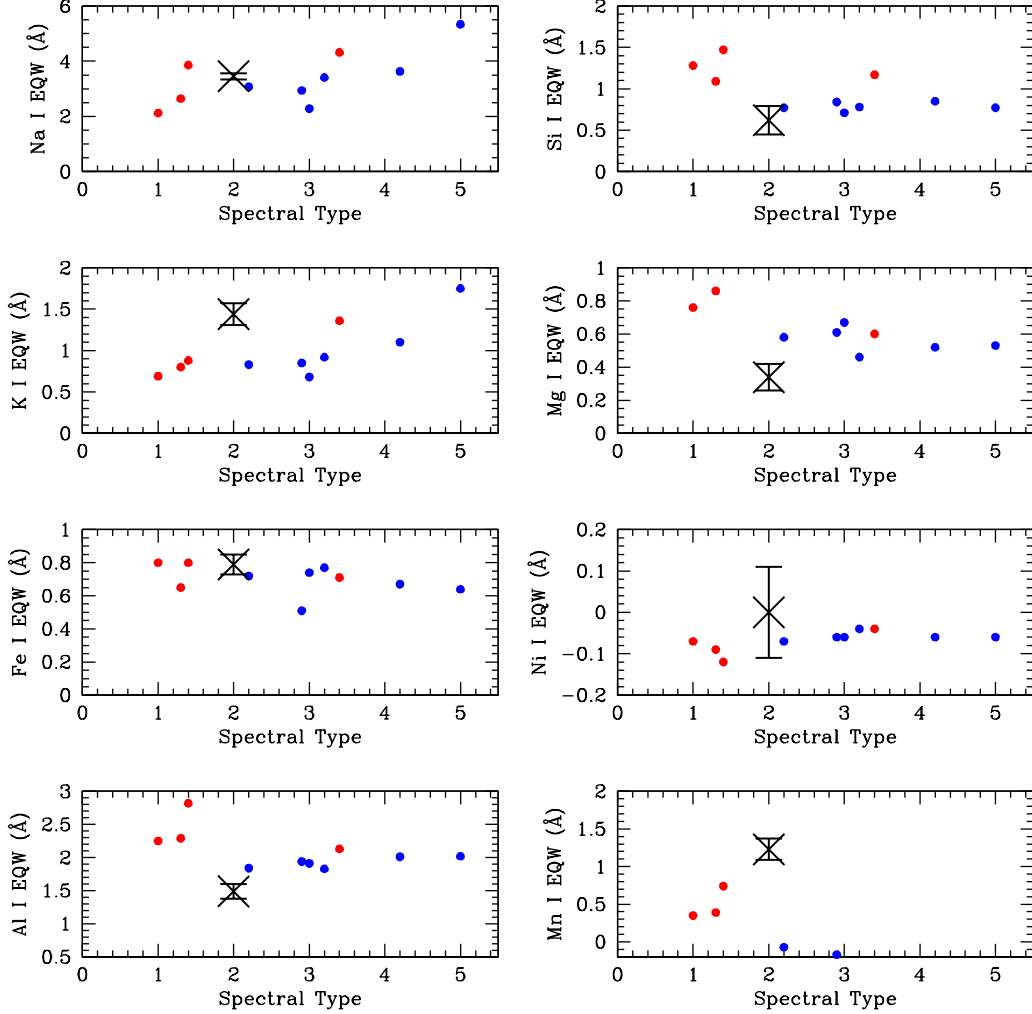


Fig. 12abc.— The plot of the EQW measurements in the  $J$ -band of RX And versus those for the M dwarfs in the IRTF Spectral Library (Cushing et al. 2005) for the same set of elements used above. The abundances and spectral types of the M dwarfs were generated using the techniques discussed in H16. The x-axis is spectral type, ranging from M0V to M5V. The data plotted in blue are the EQW measures for M dwarfs with  $[\text{Fe}/\text{H}] < 0$ , while those in red are for  $[\text{Fe}/\text{H}] > 0$ .

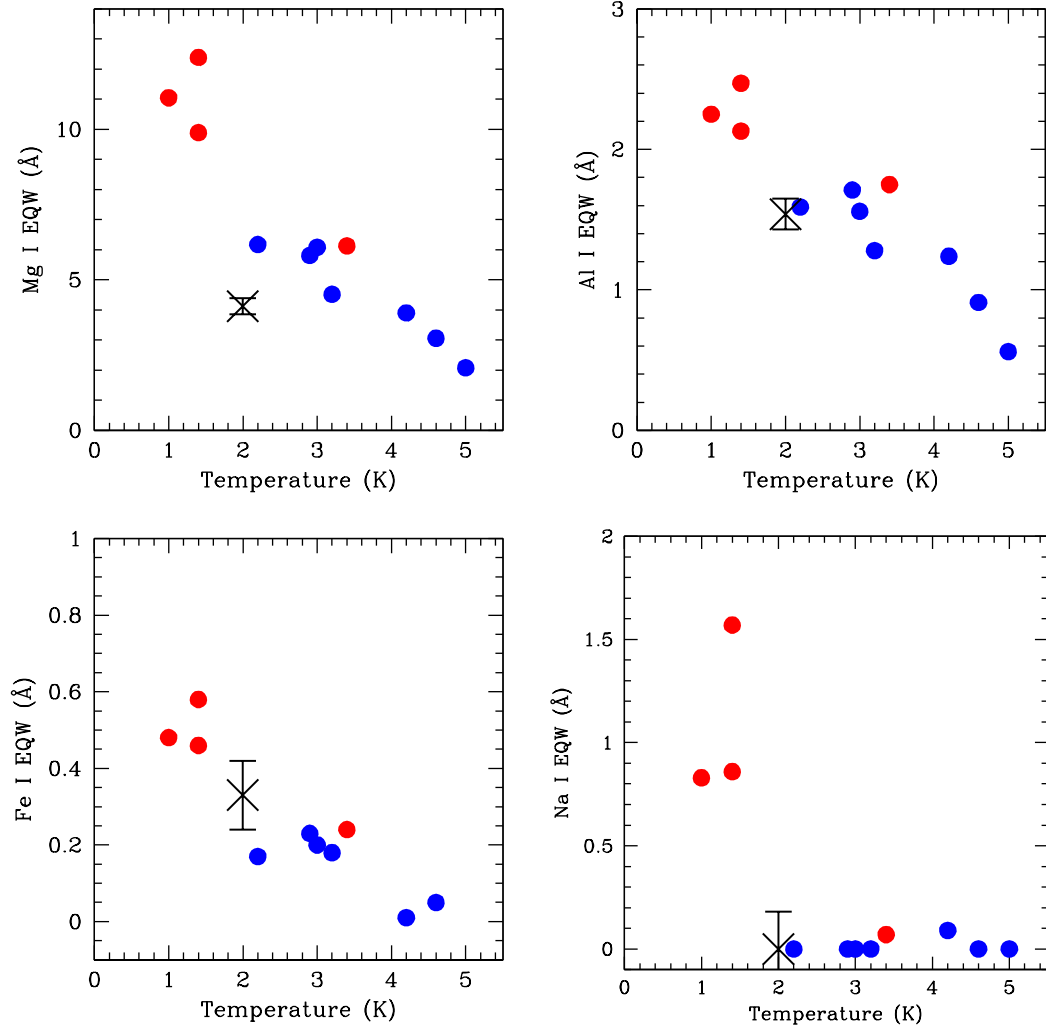


Fig. 12b.— The same as panel *a*, but for the *H*-band.

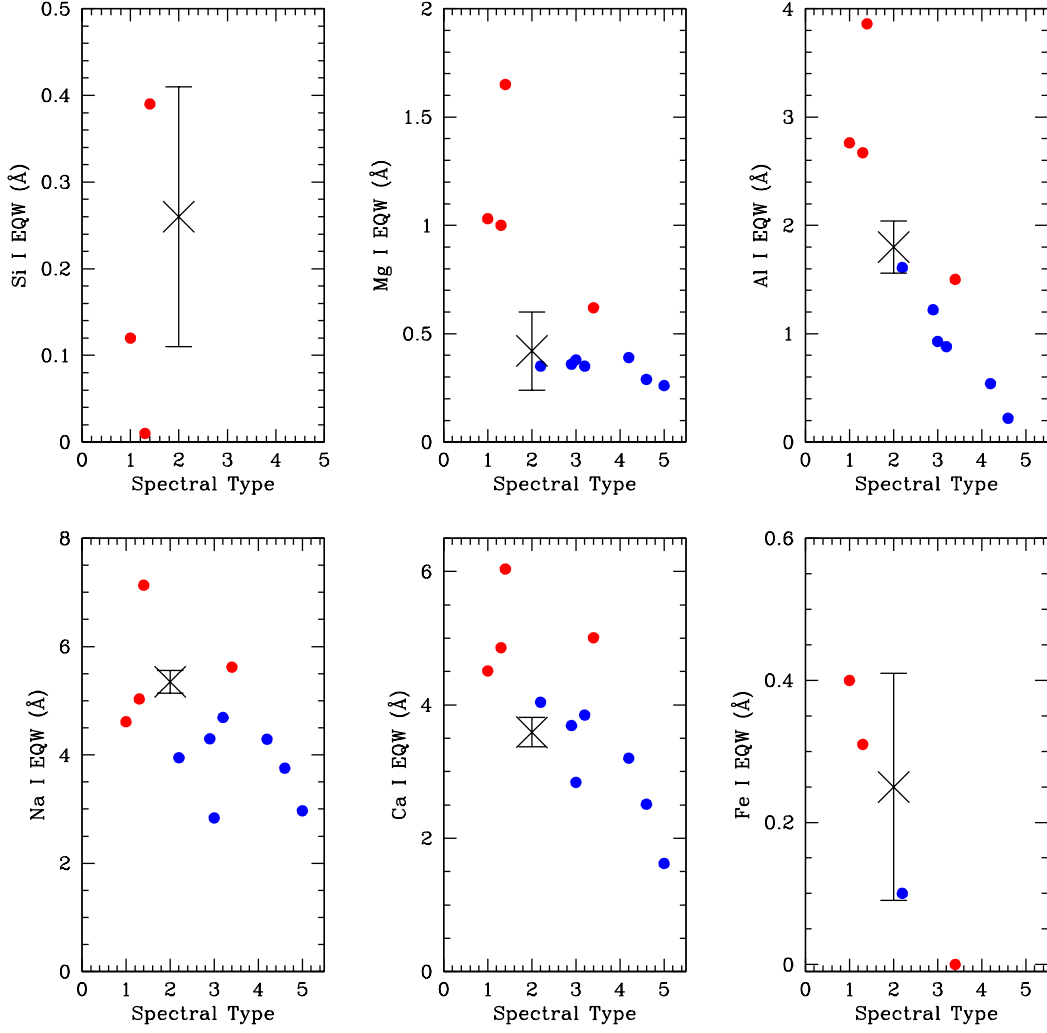


Fig. 11c.— The same as panel *a*, but for the *K*-band.

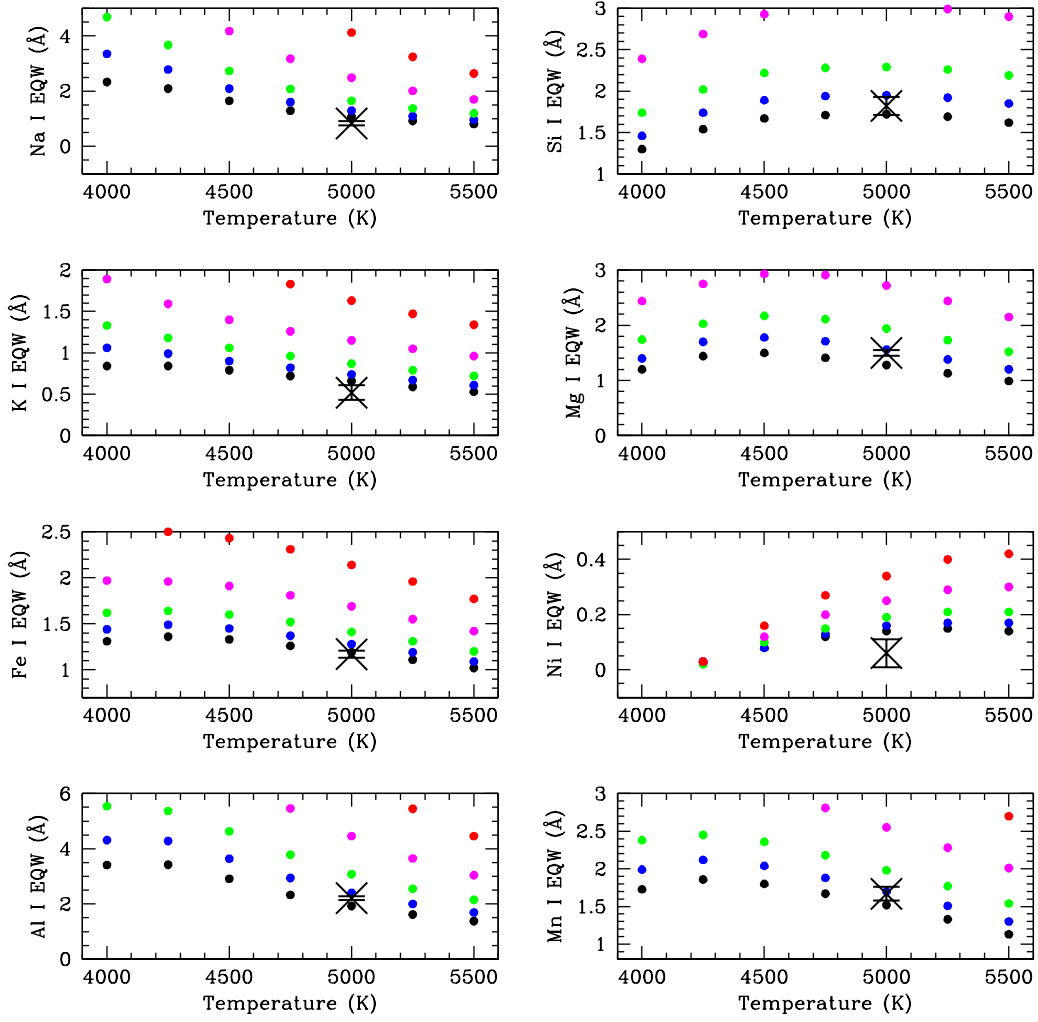


Fig. 13abc.— The fit of the *J*-band EQW measurements for AE Aqr to those for the model synthetic spectra with  $\log g = 4.5$ , and  $[\text{Fe}/\text{H}] = 0.0$ .

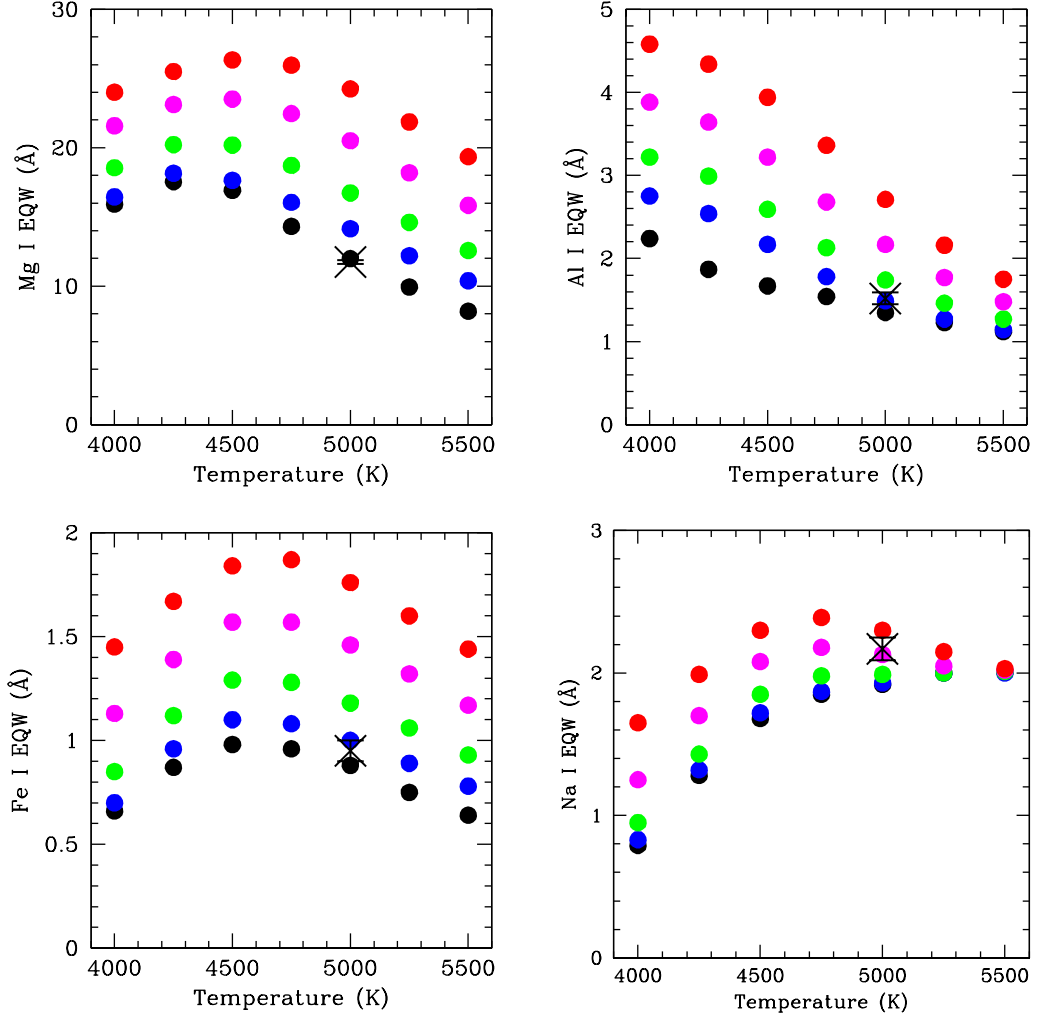


Fig. 13b.— The same as panel *a*, but for the *H*-band.

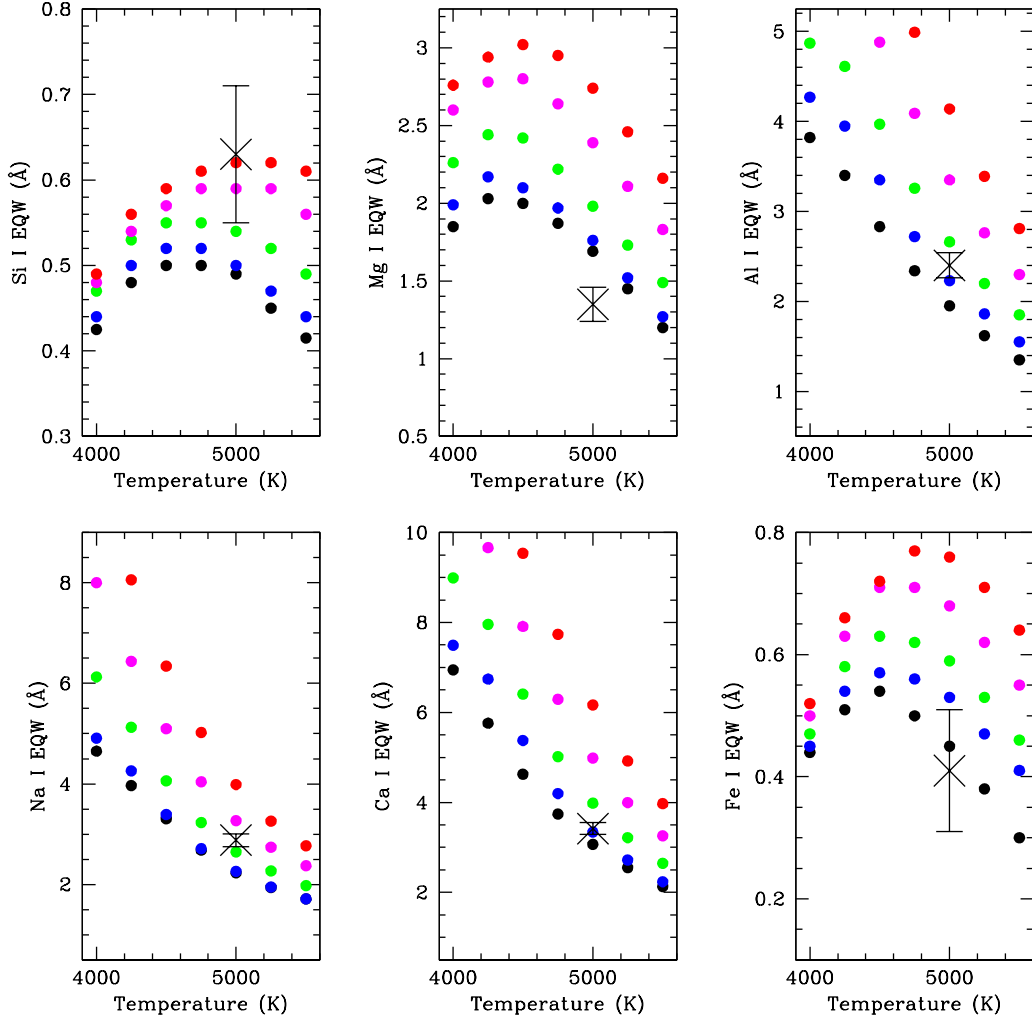


Fig. 13c.— The same as panel *a*, but for the *K*-band.

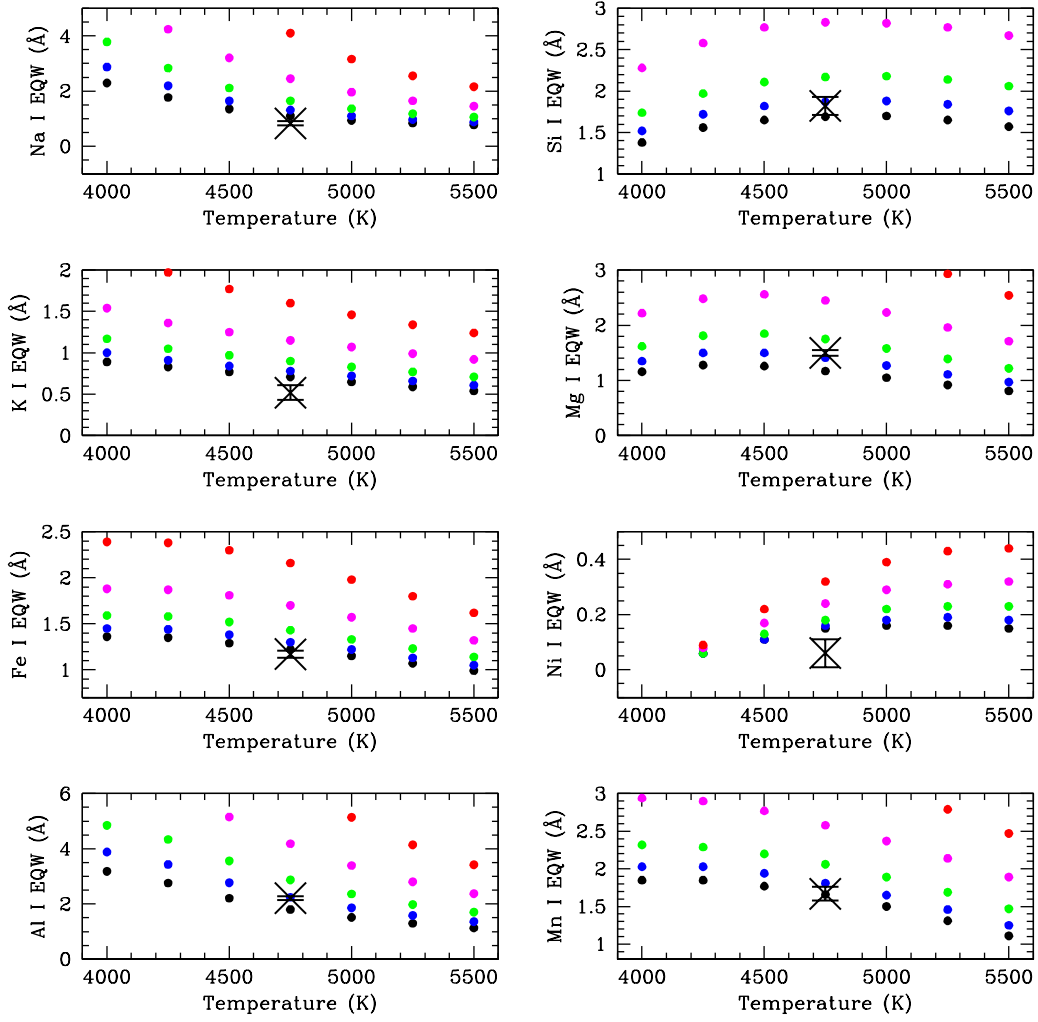


Fig. 14abc.— The fit of the *J*-band EQW measurements for AE Aqr to those for the synthetic spectra with  $\log g = 4.0$ , and  $[\text{Fe}/\text{H}] = 0.0$ .

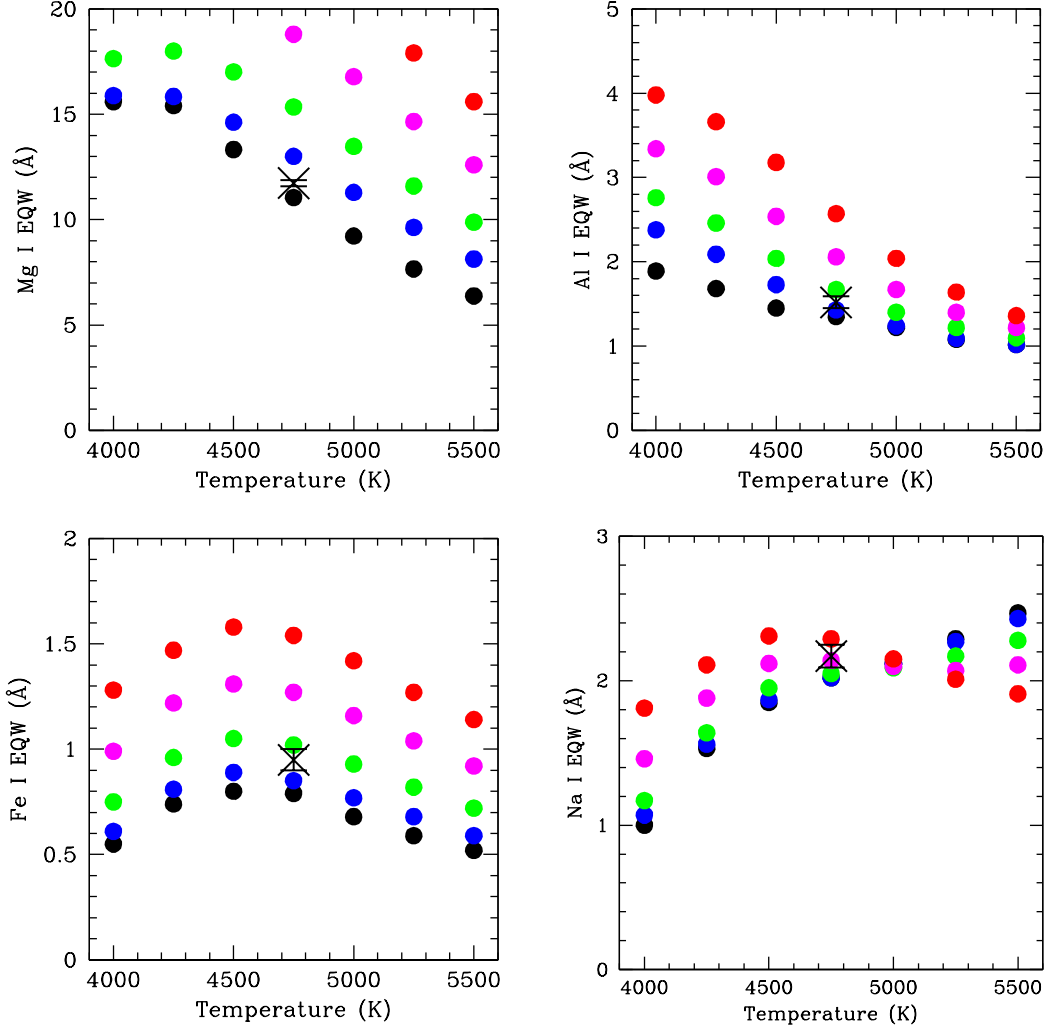


Fig. 14b.— The same as panel *a*, but for the *H*-band.

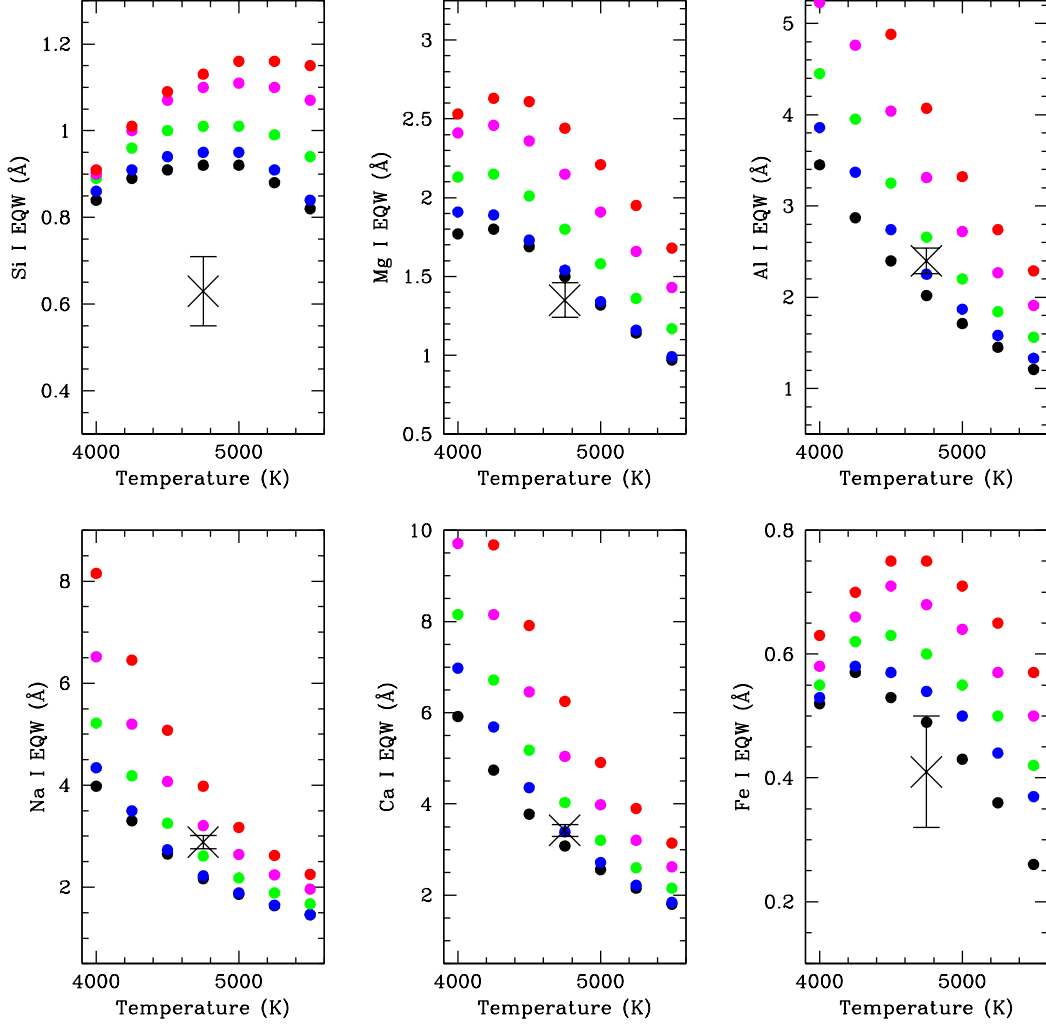


Fig. 14c.— The same as panel *a*, but for the *K*-band.

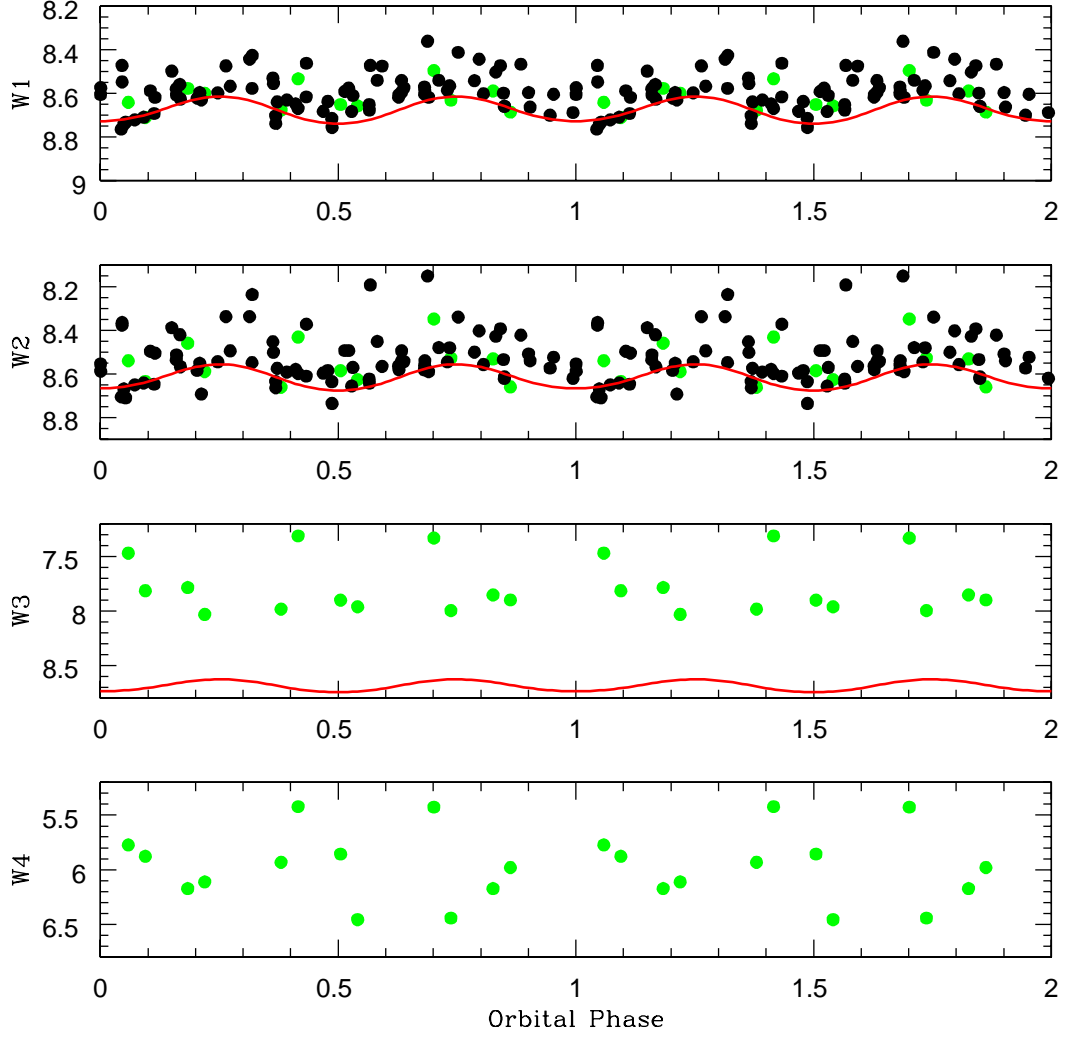


Fig. 15.— The *WISE* (green) and *NEOWISE* (black) light curves of AE Aqr.

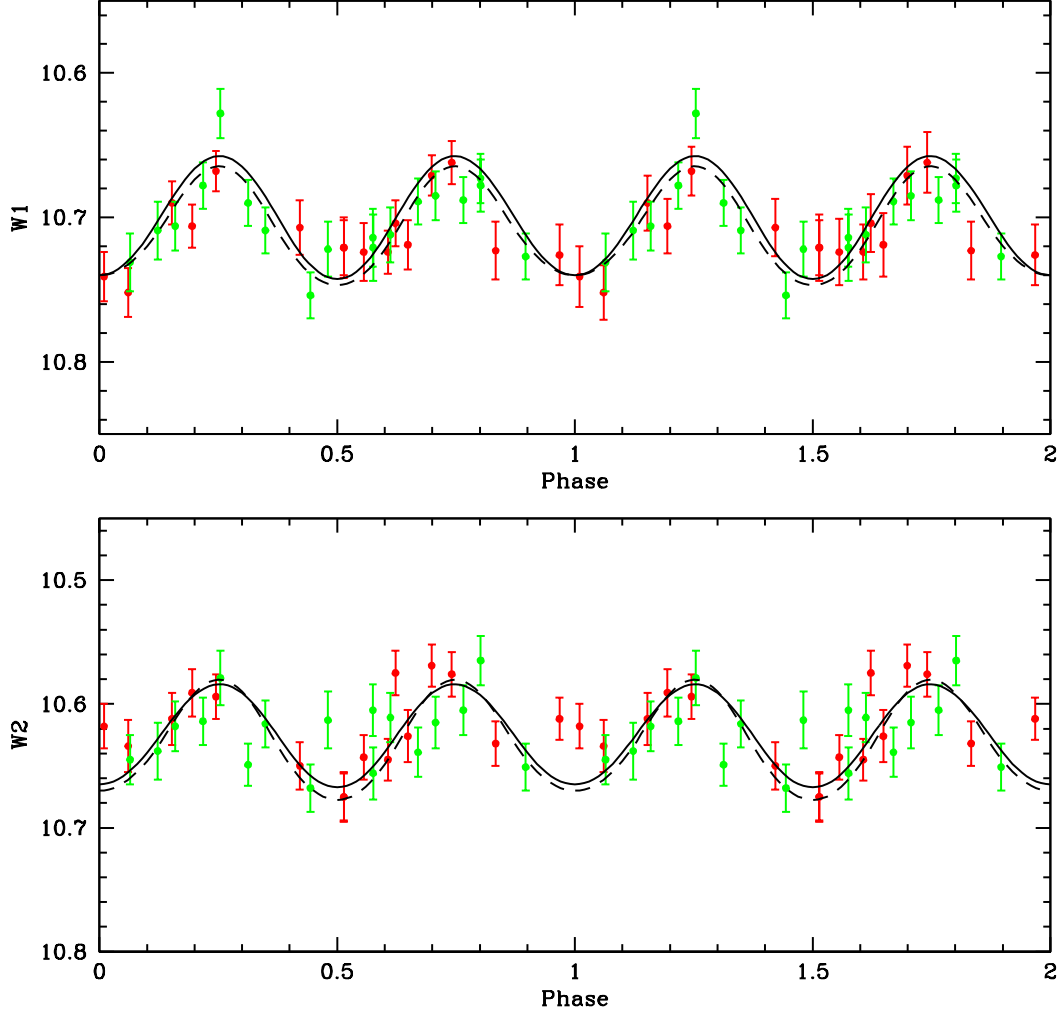


Fig. 16.— The *NEOWISE* light curves of Z Cam. The data for the 2014 October 10 epoch are plotted in red, and those for 2015 October 10 epoch are plotted in green. The photometry for 2014 has been offset by  $\Delta = +0.17$  mag so as to agree with the 2015 data. The solid black line is a light curve model with  $i = 40^\circ$ , while the dashed line has  $i = 57^\circ$ , and a contamination level of 32% in the *W1* band, and 28% in the *W2* band.

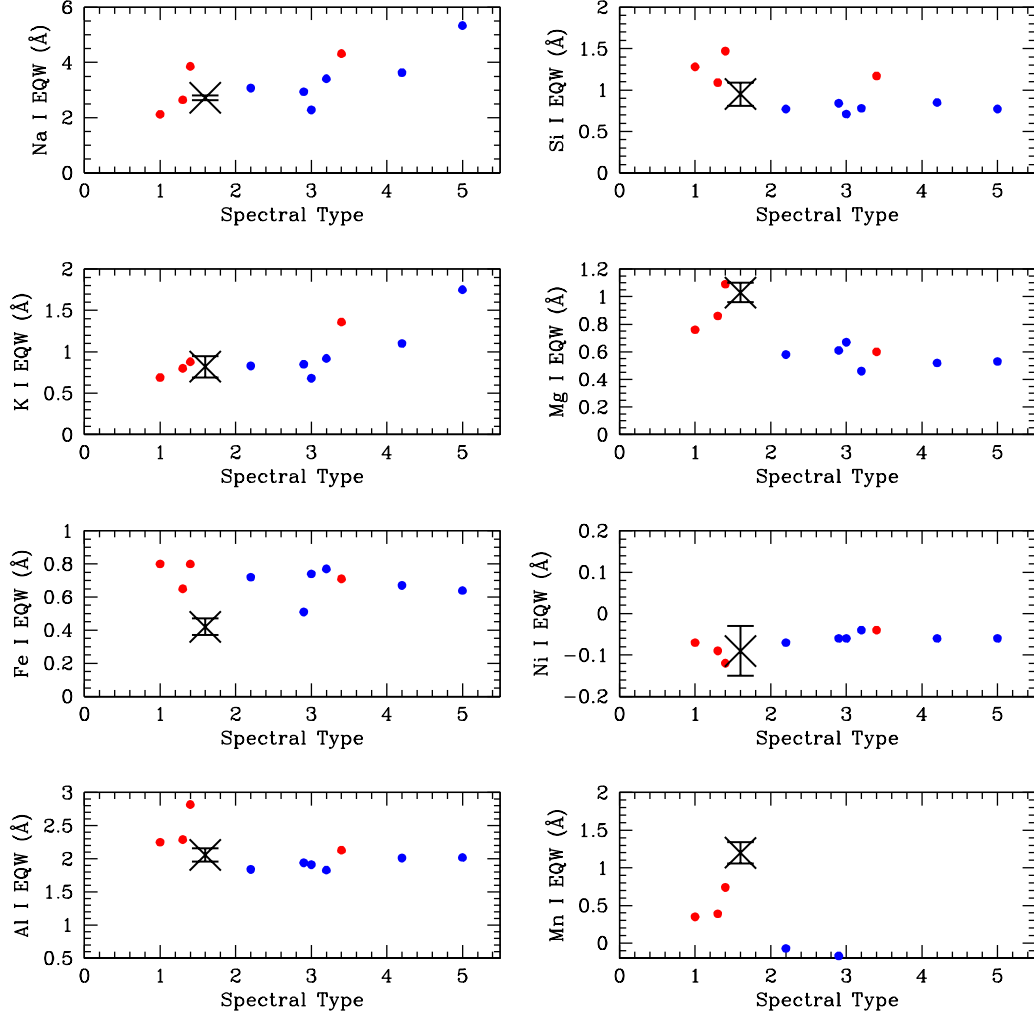


Fig. 17abc.— As in Fig. 12abc, we compare the EQW measurements of Z Cam in the  $J$ -band to those of M dwarfs.

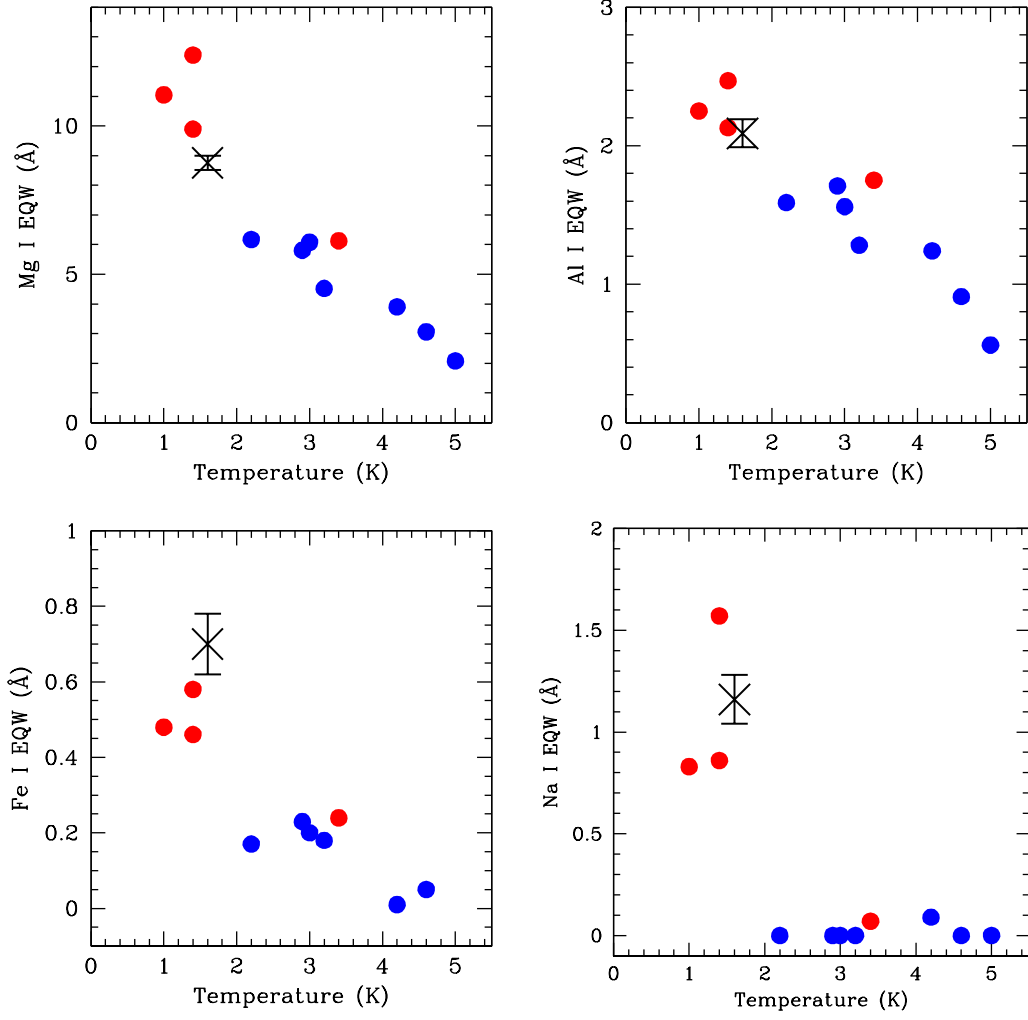


Fig. 17b.— As in Fig. 17abc, but for the *H*-band.

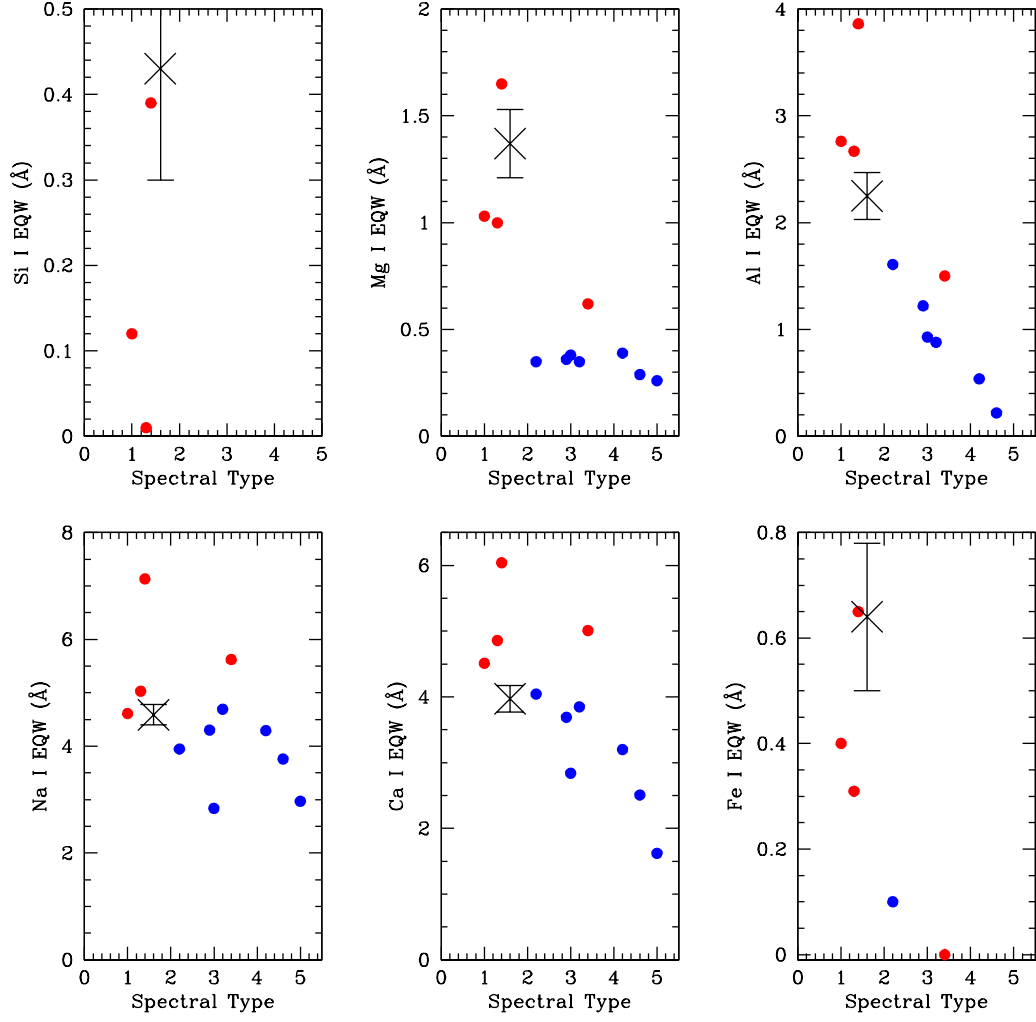


Fig. 17c.— As in Fig. 17abc, but for the *K*-band.

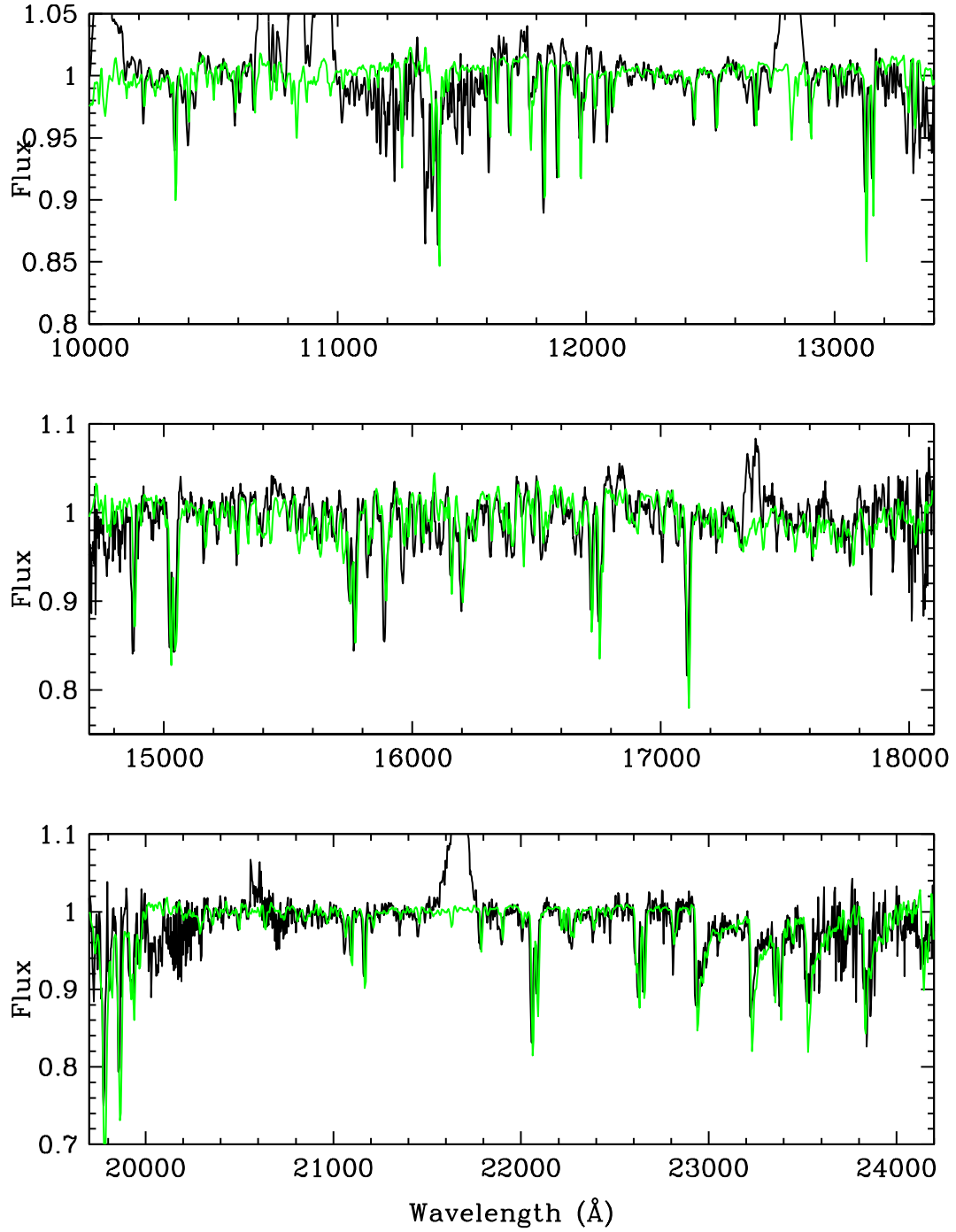


Fig. 18.— The *JHK* spectra of Z Cam (black) compared to to that of HD 42581, an M1.3V (green).

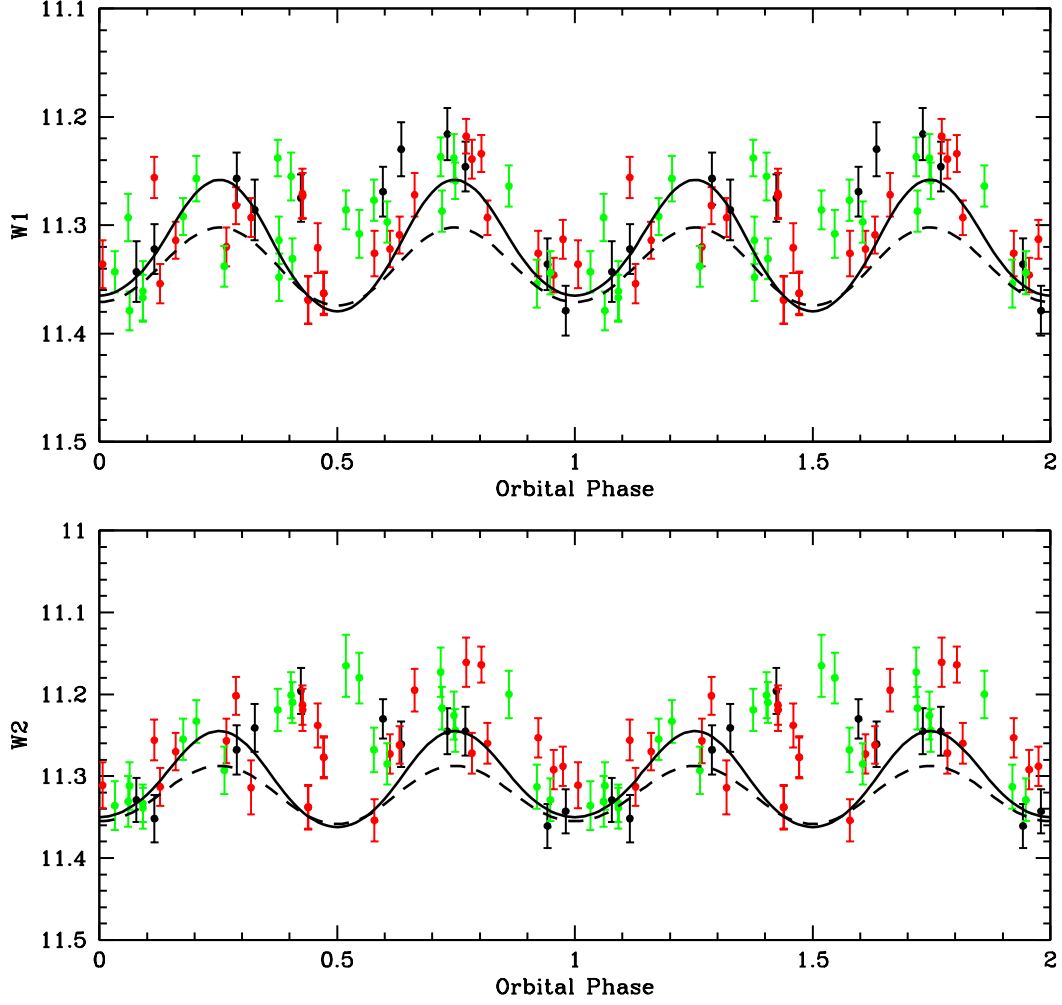


Fig. 19.— The *WISE* (black) and *NEOWISE*, 2016 April (red), and 2016 November (green) data for SY Cnc. The solid black line is a light curve model with  $i = 55^\circ$ , while the dashed curve is for  $i = 38^\circ$ .

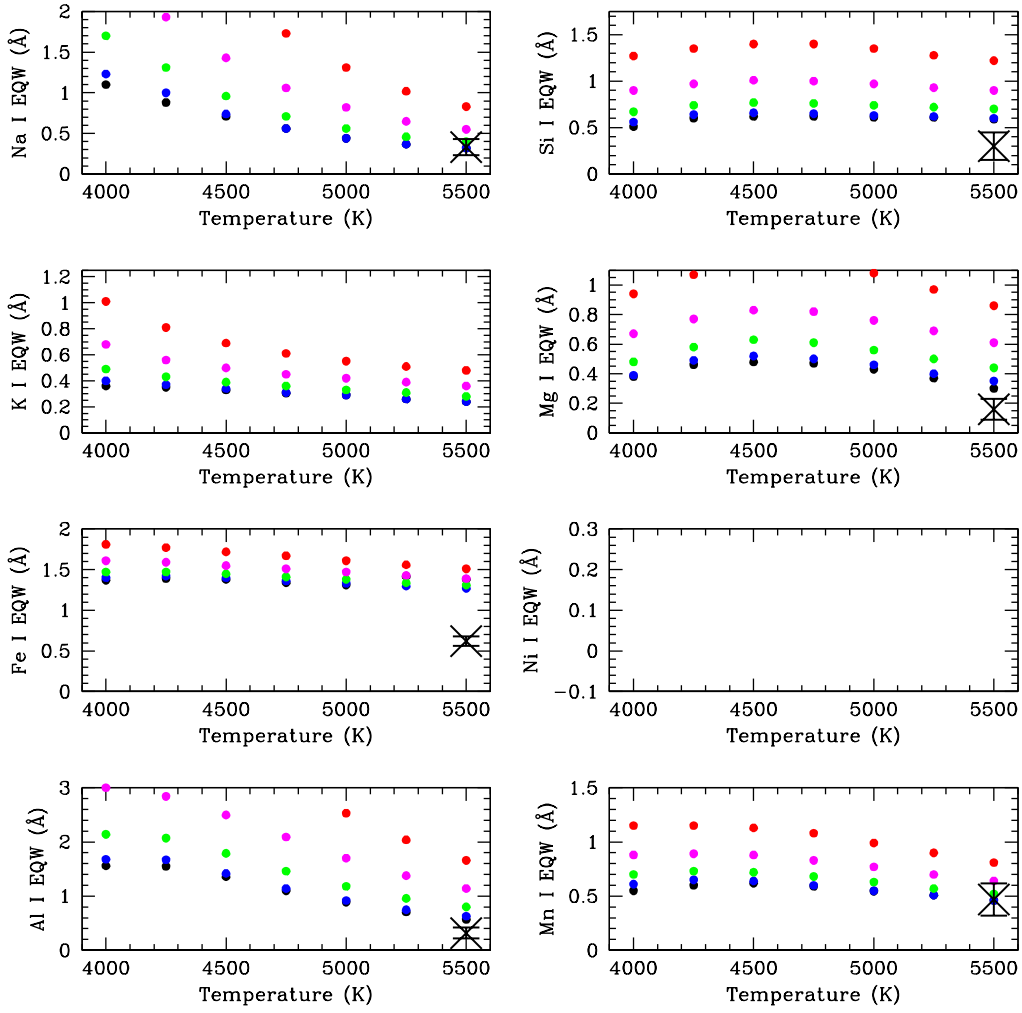


Fig. 20abc.— The EQW measurements for SY Cnc in the  $J$ -band. Before the analysis, both the source and synthetic spectra were boxcar smoothed by 5 pixels.

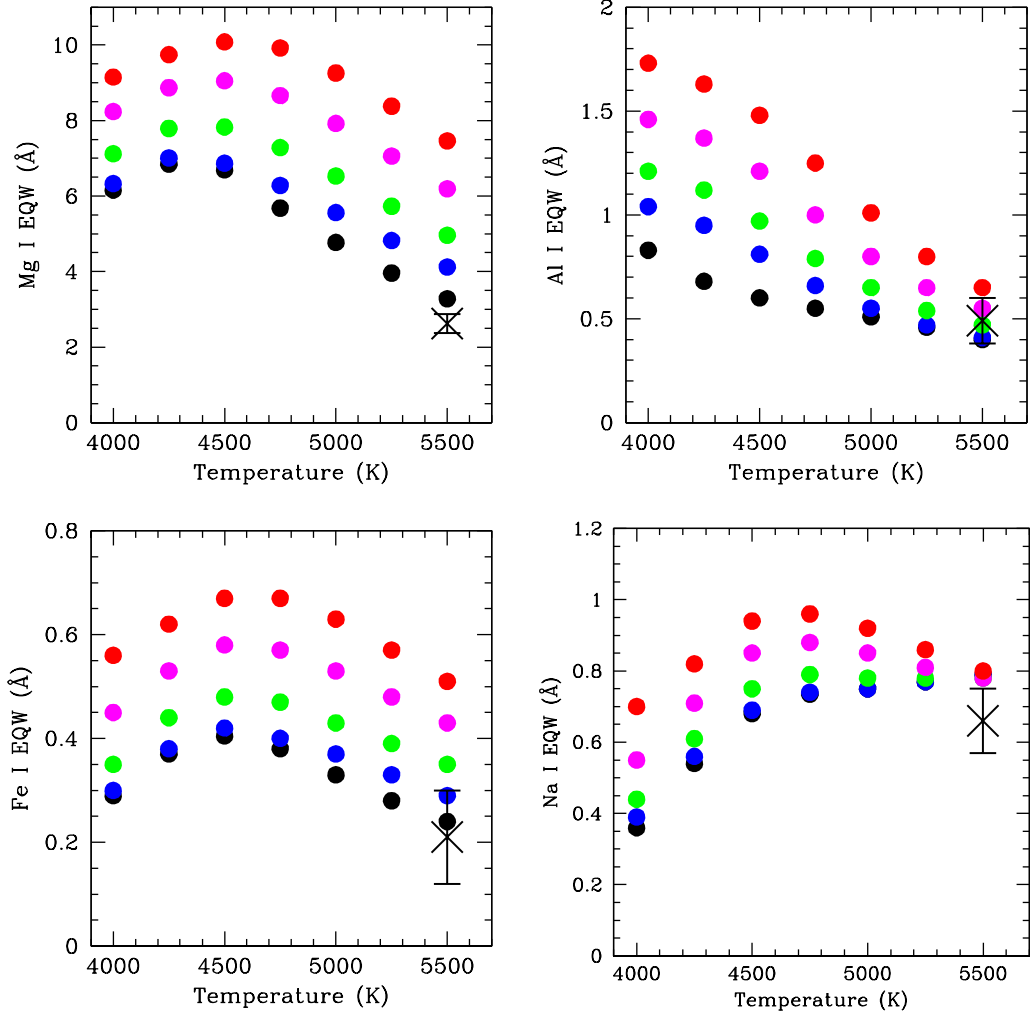


Fig. 20b.— The same as panel *a*, but for the *H*-band.

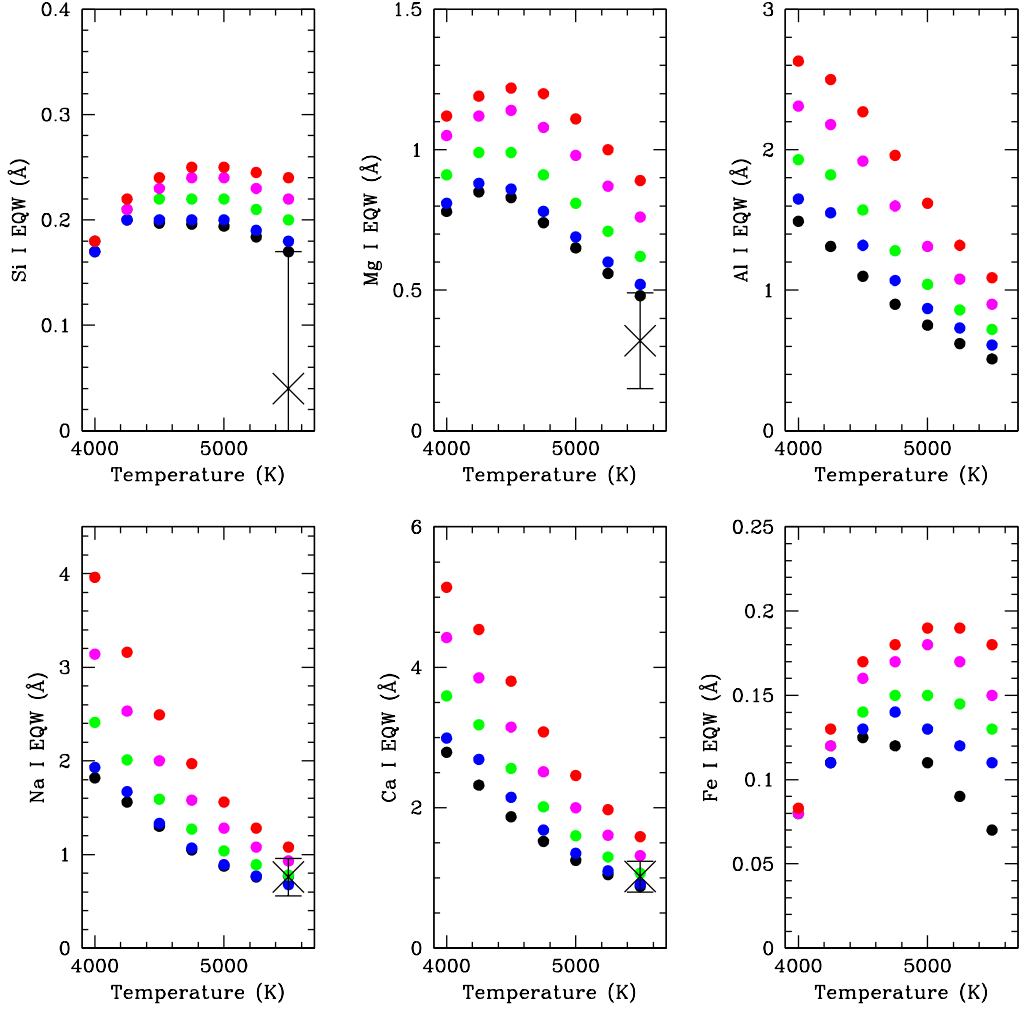


Fig. 20c.— The same as panel *a*, but for the *K*-band.

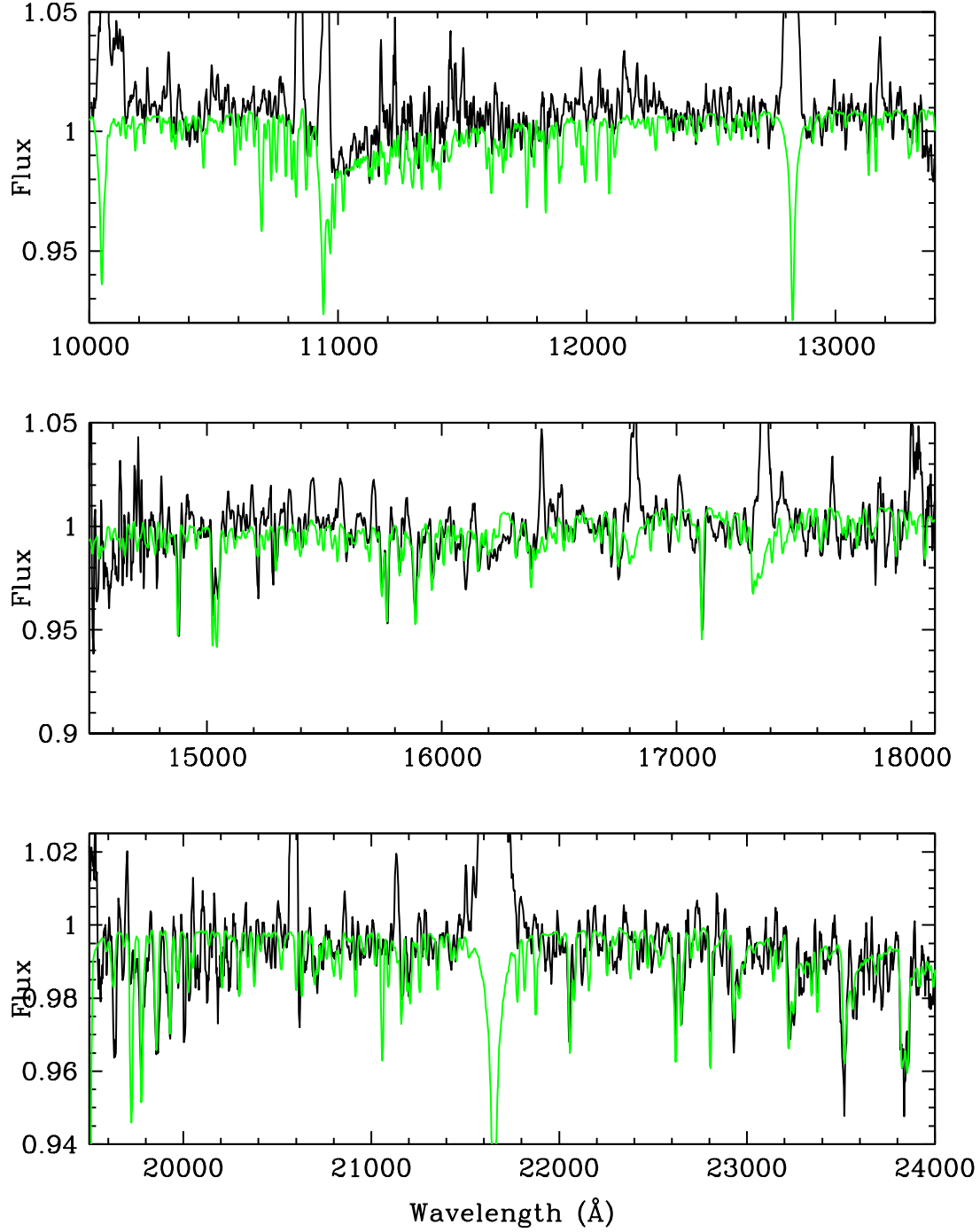


Fig. 21.— The *JHK* spectra of SY Cnc compared to a (highly contaminated) synthetic spectrum that has  $T_{\text{eff}} = 5250$  K,  $[\text{Fe}/\text{H}] = 0.0$ , and  $[\text{C}/\text{Fe}] = 0.0$ . Both model and source spectra have been boxcar smoothed by 5 pixels.

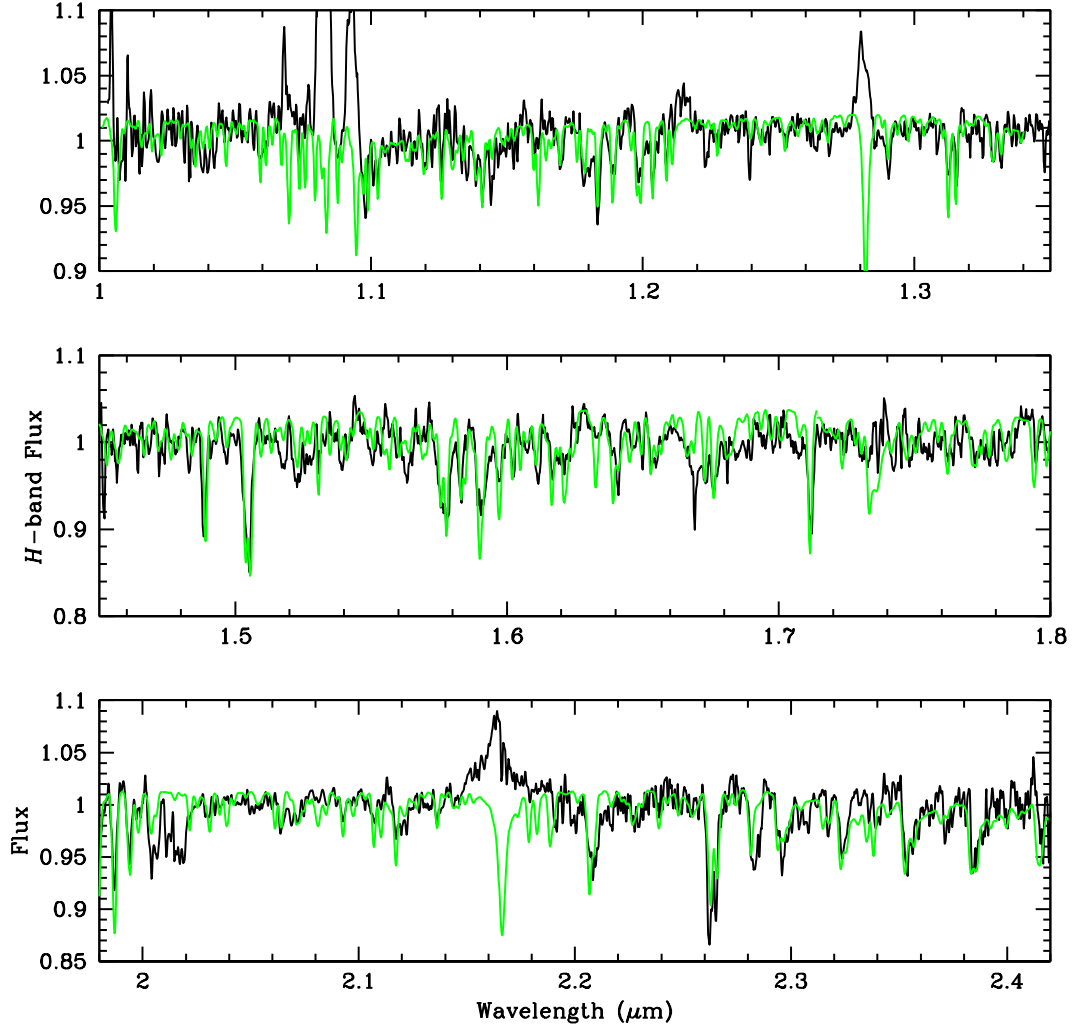


Fig. 22.— The Gemini GNIRS spectra of EM Cyg (black). A synthetic model spectrum is plotted in green, and has  $T_{\text{eff}} = 4500$  K,  $[\text{C}/\text{Fe}] = -0.5$ , and  $[\text{Mg}/\text{Fe}] = -0.5$ .

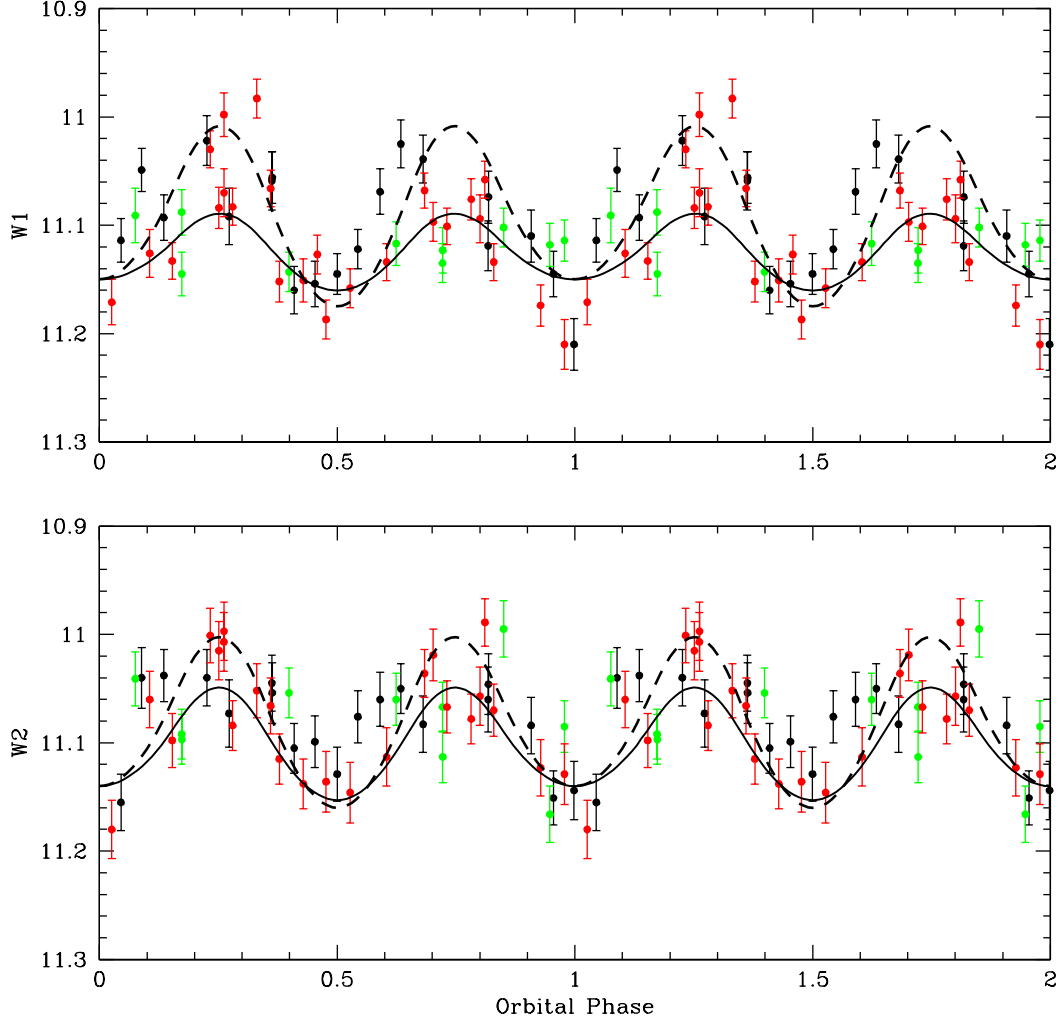


Fig. 23.— The *WISE* (black circles), and *NEOWISE* light curves for EM Cyg. There are two epochs of *NEOWISE* data plotted here. The one in green is for 2014 Oct 24, and the one in red is for 2015 Oct 18. The solid curve is the light curve model assuming a contaminating source. The dashed curve assumes no contamination.

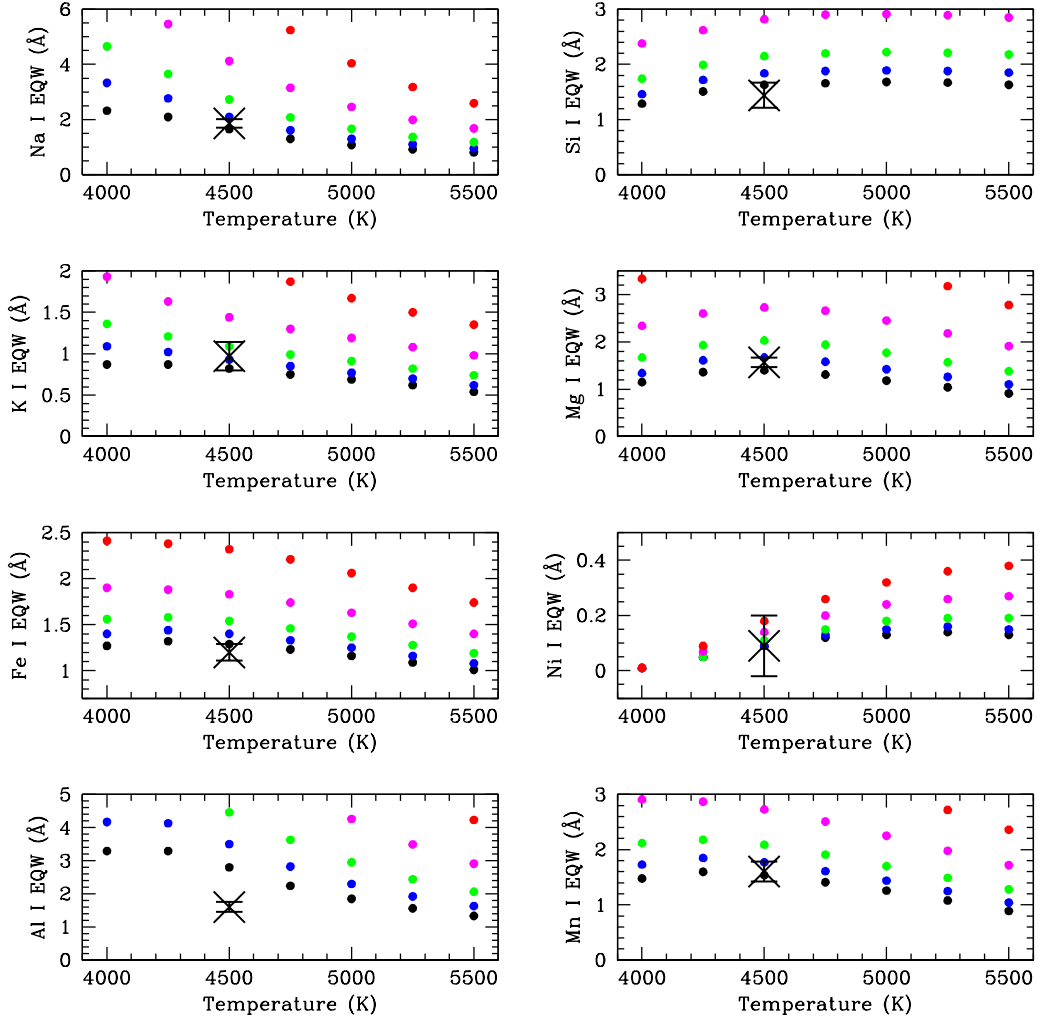


Fig. 24abc.— The EQW measurements for EM Cyg in the  $J$ -band compared to a solar abundance pattern grid.

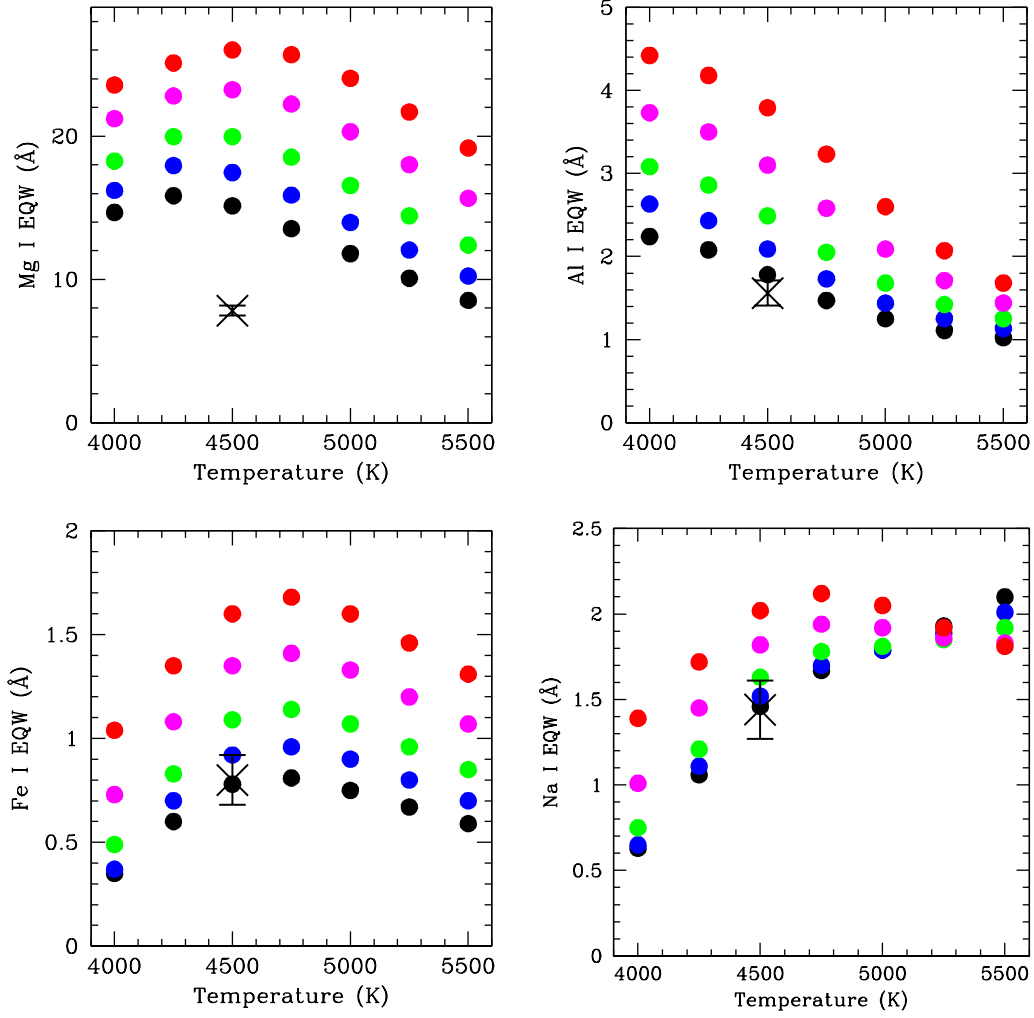


Fig. 24b.— The same as panel *a*, but for the *H*-band.

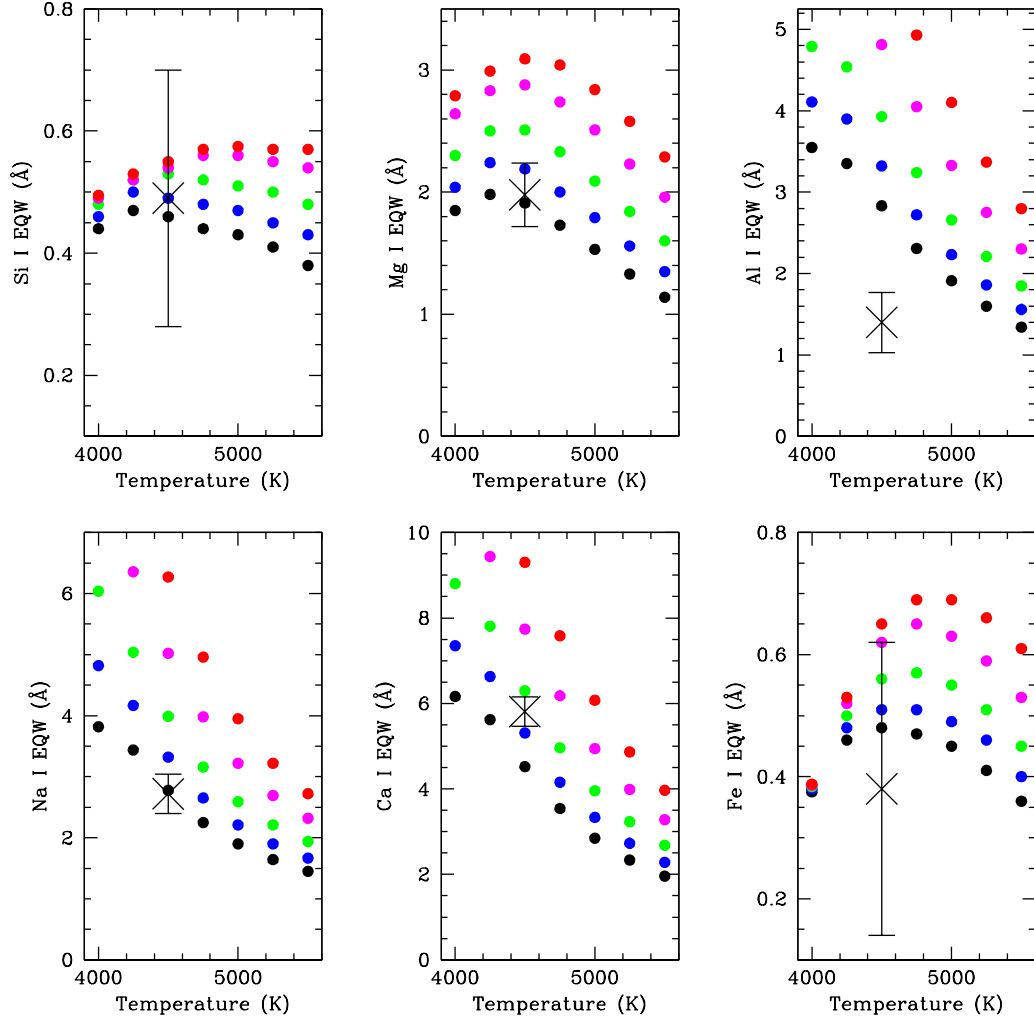


Fig. 24c.— The same as panel *a*, but for the *K*-band.

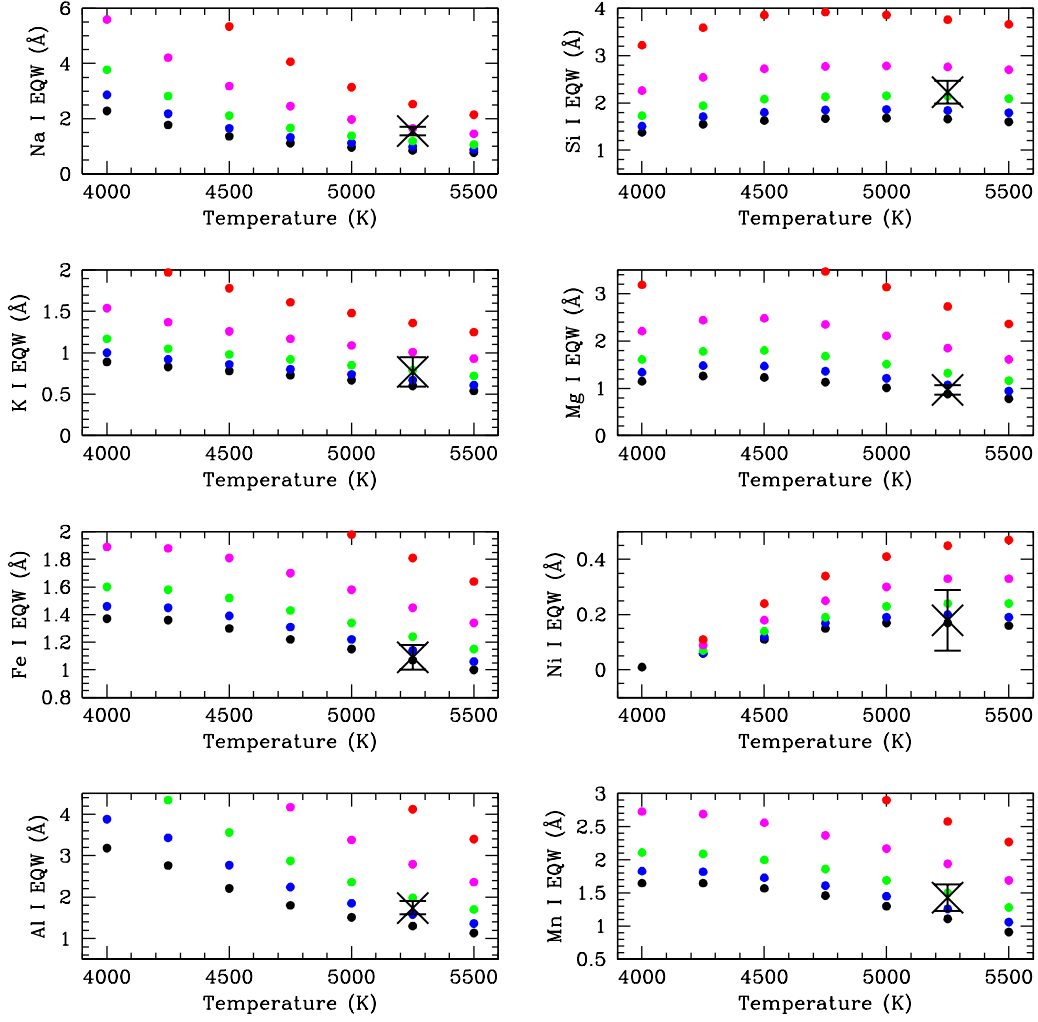


Fig. 25abc.— The fit of the  $J$ -band EQW measurements for EY Cyg to those for the synthetic spectra with  $\log g = 4.0$ , and  $[\text{Fe}/\text{H}] = 0.0$ .

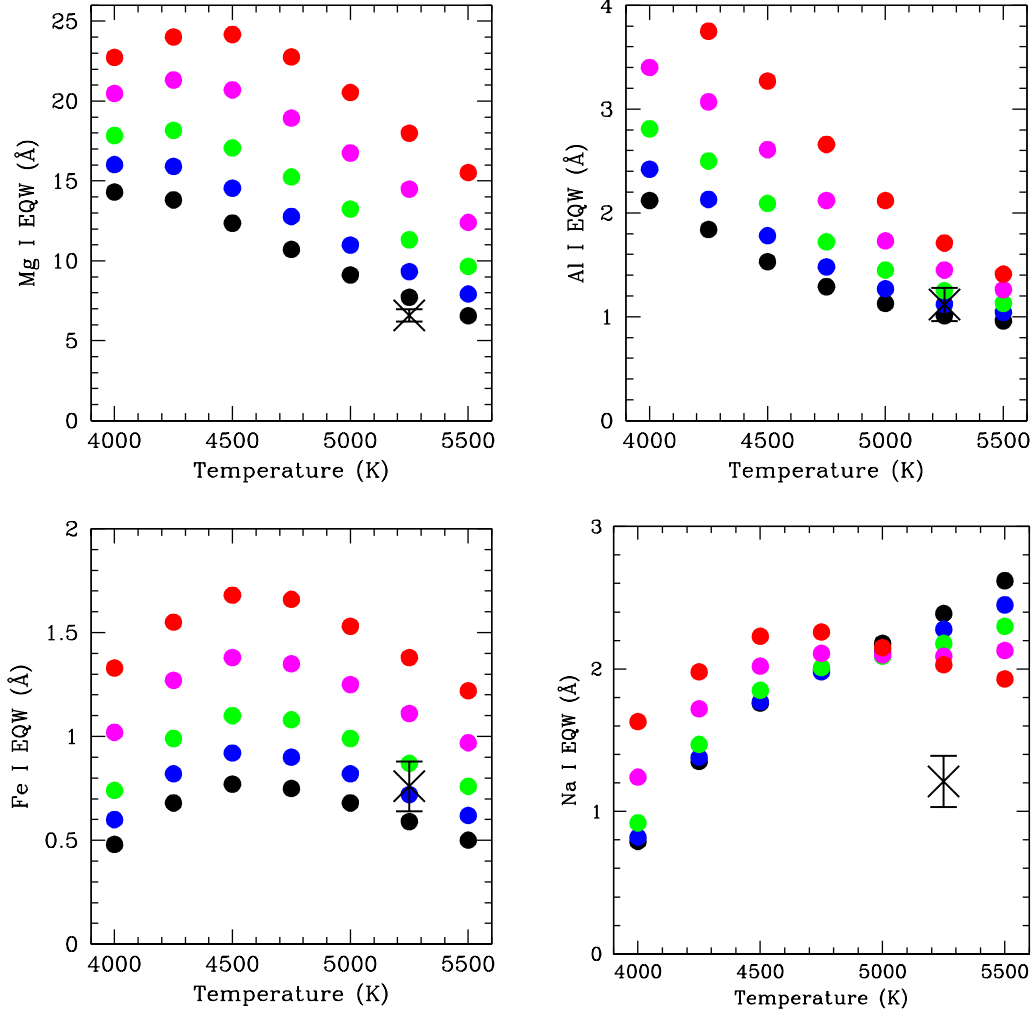


Fig. 25b.— The same as panel *a*, but for the *H*-band.

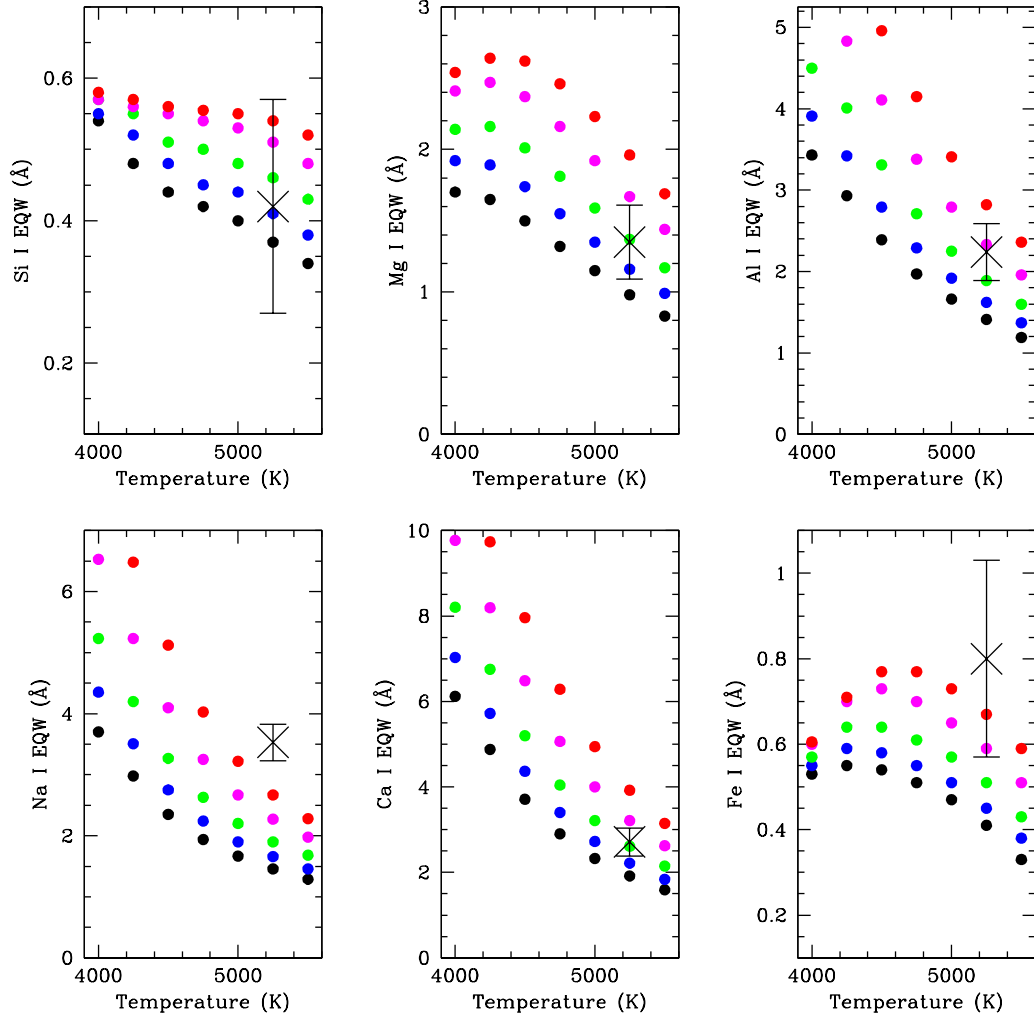


Fig. 25c.— The same as panel *a*, but for the *K*-band.

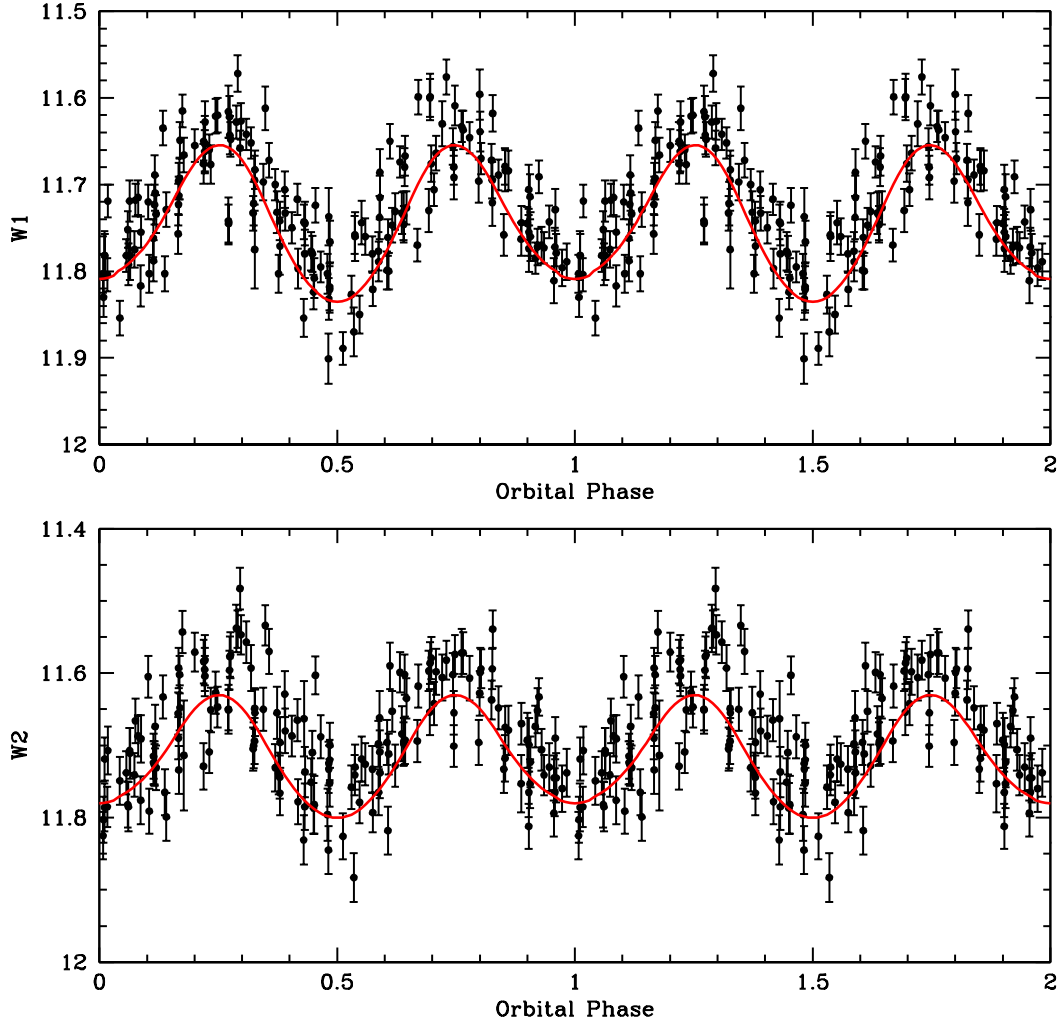


Fig. 26.— The *WISE/NEOWISE* light curves of V508 Dra. The light curve model, with an orbital inclination of  $i = 75^\circ$ , is plotted in red.

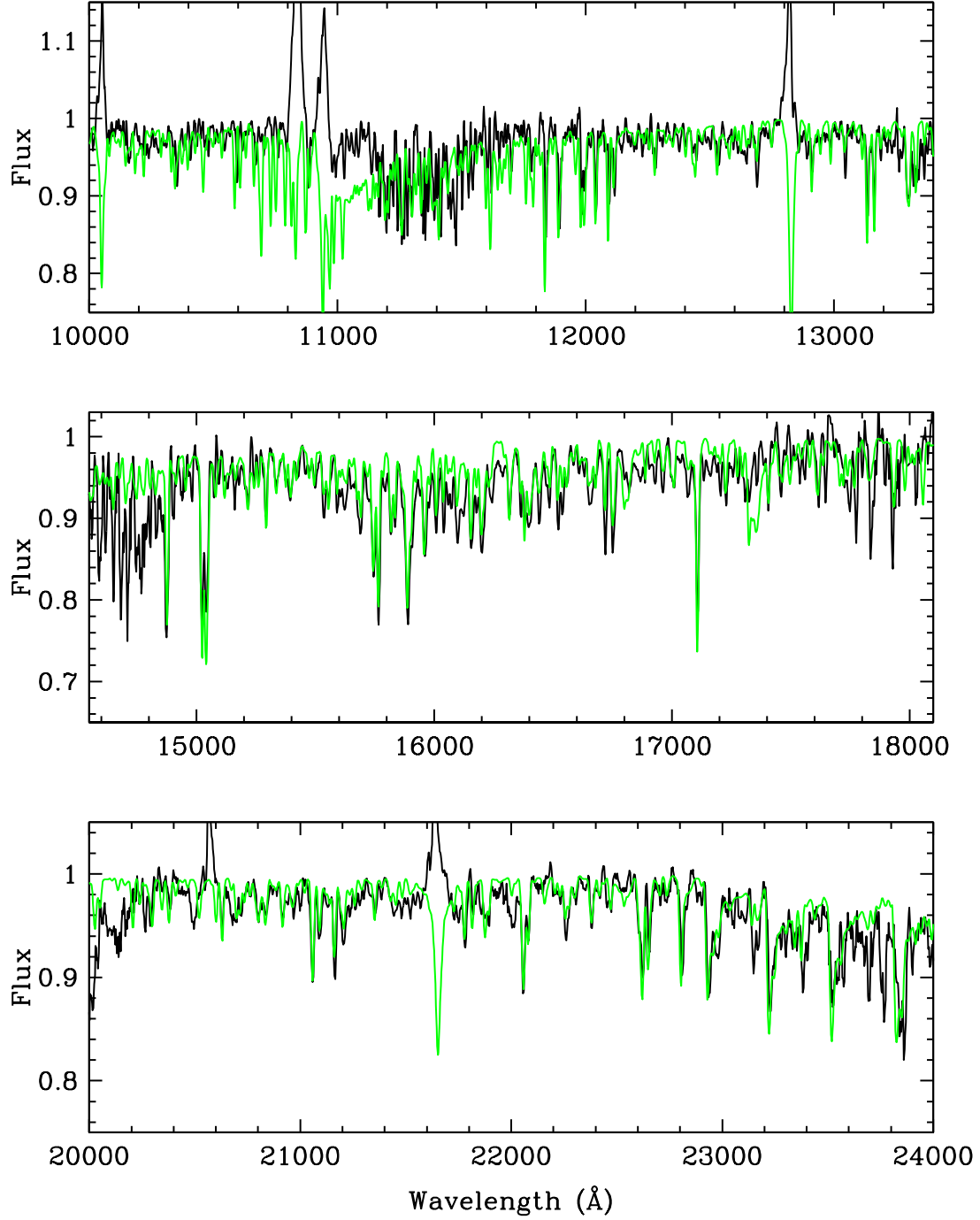


Fig. 27.— The *JHK* spectra of V508 Dra (black), overplotted by a synthetic spectrum with  $T_{\text{eff}} = 4500$  K,  $\log g = 4.0$ ,  $[\text{Fe}/\text{H}] = 0.0$ , and  $[\text{C}/\text{Fe}] = -0.3$  (green).

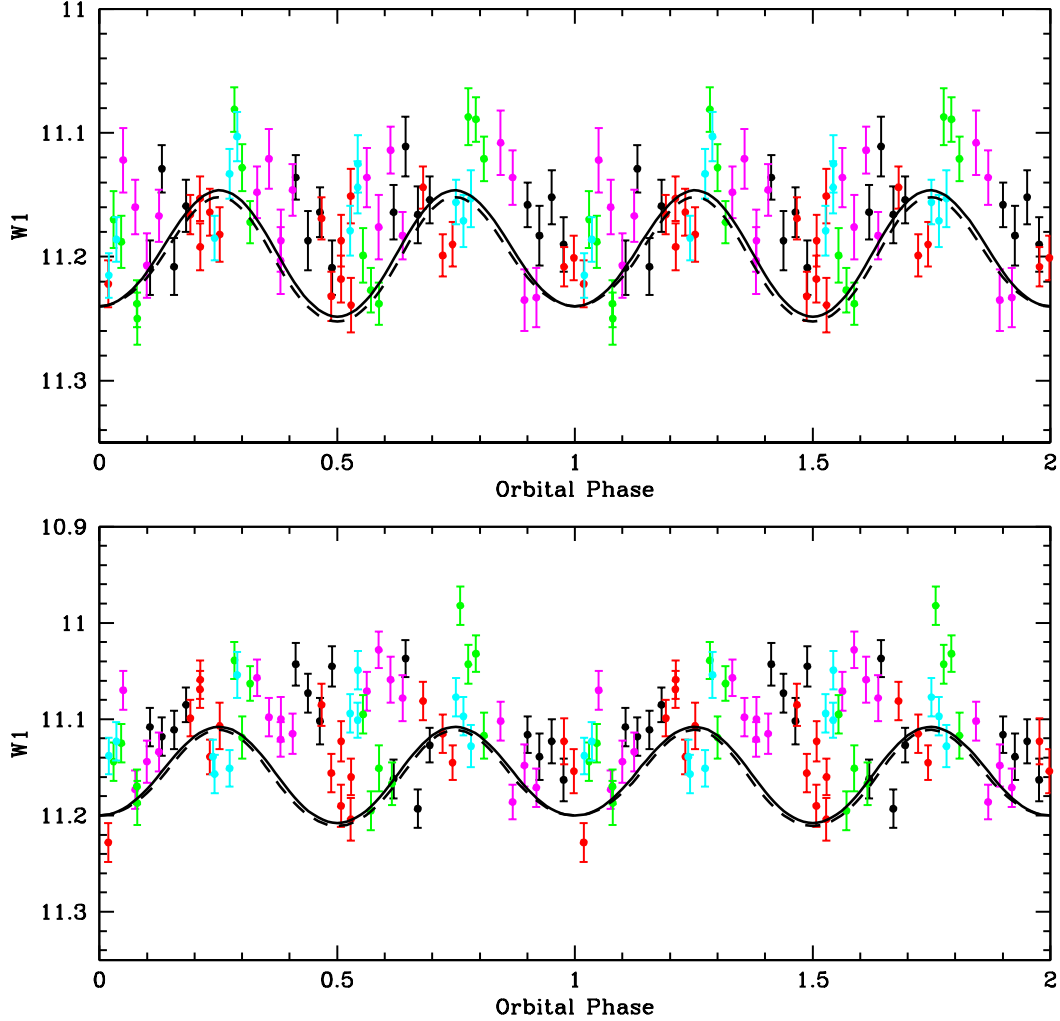


Fig. 28.— The *WISE*/*NEOWISE* light curves of AH Her. The black points are the *WISE* data for the epoch of 2010 February 22. We have calculated the mean values in both *W1* and *W2* for all five epochs of data, and have offset them to match the values for the initial *WISE* epoch. The magenta points are for the second *WISE* epoch (2010 August 23), red represents the first *NEOWISE* epoch (2014 February 22), green is for 2015 August 17, cyan is for 2016 February 22. The solid line is a light curve model for  $i = 46^\circ$ . The dashed line is a light curve model with  $i = 58^\circ$ , with a contaminating source that supplies 30% of the flux.

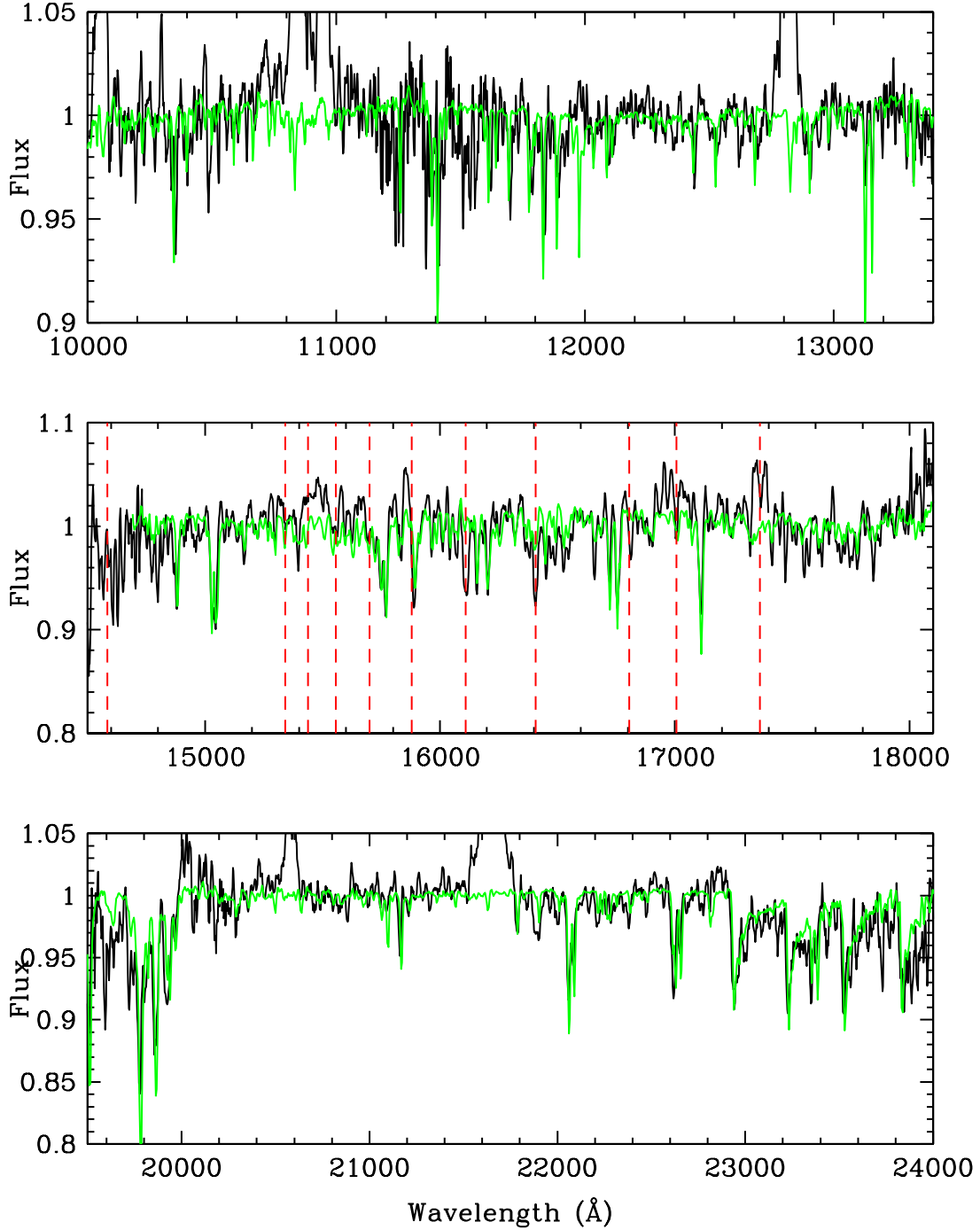


Fig. 29.— The TripleSpec data for AH Her (black). We overplot the spectra of the M1.3 dwarf HD 42581 from the IRTF Spectral Library (green). In the panel for the  $H$ -band, we locate the H I Brackett series as vertical red dashed lines. The line at  $\lambda 17005$  Å is due to He I. The left most line represents the Brackett limit.

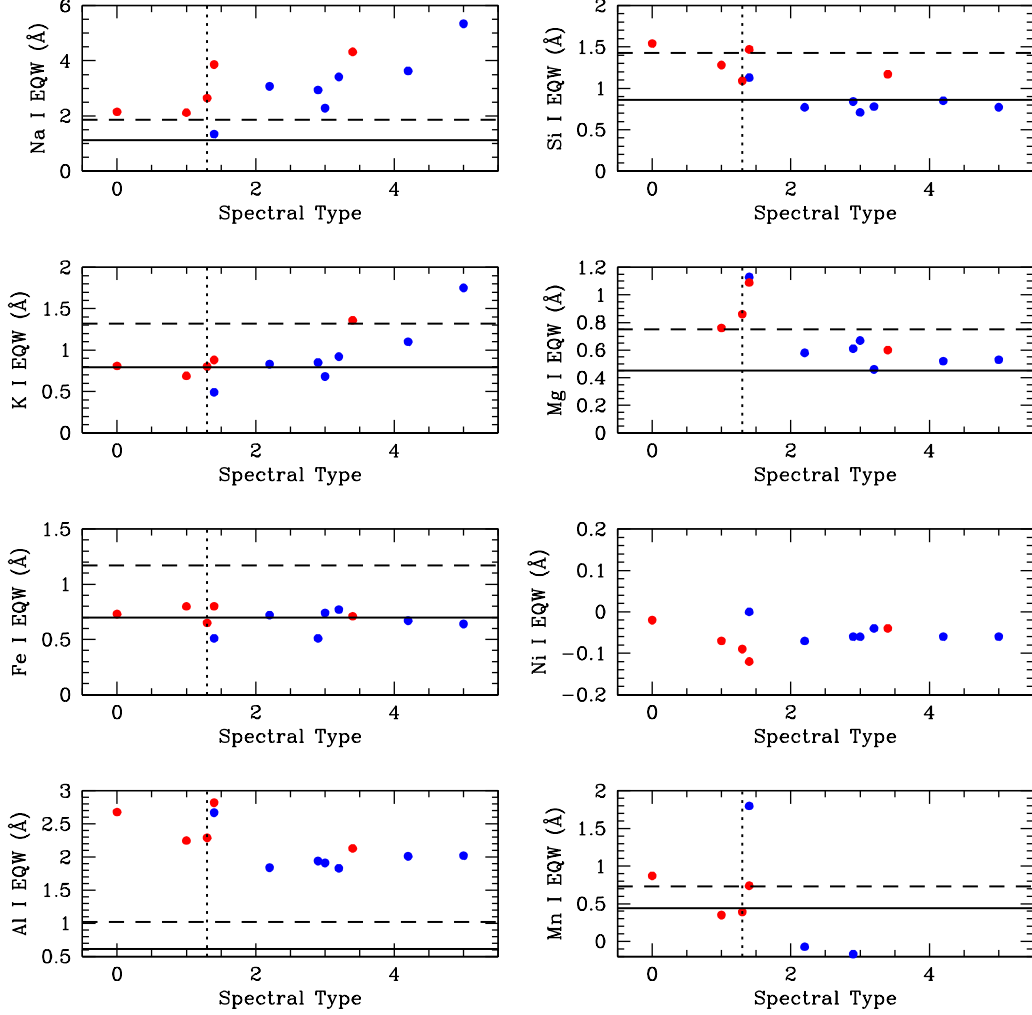


Fig. 30abc.— The EQW measures for AH Her in the  $J$ -band, plotted as a solid horizontal line, compared to those of M dwarfs (see Fig. 12abc). The horizontal dashed line would be the true EQW measures for AH Her if they were not diluted by a 40% level of contamination. The vertical dotted line is the derived spectral type.

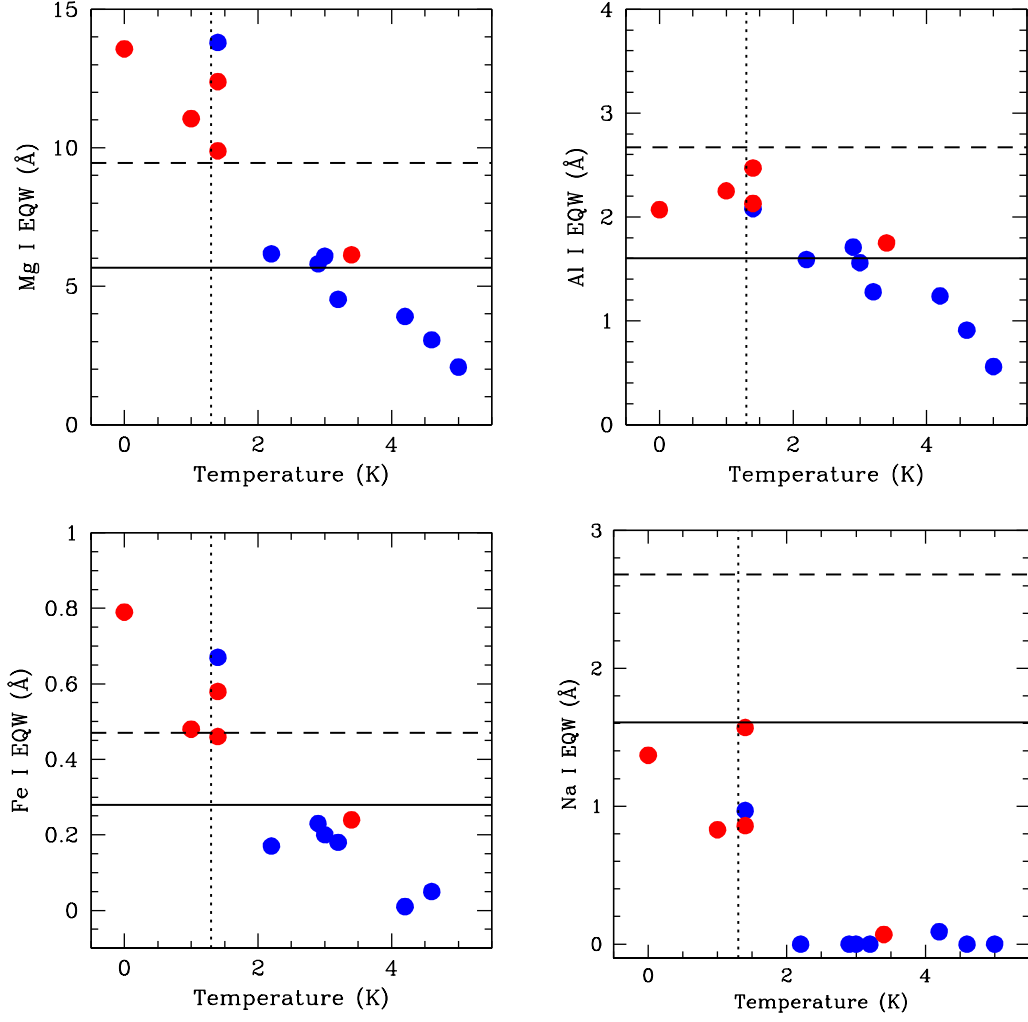


Fig. 30b.— The same as panel *a*, but for the *H*-band.

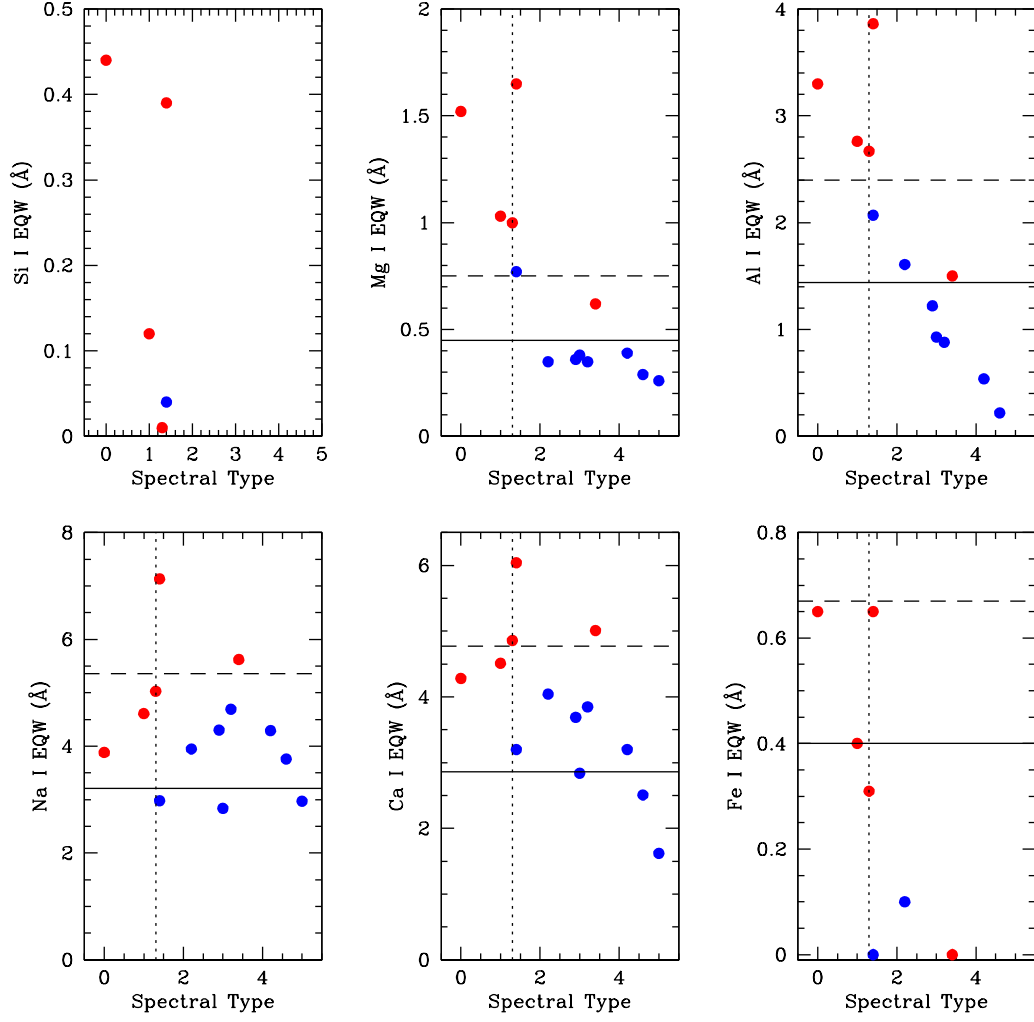


Fig. 30c.— The same as panel *a*, but for the *K*-band.

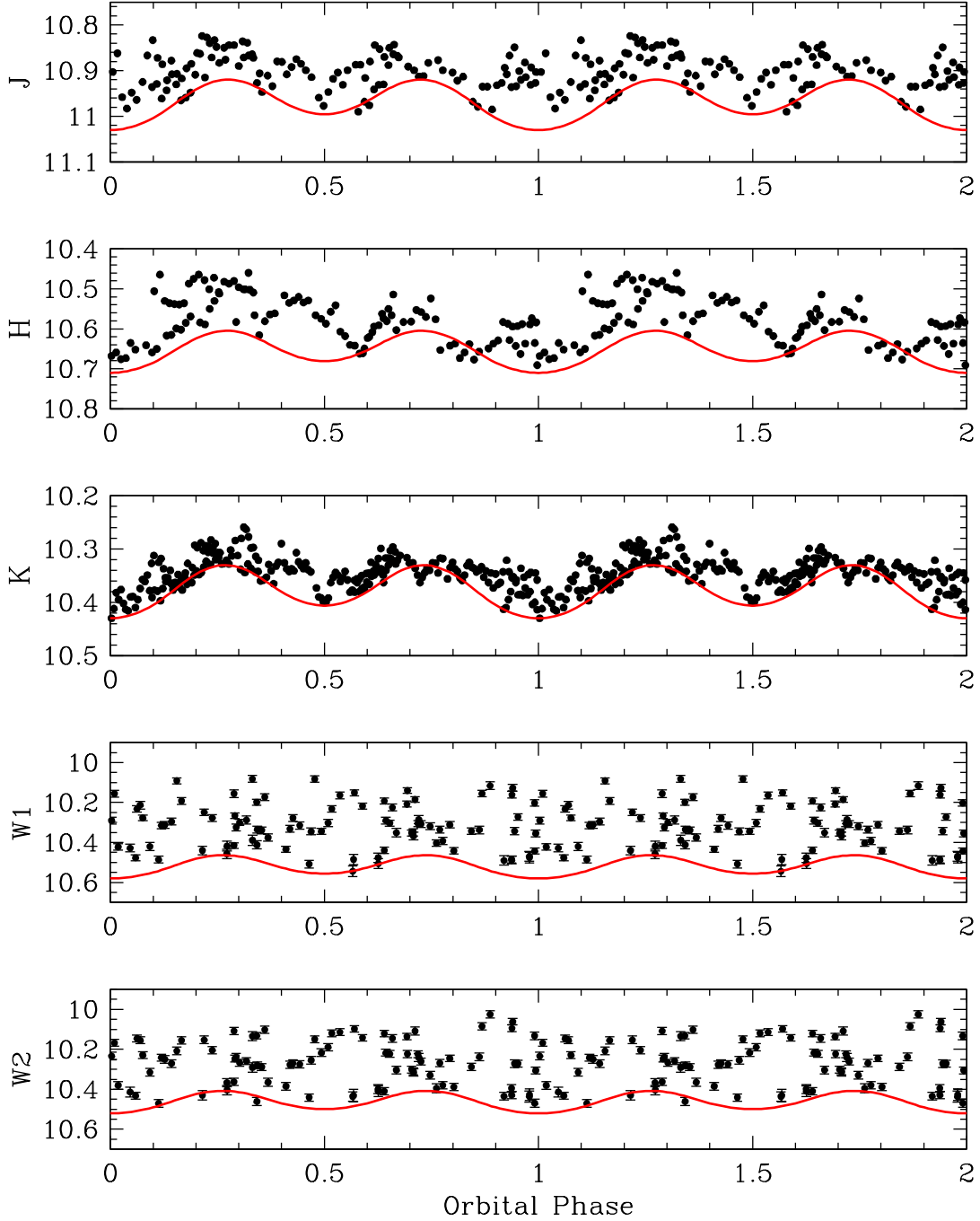


Fig. 31.— The *JHK*, *WISE* and *NEOWISE* light curves for RU Peg. The *JHK* data were obtained with SQUIID over three nights, 2003 August 3 through 5. The light curve model (red) has  $T_1 = 45,000$  K,  $T_2 = 5,000$  K,  $i = 50$ , and a contamination level of 25%.

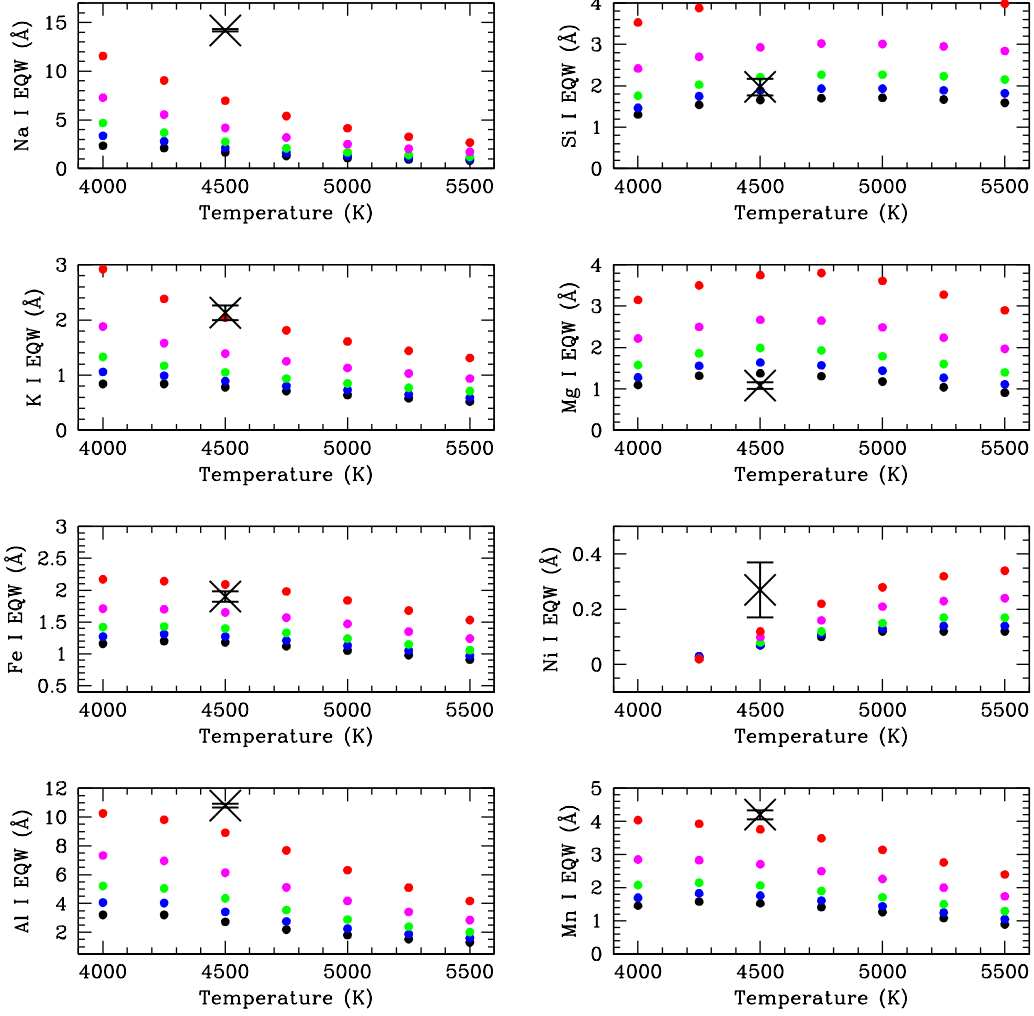


Fig. 32abc.— The equivalent width measurements for QZ Ser in the *J*-band.

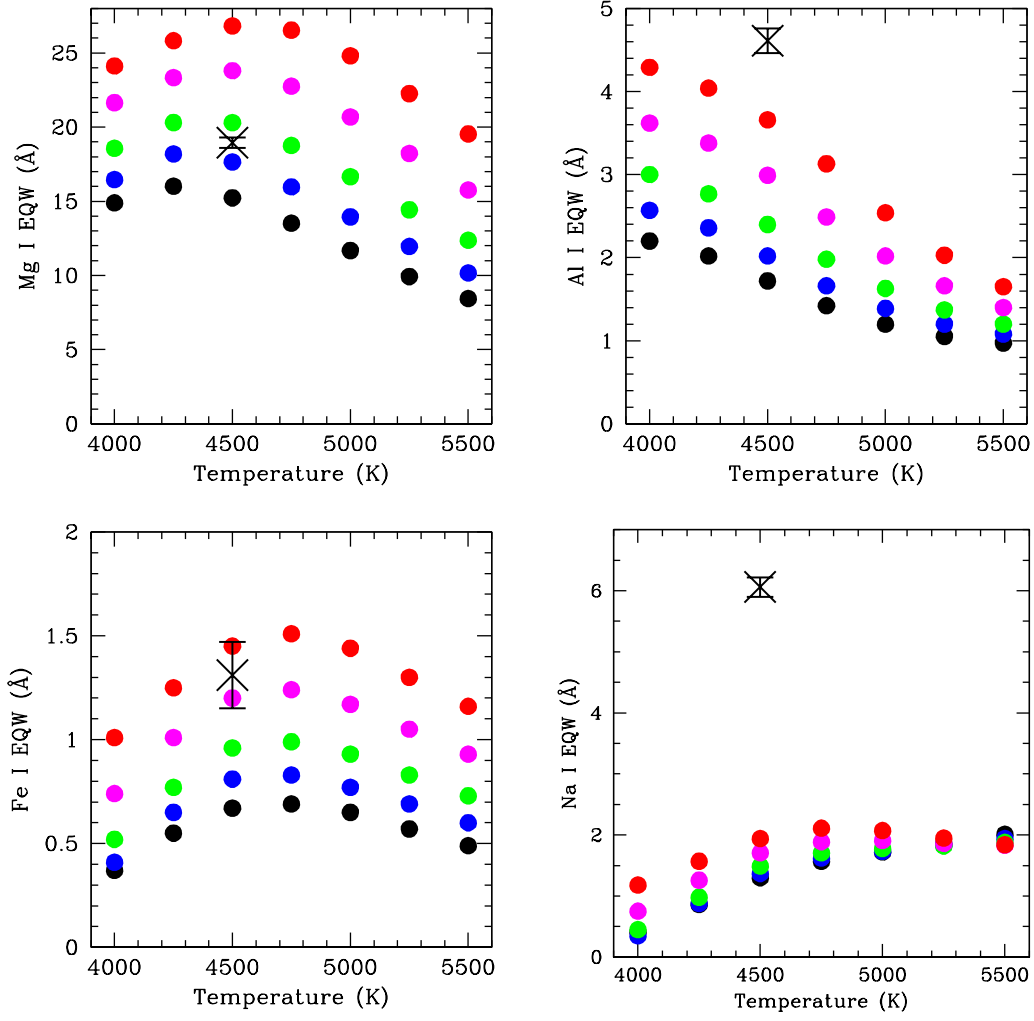


Fig. 32b.— The same as panel A, for the *H*-band.

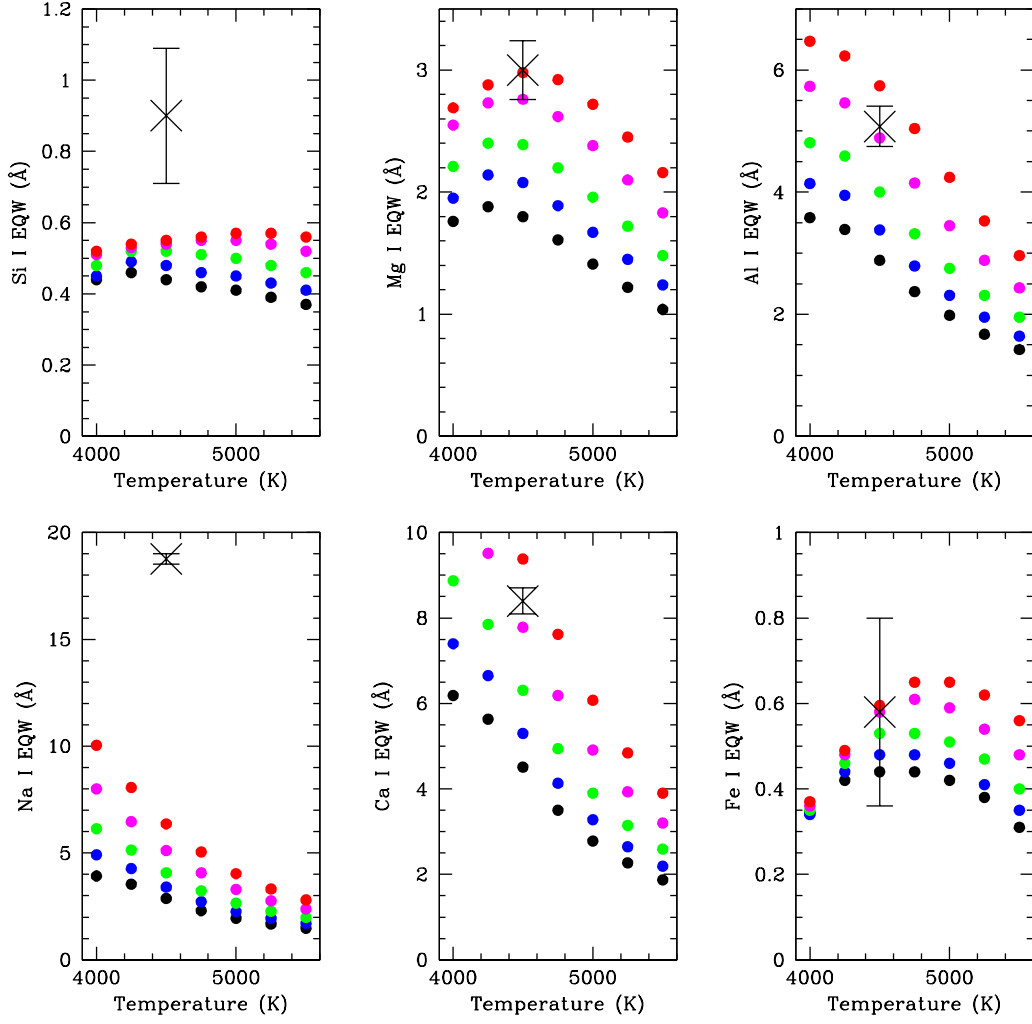


Fig. 32c.— The same as panel *A*, for the *K*-band.

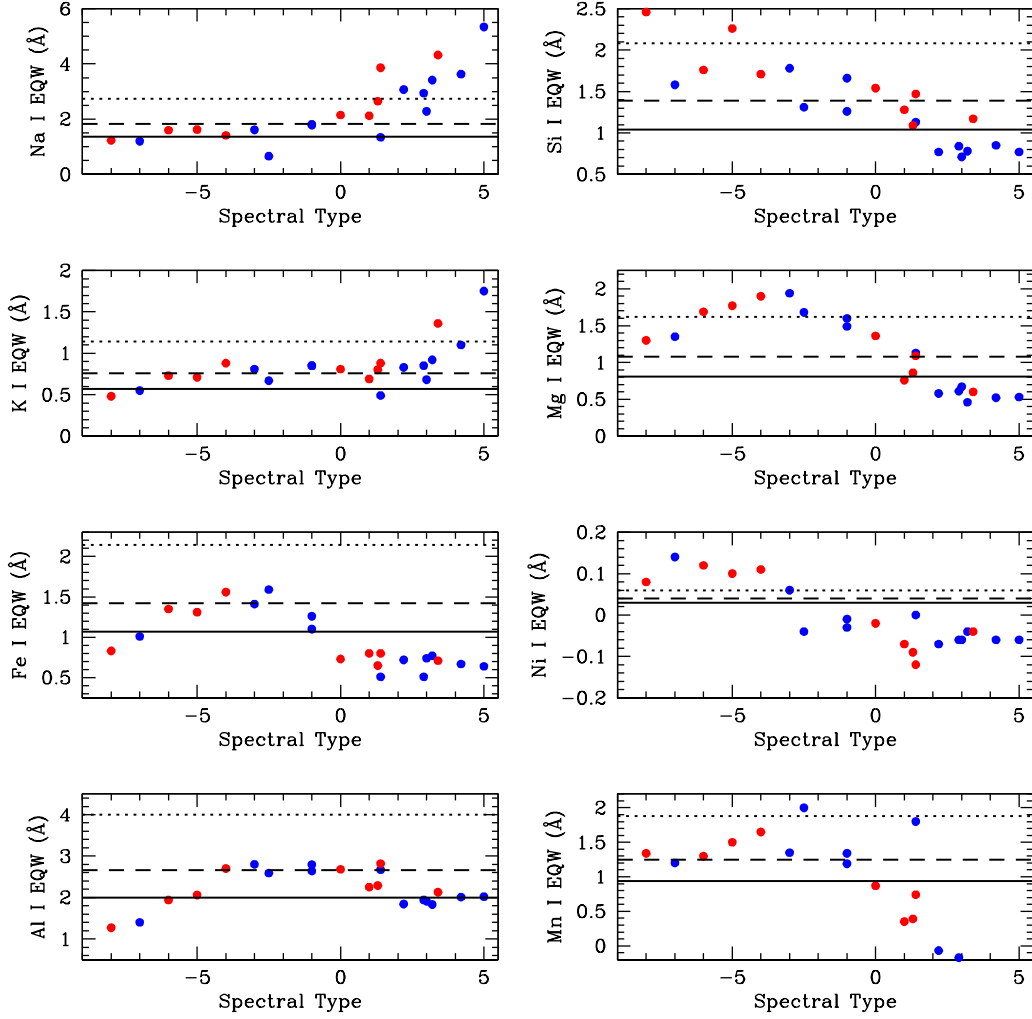


Fig. 33abc.— The equivalent width measurements in the  $J$ -band for SS Cyg, solid lines, compared to those of K and M dwarfs. The latter have been color coded so that red is  $[\text{Fe}/\text{H}] > 0.0$ , and blue is  $[\text{Fe}/\text{H}] < 0.0$ . The dashed lines are what the EQWs of SS Cyg would be if a contamination level of 25% was removed. The dotted line is for a contamination level of 50%. SS Cyg has a spectral type of  $-4.5$ .

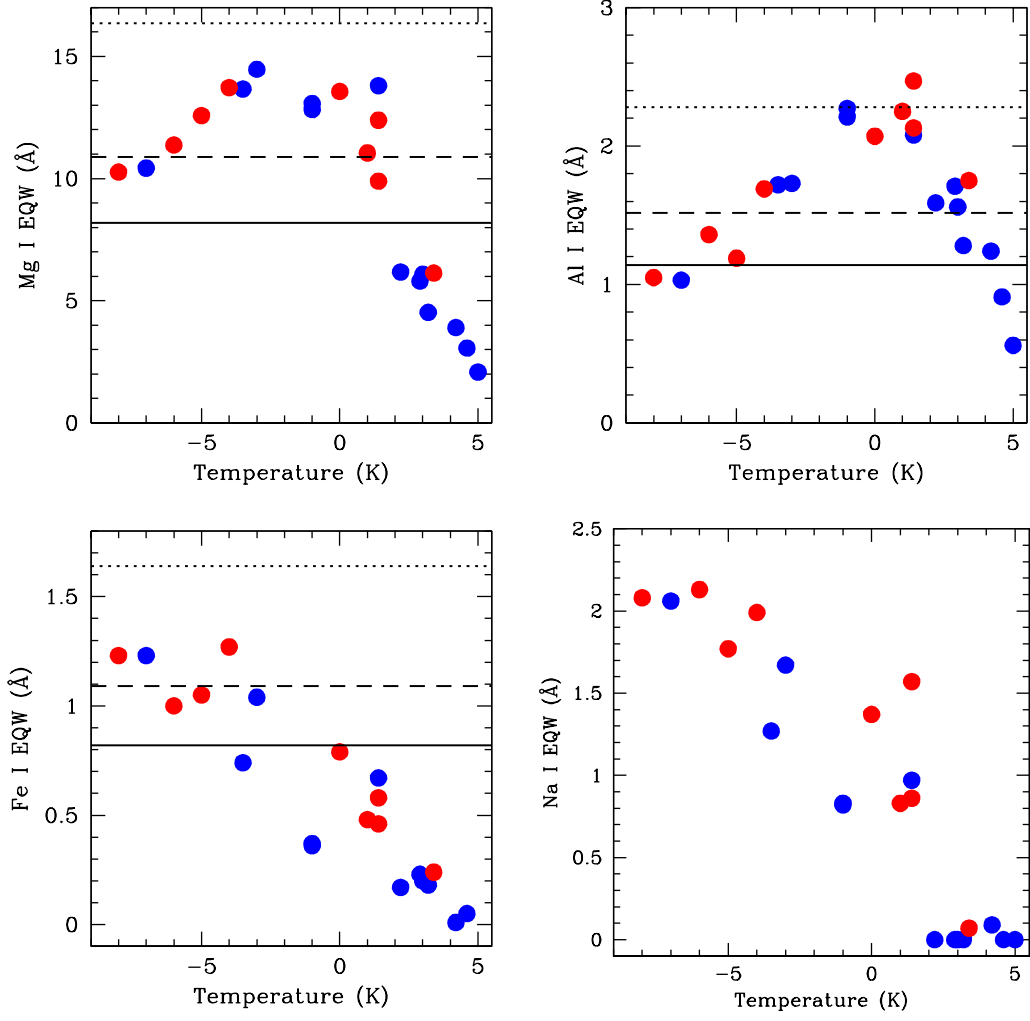


Fig. 33b.— The same as panel *a*, but for the *H*-band. Due to an emission feature, the Na I doublet in the *H*-band was unmeasurable.

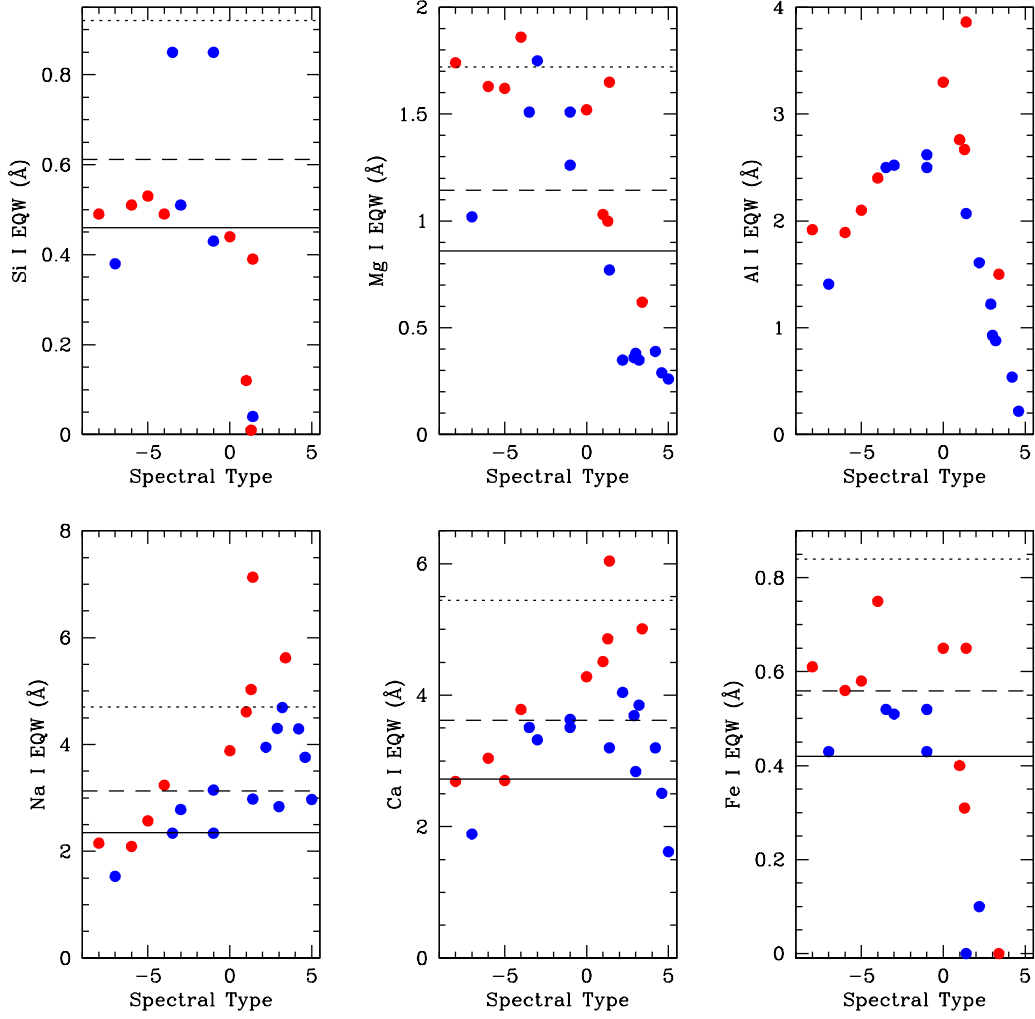


Fig. 33c.— The same as panel *a*, but for the *K*-band. An He I emission line corrupts the measurement of the Al I feature at 21100 Å.